Additive Manufacturing of Copper via Binder Jetting of Copper Nanoparticle Inks

Yun Bai

Dissertation submitted to the faculty of the Virginia Polytechnic Institute and State University in partial fulfillment of the requirements for the degree of

Doctor of Philosophy
In
Mechanical Engineering

Christopher B. Williams (Chair)
Alex O. Aning
Thomas E. Diller
Peizhen (Kathy) Lu
Carlos T. A. Suchicital
Xiaoyu (Rayne) Zheng

April 9, 2018
Blacksburg, VA

Keywords: Additive Manufacturing, 3D Printing, Binder Jetting, Copper, Nanoparticle

Additive Manufacturing of Copper via Binder Jetting of Copper Nanoparticle Inks

Yun Bai

ACADEMIC ABSTRACT

This work created a manufacturing process and material system for the Additive Manufacturing of copper based on binder jetting. In order to reduce the sintered part porosity and shape distortion through an improved powder bed density, a bimodal particle size powder bed and multiple nanoparticle binders were investigated. The goals of this work are to develop an understanding of (i) the relationship between printed part properties and powder bed particle size distribution, and (ii) the binder-powder interaction and printed primitive formation in binder jetting of metals.

Bimodal powder mixtures created by mixing a coarse powder with a finer powder were investigated first. Compared to the parts printed with the monosized fine powder constituent, the use of a bimodal powder mixture improved the powder flowability and packing density, and therefore increased the green part density (8.2%), reduced the sintering shrinkage (6.4%), and increased the sintered density (4.0%).

The deposition of nanoparticles to the powder bed voids was achieved by three different metal binders: (i) a nanoparticles suspension in an existing organic binder, (ii) an inorganic nanosuspension, and (iii) a Metal-Organic-Decomposition ink. The use of nanoparticle binders improved the green part density and reduced the sintering shrinkage, which has led to an improved sintered density when high binder saturation ratios were used. A new binding mechanism based on sintering the jetted metal nanoparticles was demonstrated to be capable of (i) providing a permanent bonding for powders to improve the printed part structural integrity, and (ii) eliminating the need for organic adhesives to improve the printed part purity.

Finally, the binder-powder interaction was studied by an experimental approach based on sessile drop goniometry on a powder bed. The dynamic contact angle of binder wetting capillary pores was calculated based on the binder penetration time, and used to describe the powder permeability and understand the binder penetration depth. This gained understanding was then used to study how the nanoparticle solid loading in a binder affect the binder-powder interactions and the printed primitive size, which provided an understanding for determining material compatibility and printing parameters in binder jetting.

Additive Manufacturing of Copper via Binder Jetting of Copper Nanoparticle Inks

Yun Bai

GENERAL ABSTRACT

The binder jetting Additive Manufacturing (AM) process can be used to fabricate net-shape metal parts with complex geometries by selectively inkjet printing a liquid binding agent into a powder bed, followed by post-process sintering of the printed green parts. Motivated by the need to create highly efficient thermal management systems, this work has established a binder jetting manufacturing process chain for fabricating components made of pure copper, a conductive and optically reflective material that is challenging to be processed by laser-based AM systems. In order to improve the performance metrics (e.g., mechanical strength, electrical and thermal conductivity) of the printed copper parts, an overall strategy to improve powder bed packing density by filling the powder bed voids with fine particles was investigated. Through the use of a bimodal powder mixture and a nanoparticle binder, the sintered density and structural integrity of the printed parts were improved. Via the investigation of these novel material systems created for binder jetting of copper, (i) the gaps in understanding the relationship between printed part properties and powder bed particle size distribution were filled, and (ii) an experimental approach to characterize and understand the binder-powder interaction and printed primitive formation was created to guide the selection of printing parameters in binder jetting.

Acknowledgements

I would like to thank my advisor, Dr. Chris Williams, for having an opportunity to conduct this work under his guidance and support. I consider myself extremely fortunate to have known him and worked for him. I have learned from him how to do research, and more importantly, how to become a better human being. I am grateful for his mentoring, caring, and many of those great conversations that have provided tremendous enlightenments and encouragements in my brightest and darkest hours.

I would like to thank Drs. Alex Aning, Thomas Diller, Kathy Lu, Carlos Suchicital, and Rayne Zheng, for the discussion of my research, and their insights and suggestions provided to this dissertation.

I acknowledge the assistance and support on numerous instrumentation uses, which is essential in performing this work and provided to me by Thomas Staley, Stephen McCartney, Carlos Suchicital, Alex Aning, Hesham Elmkharram, Jeremy Beach, Alan Druchitz, Mac McCord, Robert Mills, James Kong, Peter Jia Liu, Candace Wall, Alan Esker, and Emily Wilts.

I am grateful for the great working relationships with the students and alumni of the DREAMS lab, with special thanks given to Drew Snelling, Nick Meisel, and Amy Elliot for being great mentors. I also acknowledge the assistance and contributions provided to several projects related to this work, from Grady Wagner, Ashwath Kumar, Hannah Pham, and Susan Ma.

I would like to thank the help and resources I received from the ExOne Company, provided by Dan Brunermer, Bob Wood, Rick Lucas, Phil Lane, and Kevin Handerhan.

I would like to thank Steve Hudelson and Michael Gibson for giving me an opportunity to make a broader contribution to Binder Jetting and Additive Manufacturing.

Finally, I would like to thank my parents, Yusheng Bai and Sujuan Zhang, for their unconditional love and support; and my wife, who is also my best friend, Mingfei Liu, for bringing the greatest joy to my life.

Table of contents

1. Introduction 1
   1.1. Additive Manufacturing of copper cellular materials 1
      1.1.1. Motivation 1
      1.1.2. Existing AM processes for copper 1
         1.1.2.1. Direct metal fusion processes 1
         1.1.2.2. Sheet lamination 2
         1.1.2.3. Indirect AM approach 2
   1.2. Binder jetting 2
      1.2.1. Process overview 2
      1.2.2. Process rationale 3
      1.2.3. Process limitations 3
   1.3. Overall research goal 4
   1.4. Research questions 5
      1.4.1. Research Question 1: Bimodal Powder Mixture 5
         1.4.1.1. Background 5
         1.4.1.2. Research gap 5
         1.4.1.3. Research question and hypothesis 5
      1.4.2. Research Question 2: Nanoparticle Binder 6
         1.4.2.1. Background 6
         1.4.2.2. Research gap 6
         1.4.2.3. Research question and hypothesis 7
      1.4.3. Research Question 3: Binder-powder Interaction 7
         1.4.3.1. Background 7
         1.4.3.2. Research gap 8
         1.4.3.3. Research question and hypothesis 8
   1.5. Dissertation roadmap 9
   1.6. References 10
2. Establishment of the manufacturing process for Binder Jetting of copper 15
   2.1. Additive Manufacturing of Copper 15
      2.1.1. Prior Work in Additive Manufacturing of Copper 15
      2.1.2. Rationale of Binder Jetting of copper 15
      2.1.3. Context 16
   2.2. Experimental procedure 16

2.2.1. Binder selection 17
2.2.2. Powder selection 17
2.2.3. Green part creation 17
2.2.4. Post-processing 18
2.2.5. Part characterization 18
2.3 Results and Discussion 19
2.3.1 Green part creation 19
2.3.2 Densification and shrinkage 21
2.3.3 Pore structure and distribution 23
2.3.4 Effect of reducing atmosphere on sintering 24
2.3.5 Tensile strength 25
2.4 Summary and future work 26
2.5 References 26
3. Effect of Particle Size Distribution on Powder Packing and Sintering in Binder Jetting of Copper 29
3.1. Introduction 29
3.1.1. Achieving full density in binder jetting of metals 29
3.1.2. Improving sintered density via bimodal powder mixtures 29
3.1.3. Context 30
3.2. Experimental Method 30
3.2.1. Powder selection and characterization 30
3.2.2. Powder packing density assessment 31
3.2.3. Printing process parameters 31
3.2.4. Post-processing and sintering 31
3.2.5. Green and sintered part characterization 31
3.3. Results and Discussion 32
3.3.1. Bimodal powder mixture's impact on powder packing 32
3.3.1.1. Particle size distribution 32
3.3.1.2. Measured powder density and printed part green density 32
3.3.1.3. Powder flowability 33
3.3.2. Sintered density and shrinkage of bimodal powder mixtures 33
3.3.3. Influence of sintering conditions on bimodal powder mixtures 34
3.3.3.1. Effect of isotherm temperature and duration 34
3.3.3.2. Effect of heating ramp 35
3.3.4. Microscopic analysis of sintered bimodal powder parts 35
3.3.5. Discussion 36

3.4. Conclusion 38
3.5. References 39
4. Effect of Inkjetted Nanoparticles on Metal Part Properties in Binder Jetting Additive Manufacturing 41
4.1. Introduction 41
4.1.1. Binder selection in binder jetting of metals 41
4.1.2. Roadmap 42
4.2. Experimental methods 42
4.2.1. Material systems 43
4.2.2. Specimen manufacturing process 43
4.2.3. Printed part characterization 45
4.3. Results 45
4.3.1. Jetting colloidal organic binder 45
4.3.1.1. Green and sintered part density 45
4.3.1.2. Microstructure-property relationship 47
4.3.2. Jetting inorganic nanosuspension as the binder 48
4.3.2.1. Nanoparticle bonding 48
4.3.2.2. Green part properties 49
4.3.2.3. Sintered part properties 50
4.4. Conclusions 53
4.5. References 54
4.6. Appendix A: Electron micrographs of the sintered inorganic nanosuspension inks on solid substrates 56
5. Interaction between Nanoparticle Suspension Binder and Metal Powder in Binder Jetting Additive Manufacturing Process 57
5.1. Introduction 57
5.1.1. Binder-powder interaction 57
5.1.2. Nanoparticle suspension binders 58
5.1.3. Context 59
5.2. Powder bed sessile drop goniometry 59
5.2.1. Physical picture of binder-powder interaction 60
5.2.2. Defining a metric for describing the binder-powder interaction 61
5.2.3. Deriving dynamic contact angle 62
5.2.4. Powder granulation and equilibrium binder saturation ratio 63
5.3. Experimental methods 64

5.3.1. Nanoparticle binder preparation and characterization 64
5.3.2. Powder preparation 65
5.4. Results and discussion 66
5.4.1. Ink rheology and jettability 66
5.4.2. Binder-powder interaction 67
5.4.2.1. Powder bed sessile drop goniometry 67
5.4.2.2. Dynamic capillary contact angle 69
5.4.3. Primitive formation 70
5.4.3.1. Binder penetration 70
5.4.3.2. Equilibrium binder saturation ratio 71
5.4.4. Application 72
5.5. Conclusions 73
5.6. References 74
6. Additive Manufacturing of Metal Parts from Jetting a Particle-free Metal Ink as Binder Precursor for Binder Jetting 77
6.1. Introduction 77
6.1.1. Polymer binder vs. metal binder 77
6.1.2. Review of metal inks used in binder jetting 78
6.1.2.1. Particle suspension metal inks 78
6.1.2.2. Metal salt inks 78
6.1.2.3. Metal-Organic-Decomposition (MOD) inks 79
6.1.3. Roadmap 80
6.2. Experimental methods 80
6.2.1. Ink formulation and synthesis 80
6.2.2. Ink rheology and metallization 81
6.2.3. Printing process and green part properties 81
6.2.4. Sintering and sintered part properties 82
6.3. Results and discussion 82
6.3.1. Ink rheology 82
6.3.2. Ink metallization 83
6.3.3. Green part properties 84
6.3.4. Sintered part properties 87
6.3.4.1. Sintered density and shrinkage 87
6.3.4.2. Surface morphology 90
6.4. Conclusions 90

6.5. References 91
7. Conclusions and broader impacts 93
7.1. Summary of research 93
7.1.1. Research Question 1 93
7.1.2. Research Question 2 94
7.1.3. Research Question 3 96
7.2. Limitations and future work 96
7.2.1. Generalization of the results 97
7.2.2. Material systems used for experimentation 97
7.2.3. Characterizing the binder-powder interaction in binder jetting 97
7.3. Publications 97
7.4. Research contributions 98
7.5. Broader impacts 99

List of figures

Figure 1.1 Binder jetting of metal manufacturing process 3
Figure 2.1 Binder Jetting process schematic 16
Figure 2.2 The heating schedules used for sintering copper: (left) in air/vacuum and (right) in reducing atmosphere 18
Figure 2.3 16 µm powder SEM (left) and particle size distribution (right) 20
Figure 2.4 15 µm powder SEM (left) and particle size distribution (right) 20
Figure 2.5 75 µm powder sintered in pure hydrogen at 1000 °C for 8 hours. Left: sintered copper samples. Right: SEM of the sintered copper particles 21
Figure 2.6 Sintered density/shrinkage vs. sintering temperature of 15 µm powder and 16 µm powder (both sintered in hydrogen/argon for 2 hrs.) 22
Figure 2.7 Sintered density/shrinkage vs. sintering time of 15 µm powder (60% and 80% binder saturation), both sintered in hydrogen/argon at 1080 °C. 22
Figure 2.8 Complex shaped copper made via Binder Jetting 23
Figure 2.9 Percent porosity measurement using micrographs of the sectioned copper sample (15 µm powder sintered at 1080 °C/240 min.) 24
Figure 2.10 SEM of sintered 15 µm powder (1080 °C, 2 hours) at magnifications of (a) 200x, (b) 500x and (c) 2000x 24
Figure 2.11 Tensile test specimen sintered at 1060 °C (top) and 1080 °C (bottom) 25
Figure 3.1 Comparison of apparent density, tap density and green density for different powders 33
Figure 3.2 Sintered density and volumetric shrinkage of 5 µm powder and its bimodal mixtures, sintered at 1080 °C for 2 hours 33
Figure 3.3 Sintered density and densification comparison under various sintering conditions (error bars are constructed with the min and max of the data) 34
Figure 3.4 Sintered density of loosely packed powders in crucible with different heating rates 35
Figure 3.5 Surface microscopic images of bimodal powder parts sintered at 1060 °C for 120 minutes: (a) 75+15 µm powder (800X) and (b) 30+5 µm powder (2000X) 36
Figure 3.6 Optical microscopy of (a) 5 µm powder and (b) 30(73%) + 5 µm powder, sintered under the conditions in Section 3.3.2 36
Figure 3.7 Prediction model (line) and experimental results (dot) in specific volume and density of 15+5 µm powder mixture 37
Figure 3.8 Prediction model (line) and experimental results (dot) in specific volume and density of 30+5 µm powder mixture 37
Figure 3.9 An illustration of the relationship between the constituent powder shrinkage and the design of powder mixtures for maximum sintered density (the separation line is only representative in this figure and needs to be determined for each powder mixture based on particle size ratios) 38
Figure 4.1 Schematics of the use of colloidal organic binder and nanosuspension at different stages of binder jetting 42
Figure 4.2 TGA of the tested binders 44
Figure 4.3 Green density of polymer binder and nanoparticle-polymer suspension printed parts 46
Figure 4.4 Sintered density vs. sintering shrinkage of organic binder and nanoparticle-polymer suspension printed parts (sintered at 1075 °C for 120 min.) 46
Figure 4.5 Sintered density vs. sintering shrinkage of organic binder and nanoparticle-polymer suspension printed parts (sintered at 1075 °C for 600 min.) 47
Figure 4.6 Metallographic analysis (100x) of polymer binder printed parts (200% binder saturation), sintered at 1075 °C for 120 min. (left) and 600 min. (right) 47

Figure 4.7 Metallographic analysis (100x) of nanoparticle in polymer binder printed parts (200% binder saturation), sintered at 1075 °C for 120 min. (left) and 600 min. (right) 48
Figure 4.8 Ultimate tensile strength comparison between parts sintered at 1075 °C for 120 min. (left) and 600 min. (right) 48
Figure 4.9 Electron micrographs of the surface of green parts printed by polymer binder (left) and nanoparticle suspension (right) following the curing condition in Table 4.2 49
Figure 4.10 Electron micrographs at 20kx (left) and 50kx (right) of the nanoparticle bonding formed after curing at 260 °C 49
Figure 4.11 Flexural strength of printed green parts after curing at different temperatures 50
Figure 4.12 Green density of polymer binder and nanoparticle suspension printed parts 50
Figure 4.13 Sintered copper parts printed by the nanosuspension with different binder saturation ratios . 51
Figure 4.14 Sintered density vs. sintering shrinkage after sintering at 1075 °C for 120 min. (left) and 600 min. (right) 51
Figure 4.15 Sintered density vs. binder saturation ratio after sintering at 1075 °C for 120 min. (left) and 600 min. (right) 51
Figure 4.16 Sintering shrinkage (left) and sintered density (right) vs. weight percentage of large powder particles in the printed parts, after sintering at 1075 °C for 600 min. 52
Figure 4.17 Density of parts made by bimodal powder after sintering at 1075 °C for 600 min. 52
Figure 4.18 Overhang structure after sintering without supports, printed by: polymer binder printed with 100% binder saturation ratio (A), nanoparticle suspension printed with 70% (B) and 140% (C) binder saturation ratio 53
Figure 4.19 Electron micrographs of the inorganic copper nanosuspension heated on a silicon wafer in hydrogen atmosphere, at (A) 190 °C, (B) 250 °C, (C) 400 °C and (D) 600 °C 56
Figure 4.20 Electron micrographs of the inorganic copper nanosuspension heated on a silicon wafer in at 250 °C, in an atmosphere of (A) hydrogen, (B) nitrogen and (C) air 56
Figure 5.1 Overlapping primitives to form printed parts 57
Figure 5.2 Linking binder rheology to binder-powder interaction and primitive formation using the dynamic contact angle in capillaries 59
Figure 5.3 Recorded contact angle from initial contact (left) to completed absorption (right) 60
Figure 5.4 Binder-powder interaction and primitive formation process in binder jetting 60
Figure 5.5 Static contact angle at solid-liquid-vapor interface 61
Figure 5.6 Apparent contact of binder spreading on powder bed (θa) vs. dynamic wetting contact angle in the powder capillary pores (θd) 61
Figure 5.7 Typical capillary-saturation curve for liquid-powder interaction 64
Figure 5.8 Particle size distribution of tested powders 65
Figure 5.9 Viscosity of polymer binder and nanoparticle-polymer dispersions at different solid loading . 66
Figure 5.10 Fractional viscosity versus nanoparticle volume fraction with a curve fitted model 66
Figure 5.11 Inkjet testing of polymer binder (A), 15wt% (B) and 22.5 wt% (C) nanoparticle binder 67
Figure 5.12 Measured apparent contact angle as binder penetrates into the (A)75 μm, (B) 30+5 μm, and (C) 17 μm powder with a decreasing pore size of 12.2 μm, 2.8 μm, and 2.5 μm respetively 68
Figure 5.13 Penetration time vs. solid loading of nanoparticles for different powder 68
Figure 5.14 Dynamic contact angle vs. solid loading of nanoparticles for different powder 69
Figure 5.15 Calculated capillary number for each binder-powder combination 70
Figure 5.16 Top view (A) and side view (B) of powder granule generated from binder sessile drop absorbed into powder 70
Figure 5.17 Normalized radial diameter and vertical depth of the binder agglomerated powder generated from the binder penetrating powder goniometry 71

Figure 5.18 The equilibrium binder saturation ratio vs. nanoparticle solid loading for different powders 71
Figure 5.19 The relationship between the capillary pressure and equilibrium binder saturation ratio 72
Figure 5.20 Overlapping of printed primitives with a drop spacing of *dX* and *dY* 73
Figure 6.1 Jetting an organic adhesive as the binder 77
Figure 6.2 Jetting a nanoparticle suspension as the binder 78
Figure 6.3 Comparison between jetting a nanoparticle suspension (with particles) and MOD ink (particle-free) as the binder..... 80
Figure 6.4 Viscosity of the copper MOD ink in the solvent with different concentrations, compared to the polymeric binder 82
Figure 6.5 Pendent drop of 50% MOD ink, with a calculated surface tension of 29.42 mN/m 83
Figure 6.6 SEM images of copper MOD ink, heated at 250 °C for 3 hours in hydrogen (left, 100kx), nitrogen (middle, 100kx), and air (right, 50kx), with copper weight percent measured by EDS of 98.2%, 93.9% and 77.4%..... 83
Figure 6.7 Thermographic analysis of copper MOD in (50 wt% compound in solvent) and polymer binder 84
Figure 6.8 SEM images of the green parts printed with MOD ink (150% binder saturation, without post-print curing): 1kx (left) and 5kx (right) magnification rate 85
Figure 6.9 MOD printed part (18×6×3 mm) with (a) 150% saturation ratio and (b) 75% saturation ratio, after retrieving from the powder bed without post-print curing 85
Figure 6.10 SEM images of the powder particle bonding formed by sintered copper nanoparticles (150% saturation): 5kx (left) and 20kx (right) magnification rate 85
Figure 6.11 Green density of MOD ink printed and polymeric binder printed parts..... 86
Figure 6.12 Optical microscopic images of the sectioned and polished sintered parts, printed by (a) MOD ink and (b) polymeric binder, using 150% binder saturation ratio 87
Figure 6.13 Porosity distribution analysis by separating large and small pores from Figure 6.12: (a) large pores in MOD ink parts, (b) small pores in MOD ink parts, (c) large pores in polymer binder parts, and (d) small pores in polymer binder parts 87
Figure 6.14 Porosity measurement (by optical pixel counting) for MOD ink printed part (Figure 6.12): core section only (1.1%), large pores (4.86%), and small pores (0.86%)..... 88
Figure 6.15 Porosity measurement (by optical pixel counting) for polymer binder printed part (Figure 6.12): core section only (5.4%), large pores (1.97%), and small pores (2.40%) 88
Figure 6.16 Sintered density measured with oil impregnation 89
Figure 6.17 Volumetric shrinkage of the sintered part 89
Figure 6.18 SEM images (100x magnification) of sintered part surface (sintered at 1075 °C), for surface morphology comparison between parts printed by (a) polymeric binder, (b) 150% saturation MOD ink, and (c) 75% saturation MOD ink..... 90

List of tables

Table 1.1 Summary of research questions 10
Table 2.1 Particle size, packing density, and purity of received copper powders 19
Table 2.2 Printing parameters for the green part creation 20
Table 2.3 The highest achievable sintered density and volumetric shrinkage 23
Table 2.4 Chemical composition comparison before and after sintering in a reducing atmosphere 25
Table 2.5 Densification comparison between parts sintered in reducing and non-reducing atmospheres (15 µm powder sintered at 1060 °C for 2 hours) 25
Table 2.6 Ultimate tensile strength of specimen (15 µm powder) sintered with various temperatures 26
Table 3.1 Copper powders used for creating mixtures 31
Table 3.2 Particle size and density of the powder mixtures 32
Table 4.1 Measured drop volume and adopted binder saturation ratio 43
Table 4.2 Drying conditions used for the printing of the tested binders 44
Table 4.3 Carbon content in sintered parts measured by different spectroscopy methods 53
Table 5.1 Summary of powder properties 65
Table 5.2 Summary of rheology and calculated Oh numbers for polymer binder and nanoparticle-polymer dispersions at different solid loading 67
Table 5.3 Printing parameter selection for 17 µm powder 73
Table 6.1 Summary of binder rheology and jettability 83
Table 6.2 Before and after depowdering comparison of the green parts cured at different temperatures for 1 hour in hydrogen 86
Table 7.1 Summary of the nanoparticle binders used in this work 95

1. Introduction

1.1. Additive Manufacturing of copper cellular materials

1.1.1. Motivation

Copper is among the most conductive metallic materials and its thermal conductivity is only second to silver. Additive Manufacturing (AM) of copper could have impact on several applications that leverage the thermal/electrical conductivity of this material. For example, copper AM could enable the creation of highly efficient thermal management systems by leveraging the geometric design freedom offered by the AM's layer-by-layer approach. One of the applications for AM of copper is to create compact heat exchangers featuring complex cellular array of intake and exhaust passages to manage the thermal loads in high energy density power generators for portable electronic devices.

1.1.2. Existing AM processes for copper

Driven by the need to enable the AM a highly conductive material, research on AM of copper and copper alloys have been conducted on various AM platforms.

1.1.2.1. Direct metal fusion processes

Copper and its alloys have been additively manufactured with energy beam in Powder Bed Fusion processes. In laser-based Powder Bed Fusion AM systems, a laser is used to scan powder bed and selectively melt pure copper [1,2], copper alloys [3–6], and copper/copper alloy blends (liquid-phase sintering) [7,8]. However, copper is strongly reflective to laser energy (e.g., only about 10% energy absorption for a laser wavelength of 1.06 μm at room temperature) and therefore requires high laser power to melt (e.g., more than 300W is required with a pulsed Nd:YAG laser) [9]. As a result, in order to fully melt copper powder layers and produce high density parts, ultra-high energy density laser beam was adopted through high power lasers, small beam spot (100 μm) [5], or optimized scanning pattern [1] to compensate for the energy loss. A density higher than 90% can be typically achieved, as reported in the literature, among which the highest density reported is 99.9%.

Copper has also been printed with laser in Directed Energy Deposition systems [10,11]. In addition to the low energy absorption problem with laser, solidification cracking is likely to occur at the substrate interface when copper is deposited onto a dissimilar material substrate (e.g., steel). The deposited copper typically has porosity in the range of 10-15% volume fraction, with an approximately 10% deduction in thermal conductivity [11].

The use of electron beam, an alternative energy source to lasers, overcomes the optical reflectivity issues found in copper. Researchers have demonstrated some success in Electron Beam Melting (EBM) of high purity copper [12–20]. Ramirez *et al.* used EBM to manufacture pure copper into reticulated mesh and open cellular foam structures [17], and Yang *et al.* used EBM to manufacture pure copper into lattice structures [20]. Solid copper parts were also created with a fractional density of 89.5%, where the porosity was attributed to "unconsolidated or unmelted regions" and copper oxide precipitates. More recent development has led to near full density (99.9%) and wrought-equivalent conductivities (390 W/m*K) in high purity copper processed by EBM [13,15,16].

While direct metal AM processes are viable means for fabricating highly dense metal parts and have shown success in processing copper and copper alloys, the high thermal conductivity of copper remains a major challenge to obtain satisfactory printed part quality with ultimate process control. The resulting large thermal gradients from a moving point source of energy cause residuals stresses from rapid heating, cooling, thermal expansion and contraction. The residual stresses typically require anchors or heatsinks to keep the part from warping, which limit part scalability and add complexity to part post-

processing. In addition, conductive materials can be difficult to process within powder beds as heat rapidly dissipated from the intended melt region. As more energy is needed for intentional melting, the melting pool size is hard to control, and unintentional partial melting of surrounding powder can occur resulting in rough surface finish.

1.1.2.2. Sheet lamination

Sheet Lamination is an ultrasonic additive manufacturing (UAM) process used to produce parts of near net shape from successive joining metal tapes. As the sheet lamination process does not involve melting and combines the advantage of additive and subtractive manufacturing, it allows the manufacturing of metal parts with dimensional accuracy that is free of residual stress. However, its uses can be limited by the interlayer defects, heterogeneous microstructures, and anisotropic material properties in printed parts [21].

With a thorough demonstration with aluminum alloys, the capability of this manufacturing process has been extended to high purity copper. Electrolytic copper foils have been used to fabricate copper parts through copper-copper bonding [22] and multi-material parts through copper-to-aluminum bonding [23,24].

In the sheet lamination process of copper, the oxidation of copper foils has been identified as a major challenge to achieve satisfactory interlayer copper bonding. To overcome barrier of copper oxidation layers and promote stronger metallurgical bonding of copper, a higher power ultrasonic system (9 kW) was used to increase the bonding temperature leading to enhanced dynamic recrystallization and plastic flow [22,25]; and a post-deposition surface machining step was introduced to remove surface roughness and oxides on copper foils [23,24].

1.1.2.3. Indirect AM approach

Copper can be manufactured by additively manufacturing preforms containing metal and binders, which are converted to copper parts in post-processing steps. Copper powders can be mixed into photopolymer resins, thermoplastic filaments or low melting point polymer powders to be printed into green parts by Vat Photopolymerization, Material Extrusion, or Powder Bed Fusion AM processes respectively. The final copper products can be obtained by pyrolizing binders and sintering the printed green parts. The indirect AM approaches are advantageous in terms of cost and can be integrated into low cost desktop AM systems, but the sintered metal part quality is typically compromised due to the large amount of binder that needs to be debinded via a sintering process.

For example, polymer Powder Bed Fusion has been used to indirectly fabricate metal parts from metal-polymer powders [26,27], in which the laser selectively scanned a bed of a copper-polymer powder mixture to melt the polymer, which acted as an intermediate binder to create copper green parts. As the green density is relatively low (under 27%) due to the high mixing ratio of polymer, the sintered parts suffer from significant porosity, and impurities caused by the residual ash from binder burn-off.

1.2. Binder jetting

Understanding the limitations and challenges in the existing AM processes, the author looks to binder jetting as a suitable AM technology for printing complex geometries of high purity copper.

1.2.1. Process overview

Binder jetting can be used to fabricate metal parts by selectively inkjet printing a liquid binding agent into a powder bed, followed by a post-process sintering of the printed parts. As shown in Figure 1.1, a thin layer of powder is spread across the build piston, and the jetted binder droplets interact with the powder particles to form a cross-sectional layer. Once a layer is printed and thermally cured by a heater, a

new layer of powder is recoated on top of the printed layer which is then jetted with binder and stitched to the previous layers. The layer-by-layer process is repeated to create the complete green part with specified dimensions. Once the unbound loose powder that surrounds a part is removed (depowdering), the printed green part is placed in a furnace to fuse powder particles (sintering) and obtain final density and strength.

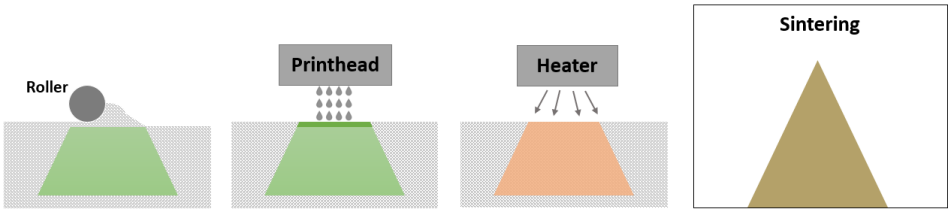

Figure 1.1 Binder jetting of metal manufacturing process

1.2.2. Process rationale

Binder jetting of metals is unique compared to direct metal AM processes as it separates geometry creation from metallurgical transformation. This fundamental difference makes binder jetting a suitable process to fabricate complex copper geometries, as it circumvents the limitations in (i) creating controlled melt pool in a powder bed of conductive materials, (ii) absorbing laser energy in optically reflective materials, and (iii) removing printed anchors and supports which adds design constraints and process cost. A summary of advantages in using binder jetting to print metal is provided.

- *No support or anchor structure needs to be printed.* As Binder jetting of metals functionally separates part creation from thermal processing, the common challenges found in direct-metal AM processes – such as residual stresses imposed by thermal gradient and requirement of anchors and/or heat sinks added to the geometry – are avoided. The ability to fabricate a part in a powder bed without the need for built anchors enables binder jetting to create large, geometrically complex parts without the need for laborious support/anchor removal in post-processing printed metal parts.
- *Large material selection.* Binder jetting is readily adaptable to a wide range of materials: polymers, ceramics and metals. As Binder Jetting does not use an energy beam to process material, it is well suited for optically reflective and thermally conductive metals. The microstructure in printed metal parts is more homogeneous and predictable than solidified molten metal.
- *Large scale and high throughput.* As it does not require an enclosed chamber and expensive energy beam sources, binder jetting is an inherently scalable technology. Binder jetting commercial systems can have large build volumes: ExOne offers build volumes of up to 780 x 400 x 400 mm for metal powders; VoxelJet offers a “continuous” sand printer that has a print width and height of 850 x 500 mm and does not restrict the length.
- *Cost effective.* Binder jetting systems are low cost compared to direct metal AM systems and the powder used for printing is 100% recyclable as the printing process does not involve high temperature and thermal degradation of powders.

1.2.3. Process limitations

While advantages exist for binder jetting, the success of manufacturing metal parts can be challenged by the difficulty to produce fully dense parts and maintain geometrical accuracy after large degree of sintering shrinkage.

Removing porosity in sintered components is critical to deliver targeted electrical and thermal conductivity performance metrics [28,29]; however, achieving fully dense sintered parts is a primary challenge in binder jetting of metals, mainly because of the loosely packed powder bed and incompatibility with ultra-fine powder feedstock [30]. While small particles are critical for providing

sintering stress for densification, their use in binder jetting needs to be in small volume percentage and the size cannot be smaller than 1 μm to avoid large inter-particular friction that lowers powder flowability for successful recoating [31]. The limited mobility of ultra-fine powder also leads to reduced powder packing efficiency, which generates less powder contacting points and large powder voids that are harmful for achieving high sintered density. Several techniques exist to address the powder packing issues in binder jetting, including spray-dried granules and slurry-based powders to accommodate for the use of fine powders [32,33], and powder compaction mechanism to improve powder packing [34]. Near full density in binder jetting can be achieved through liquid-phase sintering, but its use is limited to specific alloys or sintering aids [35–37], which is not suitable for sintering single phase materials (e.g., high purity copper). In commercial practice of binder jetting, infiltrating the printed metal skeleton with a lower melting point material during sintering is a common method to achieve full density and minimize shrinkage [38], but is always accompanied by material heterogeneity.

As sintering densification is always accompanied by dimensional shrinkage, a predictable and consistent shrinkage is important to ensure geometrical accuracy through compensating model dimensions. Yet less shrinkage is generally preferred as it can improve the reliability in predicting sintered part dimensional, except for the cases where large shrinkage is desired to produce small feature size [32]. Large degree of shrinkage should be avoided also because it is usually associated with shape distortion [39], and it imposes challenges in the use of support material to prevent slumping of overhang structures as it can be hard to remove from shrunk confined space.

In addition to the sintering densification issue, the success in binder jetting of metal is also challenged by (i) a lack of fundamental understanding of the printing process, and (ii) limited binder selections. The printing parameters are typically determined by experimental design [40], due to a lack of the fundamental understanding of binder-wetting-powder process and how it correlates to printing parameter selection. The binder selection is also limited for printing metals. While a commercially available organic binder material exists with success of printing a large variety of metallic materials, the debinding of organic matters can leave carbon residual that is harmful for high conductivity applications, and compromises structural integrity as it burns out at low temperatures where sintering bond is still weak.

1.3. Overall research goal

Overall Motivation
Establish a manufacturing process and material system for fabricating high purity copper parts with reduced porosity, less shrinkage, and improved structural integrity.

The overall motivation of this work is to address the limitations identified in Section 1.2.3, and establish a manufacturing process chain and material system that is suitable for fabricating high purity copper parts with better dimensional accuracy, structural integrity, and thermal conductivity. Driven by this overall motivation goal, a methodology is proposed to increase powder bed packing density via filling powder bed interstitial voids with small particulates, through mixing fine powders into the powder bed and/or adding nanoparticles into the binder.

Through the investigation of the developed new material systems, a fundamental understanding of binder jetting is gained through establishing process-structure-property relationships, and creating a new method to characterize and understand the binder-powder interactions that can provide guidance for material screening and printing parameter selection. The development of this fundamental understanding is guided under a primary research goal:

Primary Research Goal
To gain an understanding of how fine particulates added to a powder bed affect the printed part properties and binder-powder interactions in binder jetting of metal.

1.4. Research questions

To achieve the primary research goal, three research questions are developed to guide this dissertation. Research Question 1 and 2 focus on understanding how printed part density is affected by adding smaller particles into the powder bed (bimodal powder mixture) and into the binder (nanoparticle binder). Research Question 3 explores how the binder jetting process (e.g., binder wetting/penetrating powder) is affected by the material systems containing fine particulates.

1.4.1. Research Question 1: Bimodal Powder Mixture

1.4.1.1. Background

Using bimodal powder mixtures to replace monosized powder is a well-established practice to improve powder packing and thus increasing green density in powder metallurgy. However, compared with the certainty and reliable prediction in improving powder packing and green density by bimodal powder, the sintered density improvement is often complicated and uncertain. While small particles have rapid sintering rate and enhanced sintering stress [41], the added smaller particles may bond to the large particles and offer little influence on the overall densification. The addition of coarse powders to a fine powder matrix may increase the packing density, but the difficulty to sinter large particles also hinders densification. German developed a prediction of sintered density of bimodal mixtures and validated with a series of experiments using various materials [42]. In this prediction, the sintered density is predicted by accounting factors including particle size ratio, constituent powder packing density and sintering shrinkage, and powder mixing homogeneity. Both experimental and prediction results have shown that only fine powder constituent should be used rather than the bimodal mixture in order to achieve the maximum sintered density.

1.4.1.2. Research gap

The use of bimodal powder mixture has been explored in AM contexts [43,44], however, the study of sintering bimodal powder mixtures in the context of binder jetting of metals is limited. Lanzetta *et al.* studied the improved surface finish and printed primitive morphology in unfired bimodal powders parts [45]. Verlee *et al.* explored the sintered density of stainless steel bimodal mixtures and compared with the German model; similar to the practice in traditional powder metallurgy, the highest sintered density was obtained when using pure fine powders [46].

In the prior art of binder jetting using bimodal powder mixtures, the studied particle size range is in 16-90 μm. There exists a need to investigate bimodal powder mixtures containing smaller parts, as the sintering of ultra-fine powders (<10 μm) printed in binder jetting can be strongly affected by the poor powder packing due to the limited powder flowability. It is unknown whether binder jetting is different than traditional powder processing techniques in terms of influencing sintered density by mixing coarse particles into ultra-fine powders.

1.4.1.3. Research question and hypothesis

To address this research gap, bimodal powder mixtures are investigated in the context of binder jetting guided by Research Question 1. Understanding that the poor flowability of ultra-fine powders in binder jetting typically results in low sintered density as a result of less particle contact points and large voids in powder bed and printed green part, it is hypothesized that bimodal powder mixture is capable of

producing higher sintered density compared to only using fine powders, by overcoming the poor powder flowability and packing of fine powders.

Research Question 1:
How does the powder bed of a bimodal powder mixture affect the green/sintered density and shrinkage of binder jetting printed parts?
Hypothesis 1:
Unlike the conventional powder metallurgy processes where high sintered density is typically achieved through sintering the monosized fine powder constituent, in binder jetting the use of a bimodal powder mixture over the poorly packed ultra-fine powder constituent can increase sintered density with reduced shrinkage.

1.4.2. Research Question 2: Nanoparticle Binder

1.4.2.1. Background

Powder bed interstices can be also filled with small particles by jetting binders that contain metal contents. Compared to the commonly used organic binders in binder jetting of metals, it is hypothesized that a metal binder can bring several benefits to green and sintered part properties.

- The deposition of metal binders adds additional metal content to the powder bed voids, and therefore can improve printed green part density.
- The metal nanoparticles jetted into the powder bed interstices can be sintered at lower temperatures than bulk powder particles, and therefore can provide additional inter-particle bonding to increase the green part strength after curing the printed part with low temperature. This feature has a potential to eliminate the need of a polymeric adhesive and enable the use of nanoparticle ink as the binder.
- Unlike sacrificial organic binder that needs to be debinded prior to final stage of sintering during heat treatment, the jetted metal nanoparticles can act as a permanent binder that provides constant bonding strength to the printed parts throughout heat treatment, thus preventing part warping or slumping caused by the loss of bonding strength due to debinding.

1.4.2.2. Research gap

The benefits of nanoparticles have been demonstrated in prior art where printed and presintered powder skeleton can be infiltrated with nanoparticles to improve creep resistance and density [47,48]. Nanoparticles can be also jetted to powder bed by suspending into the existing organic binder used for printing, with demonstrated benefits to reduce sintering shape distortion [39], or achieve composition gradients in sintered parts [49].

It has been demonstrated in the literature that metal binders can be used to print refractory powders and eliminate the need of organic adhesives for powder bonding. Low melting point metal particles (e.g., iron, silver) can be created into suspensions and jetted into powder bed of high melting point metals (e.g., molybdenum); upon heating, the printed regions can form cohesive layers through molten or sintered metal particles, while the unprinted regions of the refractory powder bed remain unsintered [50,51]. Similarly, the metal binder can be also created in the form of metal salt solution, and used for printing refractory powders as a binder through sintering or melting precipitated particles upon heating [50–52].

While the use of nanoparticles in binder has been explored in the literature, there exists a lack of understanding of the process-property relationship when metal binder is used, and an opportunity to invent new material systems for binder jetting.

The prior art has explored the printing of a micro-sized silver powder with an organic binder suspended with silver nanoparticles [39]. While a proof of concept has been demonstrated for reducing sintering shrinkage with silver nanoparticle binder, the experiment did not contain process parameter variables to study the role of jetted nanoparticles. This work intends to address this gap in the literature, and study the relationship between printing parameters (e.g., binder saturation ratio) and printed part properties, to gain an understanding on the influence of jetted nanoparticles on sintering densification.

In the literature, the concept of using metal binder to replace organic binder is contingent upon the large sintering temperature gap between the base powder material and the metal binder material. As a result, only dissimilar material systems composed of refractory powders and low-melting-point-material binders have been used with the requirement of sintering the powder bed in high temperature. In a single-phase material system, the feasibility of printing a metal powder using an ink composing of the same metal as the binder, has not been demonstrated.

1.4.2.3. Research question and hypothesis

In order to further the understanding of the specified role played by jetted nanoparticles in binder jetting, there exists a need to evaluate green and sintered part properties in varied binder saturation ratios. Unlike sacrificial organic binders, a metal binder is permanent and structural, and therefore hypothesized to manifest a different relationship between binder saturation ratio and printed part properties.

It is also hypothesized that nanoparticle binders can substitute organic adhesives to print green parts with satisfactory strength. Enabled by the reduced melting and sintering temperature of nanoparticles, there exists a heating condition to sinter the nanoparticles jetted into a powder bed, without sintering the micron-sized powder particles in unprinted regions, which allows printed part retrieval from the powder bed.

Research Question 2:
How does the jetted nanoparticle affect printed green and sintered part properties?
Hypothesis 2.1:
Jetted nanoparticles can densify the printed green part and reduce sintering shrinkage. Higher sintered density with less sintering shrinkage can be produced by increasing the binder saturation ratio used for printing a nanoparticle binder.
Hypothesis 2.2:
A nanoparticles ink can be used as the binder to eliminate the need for an organic adhesive. A metallic binding mechanism is enabled through sintering the jetted nanoparticles into a powder bed that is heated below the powder sintering temperature, which (i) selectively fuses the powder bed and enable strength to the green part, and (ii) ensures printed part retrieval from the unsintered powder particles.

1.4.3. Research Question 3: Binder-powder Interaction

1.4.3.1. Background

With Research Question 1 and 2 positioned to explore how printed parts properties are affected by the fine particulates in powder bed delivered by bimodal powder (RQ1) or nanoparticle binder (RQ2), there is a lack of understanding of how the binder jet printing process is influenced by the new material systems (e.g., nanoparticle binder).

The binder permeation process and primitive formation is the very essence of the binder jet printing process. When a droplet is released from the inkjet nozzle and brought into contact with a powder bed, it begins to spread and penetrate into the powder. The result of binder imbibition into the powder is a powder-binder agglomerate formed within the loosely packed powder bed, which is also the primitive in

binder jetting as it is the fundamental building block that constitutes a printed part. Understanding the binder-powder interaction and knowing the primitive size is critical for the printing accuracy and finished material properties in binder jetting.

The capability of a binder wetting and penetrating into a powder constitutes the main criteria of determining the compatibility between a binder and powder. The metrics obtained from characterizing the interaction between binder and powder can therefore be used for screening material combinations and determining binder-powder compatibility. The resolution of the printed part of a material system can be derived when the primitive size and morphology is known.

Studying the binder-powder interaction can also guide the selection of printing parameters in binder jetting. The strength of a printed green part is gained from overlapping the primitives within a layer and stitching primitives across the printed layers. Therefore, the information of primitive size and morphology can guide the selection of layer thickness and binder droplet spacing, the two most essential printing parameters in binder jetting, to achieve desired primitive overlapping. Layer thickness and binder droplet spacing, along with a known droplet volume, can be used to calculate binder saturation ratio (defined as the ratio of total amount of binder verses total pore volume in a printed part).

1.4.3.2. Research gap

The fundamental theories for a fluid flow in a porous body driven by capillary forces have been established as Washburn Equations [53]. Further models have been then developed based on this understanding to describe the interactions between liquid and powders, by treating the pores in powder as straight capillary cylinders [54,55].

Recognizing the importance of understanding the binder-powder interactions, capillary models have been applied in the binder jetting context. Holman *et al.* studied how binder infiltration rate is affected by the pore size in slurry-based ceramic powder beds, and how it determines the drop diameter (drawing area) on powder [56]. Miyanaji *et al.* addressed the binder imbibition and drainage behaviors inside powder pores by establishing a relationship between capillary pressure and binder saturation level at equilibrium state of binder permeation [57].

The interaction between binder and powder ultimately determines the morphology of the resultant binder-powder agglomerate (primitive) in binder jetting. Cima *et al.* created primitives by sieving printed individual binder-powder agglomerates from loose powder [58]. The printed primitives have shown spherical curvature and higher packing density than loosely packed powder, as a result of the surface tension in binder that rearranges powder particles.

Research gaps exist in that the effect of the suspended nanoparticles in a binder on powder wettability and primitive size is unknown. More importantly, there is a need to (i) develop a metric to define powder wettability and describe binder-powder interactions for binder jetting, (ii) and understanding how binder-powder interactions affect the primitive formation process. It is noticed that describing the powder wettability by contact angle is insufficient for binder jetting as it does not account for the binder penetration. This work aims to create a tool to experimentally evaluate the binder permeation and powder granulation process, which can be then applied in the context of nanoparticle binder.

1.4.3.3. Research question and hypothesis

Research Question 3 therefore is developed to gain the understanding on the nanoparticle binder's impact on the binder permeation process and printed primitive size. It is hypothesized that the suspended nanoparticles impose strong influence on binder rheology, which ultimately affects the binder penetration

process powder wettability. It is also hypothesized that the powder wettability in binder jetting can be described by the contact angle formed at the interface between binder and powder pores, which also affects the binder penetration depth.

Research Question 3:
How does the solid loading of nanoparticles in a binder and the powder bed pore size affect the binder-powder interaction and resultant printed primitive size?
Hypothesis 3:
As the nanoparticle content increases, the binder surface tension decreases and viscosity increases, thus reduces the powder permeability through inhibited binder penetration. Smaller printed primitives are created as a result of the reduced powder permeability. The powder permeability is further reduced in smaller pore size powder beds as the binder penetration time decreases.

1.5. Dissertation roadmap

Chapter 2 presents the establishment of the material systems and manufacturing process chain for printing high purity copper. The challenges and process limitations in binder jetting of metal is identified through the preliminary exploration of the printed copper part properties in this chapter.

Chapter 3 discusses the use of a bimodal powder mixture as the powder bed for binder jetting of copper. The effect of the bimodal particle size distribution on the printed part properties is investigated under the guidance of Research Question 1, in an effort to overcome the limitations of powder bed packing density through filling the powder bed voids with smaller particles.

Binders can be also used to deposit smaller particles to the powder bed to fill the voids. Nanoparticle suspension binders are therefore investigated in Chapter 4 guided by Research Question 2, to study their effects on the printed part properties.

Understanding the use of a nanoparticle suspension binder can have a significant impact on its interaction with the powder bed and printing parameter selection, Chapter 5 is therefore dedicated to discuss how is the binder-powder interaction and printed primitive size affected by the presence of nanoparticles in a binder, under the guidance of Research Question 3.

Inspired by the work performed with the nanoparticle suspension binder, a new concept on particle-free nanoparticle binder is discussed in Chapter 6. Designed to deliver a similar impact on the printed part properties as the nanosuspension binder, the particle-free binder can circumvent the complexity added to the binder jetting process by the suspended particles.

A summary of the research questions with the corresponding chapter and publication is provided in Table 1.1.

Table 1.1 Summary of research questions

Research Question	*Chapter*	*Journal publication*
Establishment of the manufacturing process	2	Bai, Y., Williams, C.B., 2015, An exploration of binder jetting of copper", *Rapid Prototyping Journal*, Vol. 21 Issue: 2, pp.177-185
RQ 1: bimodal powder mixture	3	Bai, Y., Wagner, G., Williams C.B., 2017, Effect of Particle Size Distribution on Powder Packing and Sintering in Binder Jetting Additive Manufacturing of Metals, *ASME. J. Manuf. Sci. Eng.*,139(8)
RQ 2: nanoparticle binder	4	Submitted to Nanotechnology
RQ 3: binder-powder interaction	5	Submitted to Journal of Manufacturing Science and Engineering
RQ 2: particle-free binder precursor (MOD ink)	6	Bai, Y., and Williams, C. B., 2018, "Binder Jetting Additive Manufacturing with a Particle-Free Metal Ink as a Binder Precursor," *Mater. Des.*, 147.

1.6. References

[1] Lykov P.A., Safonov E.V., A. A. M., 2016, "Selective Laser Melting of Copper," Trans Tech Publ., 843, pp. 284–288.

[2] Pogson, S. R., Fox, P., Sutcliffe, C. J., and O'Neill, W., 2003, "The production of copper parts using DMLR," Rapid Prototyp. J., 9(5), pp. 334–343.

[3] Scudino, S., Unterdörfer, C., Prashanth, K. G., Attar, H., Ellendt, N., Uhlenwinkel, V., and Eckert, J., 2015, "Additive manufacturing of Cu–10Sn bronze," Mater. Lett., 156, pp. 202–204.

[4] Vinod, A. R., and Srinivasa, C. K., 2014, "Studies on laser-sintering of copper by direct metal laser sintering process," Proc. 5th Int. 26th All India Manuf. Technol. Des. Res. Conf. (AIMTDR 2014), (Aimtdr), pp. 377-1–4.

[5] Wu, W., Yang, Y., and Huang, Y., 2007, "Direct manufacturing of Cu-based alloy parts by selective laser melting," Chinese Opt. Lett., 5(1), pp. 37–40.

[6] Zhang, D. Q., Liu, Z. H., and Chua, C. K., 2014, "Investigation on forming process of copper alloys via Selective Laser Melting," High Value Manuf. Adv. Res. Virtual Rapid Prototyp. Proc. 6th Int. Conf. Adv. Res. Virtual Rapid Prototyping, Leir. Port. 1-5 October, 2013, p. 285.

[7] Tang, Y., Loh, H. T., Wong, Y. S., Fuh, J. Y. H., Lu, L., and Wang, X., 2003, "Direct laser sintering of a copper-based alloy for creating three-dimensional metal parts," J. Mater. Process. Technol., 140(1–3 SPEC.), pp. 368–372.

[8] Zhu, H. H., Fuh, J. Y. H., and Lu, L., 2005, "Microstructural evolution in direct laser sintering of Cu-based metal powder," Rapid Prototyp. J., 11(2), pp. 74–81.

[9] Naeem, M., 2013, "Laser Processing of Reflective Materials," Laser Tech. J., (1), pp. 18–20.

[10] Kadekar, V., Prakash, S., and Liou, F., 2004, "Experimental investigation of laser metal deposition of functionally graded copper and steel," International Solid Freeform Fabrication Symposium, pp. 198–202.

[11] Sciammarella, F. M., Gonser, M., and Styrcula, M., 2012, "Laser Additive Manufacturing of Pure Copper," RAPID Conference.

[12] Frigola, P., Agustsson, R., Boucher, S., Murokh, A., Badakov, H., Fukasawa, A., Musumeci, P., Rosenzweig, J., Travish, G., Faillace, L., La, R., Cormier, D., and Mahale, T., 2009, "Development of Solid Freeform Fabrication (SFF) for the Production of RF Photoinjectors EBM Fabrication Process," Proc. 23rd Part. Accel. Conf., pp. 2015–2017.

[13] Frigola, P., Harrysson, O. A., Horn, T. J., West, H. A., Aman, R. L., Rigsbee, J. M., Ramirez, D. A., Murr, L. E., Wicker, R. B., and Rodriguez, E., 2014, "Fabricating Copper Components with Electron Beam Melting," Adv. Mater. Process.

[14] Frigola, P., Agustsson, R., Boucher, S., Murokh, A., Rosenzweig, J., Travish, G., Faillace, L., Cormier, D., and Mahale, T., 2008, "A Novel Fabrication Technique for the Production of RF Photoinjectors," Proc. 11th Eur. Part. Accel. Conf. (EPAC 08), pp. 751–753.

[15] Lodes, M. A., Guschlbauer, R., and Körner, C., 2015, "Process development for the manufacturing of 99.94% pure copper via selective electron beam melting," Mater. Lett., 143, pp. 298–301.

[16] Raab, S. J., Guschlbauer, R., Lodes, M. A., and Körner, C., 2016, "Thermal and Electrical Conductivity of 99.9% Pure Copper Processed via Selective Electron Beam Melting," Adv. Eng. Mater., pp. 1661–1666.

[17] Ramirez, D. A., Murr, L. E., Li, S. J., Tian, Y. X., Martinez, E., Martinez, J. L., Machado, B. I., Gaytan, S. M., Medina, F., and Wicker, R. B., 2011, "Open-cellular copper structures fabricated by additive manufacturing using electron beam melting," Mater. Sci. Eng. A, 528(16–17), pp. 5379–5386.

[18] Ramirez, D. A., Murr, L. E., Martinez, E., Hernandez, D. H., Martinez, J. L., MacHado, B. I., Medina, F., Frigola, P., and Wicker, R. B., 2011, "Novel precipitate-microstructural architecture developed in the fabrication of solid copper components by additive manufacturing using electron beam melting," Acta Mater., 59(10), pp. 4088–4099.

[19] Ramirez, D. A., 2011, "Microstrutural Architecture Developed in the Fabrication of Solid and Open-cellular Copper Components by Additive Manufacturing Using Electron Beam Melting", Doctoral dissertation, The University of Texas at El Paso

[20] Yang, L., Harrysson, O., West II, H., and Cormier, D., 2011, "Design and characterization of orthotropic re-entrant auxetic structures made via EBM using Ti6Al4V and pure copper," International Solid Freeform Fabrication Symposium, pp. 464–474.

[21] Gibson, I., Rosen, D., and Stucker, B., Additive Manufacturing Technologies, Springer, 2015

[22] Sriraman, M. R., Babu, S. S., and Short, M., 2010, "Bonding characteristics during very high power ultrasonic additive manufacturing of copper," Scr. Mater., 62(8), pp. 560–563.

[23] Janaki Ram, G. D., Johnson, D. H., and Stucker, B. E., 2007, "Ultrasonic Consolidation with aluminum and copper," 3rd Int. Conf. Adv. Res. Virtual Rapid Prototyp. Virtual Rapid Manuf. Adv. Res. Virtual Rapid Prototyp., pp. 603–610.

[24] Truog, A. G., Sriraman, R. M., and Babu, S. S., 2013, “Surface Modification of Very High Power Ultrasonic Additive Manufactured (VHP UAM) Aluminum and Copper Structures,” Trends Weld. Res. Proc. 9th Int. Conf., pp. 757–762.

[25] Sriraman, M. R., Gonser, M., Fujii, H. T., Babu, S. S., and Bloss, M., 2011, “Thermal transients during processing of materials by very high power ultrasonic additive manufacturing,” J. Mater. Process. Technol., 211(10), pp. 1650–1657.

[26] Badrinarayan, B., and Barlow, J. W., 1992, “Metal Parts from Selective Laser Sintering of Metal-Polymer Powders,” International Solid Freeform Fabrication Symposium, (1), pp. 141–146.

[27] Badrinarayan, B., and Barlow, J. W., 1991, “Selective Laser Sintering of a Copper-PMMA System,” International Solid Freeform Fabrication Symposium, pp. 245–250.

[28] Montes, J. M., Cuevas, F. G., and Cintas, J., 2008, “Porosity effect on the electrical conductivity of sintered powder compacts,” Appl. Phys. A Mater. Sci. Process., 92(2), pp. 375–380.

[29] Rhee, S. K., 1975, “Porosity-Thermal conductivity correlations for ceramic materials,” Mater. Sci. Eng., 20(C), pp. 89–93.

[30] Utela, B., Storti, D., Anderson, R., and Ganter, M., 2008, “A review of process development steps for new material systems in three dimensional printing (3DP),” J. Manuf. Process., 10(2), pp. 96–104.

[31] Sachs, E. M., Cima, M. J., Caradonna, M. A., Grau, J., Serdy, J. G., Saxton, P. C., Uhland, S. A., and Moon, J., 2003, “Jetting layers of powder and the formation of fine powder beds thereby,” 1(12).

[32] Williams, C. B., Cochran, J. K., and Rosen, D. W., 2011, “Additive manufacturing of metallic cellular materials via three-dimensional printing,” Int. J. Adv. Manuf. Technol., 53(1–4), pp. 231–239.

[33] Holman, R. K., 2001, “Effects of the Polymeric Binder System in Slurry-Based Three Dimensional Printing of Ceramics”, Doctoral dissertation, Massachusetts Institute of Technology.

[34] Gregorski, S. J., 1996, “High green density metal parts by vibrational compaction of dry powder in three dimensional printing process,” Doctoral Dissertation, Massachusetts Institute of Technology.

[35] Do, T., Kwon, P., and Shin, C. S., 2017, “Process development toward full-density stainless steel parts with binder jetting printing,” Int. J. Mach. Tools Manuf., 121(April), pp. 50–60.

[36] Do, T., Shin, C. S., Stetsko, D., Vanconant, G., Vartanian, A., Pei, S., and Kwon, P., 2015, “Improving Structural Integrity with Boron-based Additives for 3D Printed 420 Stainless Steel,” Procedia Manuf., 1, pp. 263–272.

[37] Nandwana, P., Elliott, A. M., Siddel, D., Merriman, A., Peter, W. H., and Babu, S. S., 2017, "Powder bed binder jet 3D printing of Inconel 718: Densification, microstructural evolution and challenges," Curr. Opin. Solid State Mater. Sci., 21(4), pp. 207–218.

[38] Doyle, M., Agarwal, K., Sealy, W., and Schull, K., 2015, “Effect of Layer Thickness and Orientation on Mechanical Behavior of Binder Jet Stainless Steel 420 + Bronze Parts,” Procedia Manuf., 1, pp. 251–262.

[39] Bai, J. G., Creehan, K. D., and Kuhn, H. A., 2007, “Inkjet printable nanosilver suspensions for enhanced sintering quality in rapid manufacturing,” Nanotechnology, 18(18).

[40] Shrestha, S., and Manogharan, G., 2017, “Optimization of Binder Jetting Using Taguchi Method,” JOM, 69(3), pp. 491–497.

[41] Coble, R. L., 1973, “Effects of Particle-Size Distribution in Initial-Stage Sintering,” J. American Ceram. Soc., 56(9), pp. 461–466.

[42] German, R. M., 1992, “Prediction of sintered density for bimodal powder mixtures,” Metall. Trans. A, 23(5), pp. 1455–1465.

[43] Karapatis, N., and Egger, G., 1999, “Optimization of powder layer density in selective laser sintering,” International Solid Freeform Fabrication Symposium, pp. 255–264.

[44] Spierings, A. B., Herres, N., Levy, G., and Buchs, C., 2010, “Influence of the particle size distribution on surface quality and mechanical properties in additive manufactured stainless steel parts,” International Solid Freeform Fabrication Symposium, pp. 397–406.

[45] Lanzetta, M., and Sachs, E., 2003, “Improved surface finish in 3D printing using bimodal powder distribution,” Rapid Prototyp. J., 9, pp. 157–166.

[46] Verlee, B., Dormal, T., and Lecomte-Beckers, J., 2011, “Properties of Sintered Parts Shaped by 3D-Printing from Bimodal 316L Stainless Steel Powder Mixtures,” Euro PM2011, pp. 357–362.

[47] Crane, N. B., Wilkes, J., Sachs, E., and Allen, S. M., 2006, “Improving accuracy of powder-based SFF processes by metal deposition from a nanoparticle dispersion,” Rapid Prototyp. J., 12(5), pp. 266–274.

[48] Elliott, A., Alsalihi, S., Merriman, A. L., and Basti, M. M., 2016, “Infiltration of Nanoparticles into Porous Binder Jet Printed Parts,” Am. J. Eng. Appl. Sci., 9(1).

[49] Godlinski, D., and Morvan, S., 2005, “Steel Parts with Tailored Material Gradients by 3D-Printing Using Nano-Particulate Ink,” Mater. Sci. Forum, 492–493, pp. 679–684.

[50] Yoo, H. J., 1995, “Reactive binders for metal parts produced by Three Dimensional Printing”, Thesis, Massachusetts Institute of Technology.

[51] Hadjiloucas, C., 1997, “Low Shrinkage Metal Skeletons by Three Dimensional Printing”, Thesis Massachusetts Institute of Technology.

[52] Liu, J., 2009, “In Situ Created Metal Nanoparticle Strengthening of Metal Powder Articles”, US Patent Application No.: 2009/0007724 A1

[53] Washburn, E. W., 1921, “The dynamics of capillary flow,” Phys. Rev., 17(3), pp. 273–283.

[54] Denesuk, M., Smith, G. L., Zelinski, B. J. J., Kreidl, N. J., and Uhlmann, D. R., 1993, “Capillary penetration of liquid droplets into porous materials,” J. Colloid Interface Sci., 158(1), pp. 114–120.

[55] Hapgood, K. P., Litster, J. D., Biggs, S. R., and Howes, T., 2002, “Drop Penetration into Porous Powder Beds,” J. Colloid Interface Sci., 253(2), pp. 353–366.

[56] Holman, R. K., Cima, M. J., Uhland, S. A., and Sachs, E., 2002, “Spreading and infiltration of inkjet-printed polymer solution droplets on a porous substrate,” J. Colloid Interface Sci., 249(2), pp. 432–440.

[57] Miyanaji, H., Zhang, S., and Yang, L., 2018, “A new physics-based model for equilibrium saturation determination in binder jetting additive manufacturing process,” Int. J. Mach. Tools Manuf., 124(September 2017), pp. 1–11.

[58] Cima, M. J., Lauder, A., Khanuja, S., and Sachs, E., 1992, “Microstructural Elements of Components Derived From 3D Printing,” International Solid Freeform Fabrication Symposium, pp. 220–227.

2. Establishment of the manufacturing process for Binder Jetting of copper

2.1. Additive Manufacturing of Copper

One of the research opportunities identified in the 2009 Roadmap for Additive Manufacturing was to use Additive Manufacturing (AM) to create complex heat exchangers to enable a new generation of power generators for portable electronic devices [1]. Additive manufacturing's layer-by-layer approach, which offers the utmost design freedom in the realization of complex geometries, could enable the design and fabrication of highly efficient thermal management systems that feature a complex cellular array of internal intake and exhaust passages. To take advantage of this application opportunity, there is need for research to enable the creation of copper components via AM.

2.1.1. Prior Work in Additive Manufacturing of Copper

SLS has been used to indirectly fabricate pure metal parts from metal-polymer powders [2,3]. In their work, laser selectively scanned a bed of a copper-polymer powder mixture to melt the polymer, which acted as an intermediate binder to create copper green parts. The green parts were later sintered in hydrogen. The green density is relatively low (under 27%) due to the high mixing ratio of polymer, which introduced significant porosity in the sintered copper parts. Therefore, the authors turned to bimodal mixed powders and polymer-coated granules of small copper particle to increase the powder packing density. Impurities caused by the residual ash from binder burn-off were also introduced to the final products.

Pure copper parts were fabricated via Electron Beam Melting (EBM) for applications including RF photoinjectors [4], and honeycomb structures [5]. After the energy scanning parameter optimization, a nearly fully-dense state of copper was achieved. Problems in consistency, surface quality and dimensional accuracy were noticed in the experiments. These defects were believed to be caused by the severe dissipation of thermal energy during the melting process due to the high thermal conductivity of copper. In a different study, copper open-cellular structure was developed via EBM from atomized copper precursor powders [6–8]. This process was able to fabricate a wide range of density of copper metal foams, among which the highest relative density was 89.5%. Despite the porosity, the microstructural pictures have shown a complete interlayer fusion. Copper oxide precipitate in a columnar structure was observed in the copper parts, which was found to be able to increase hardness of the material.

Very high power UAM (Ultrasonic Additive Manufacturing), a laminate-based AM process that features high power, has been used to additively fabricate copper parts [9,10]. Tapes of high purity copper foil (150 μm thick) were successively stacked and joined via ultrasonic welding, during which process coarse-grained structures recrystallized and converted to fine grains at the joining interfaces. As the name suggests, higher power level (9 kW) was required because of the difficulties in depositing copper layers caused by material hardening and oxidation issues. Copper was also found to be capable of dissimilar joining with aluminum [11].

2.1.2. Rationale of Binder Jetting of copper

In this work, the author explores the use of Binder Jetting to create high purity copper parts. Binder Jetting is an AM process in which a liquid binding agent is selectively deposited to join powder materials (Figure 1). In the green part creation stage, an inkjet printhead selectively deposits binder droplets into a powder bed. The binder interacts with the powder particles to form primitives that stitch together to form a cross-sectional layer. Once a layer is printed, the powder feed piston raises, the build piston lowers, and a counter-rotating roller spreads a new layer of powder on top of the previous layer. The subsequent layer is then printed and is stitched to the previous layer by the jetted binder. The remaining loose powder in the bed supports overhanging structures and can be removed with compressed air. To improve green part

strength for handling purpose, the green parts can be heated at an elevated temperature to cure the binder. The printed parts require sintering to obtain final density and strength. During sintering, the binder pyrolizes and particles sinter together through atomic diffusion.

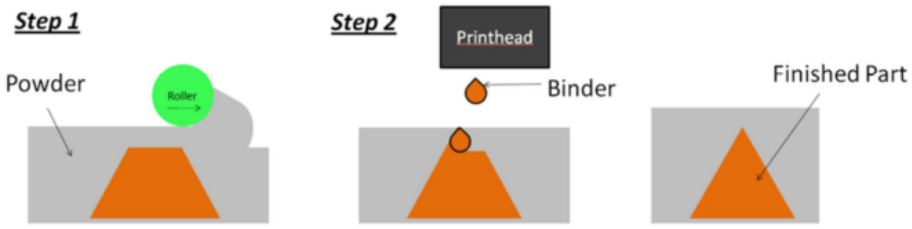

Figure 2.1 Binder Jetting process schematic

While some additive processes exist for copper manufacturing, Binder Jetting has unique characteristics that make it well-suited for fabricating complex copper geometries:

- Its use of a powder bed eliminates the need for support structures typically required when creating for overhanging features. While other direct-metal AM systems employ a powder bed, they require additional structures for part anchoring or heat dissipation purposes.
- As it does not require an enclosed chamber and expensive energy sources, Binder Jetting is an inherently scalable technology. Binder Jetting systems have large build volumes: ExOne offers build volumes of up to 780 x 400 x 400 mm for metal powders; VoxelJet offers a "continuous" sand printer that has a print width and height of 850 x 500 mm and does not restrict the length.
- Binder Jetting is readily adaptable to a wide-range of materials: polymers, ceramic materials, and metals. Material development for direct-metal AM systems is typically complicated by the concerns over a material's melt point, reactivity, optical reflectivity, thermal conductivity, and heterogeneous microstructure.
- As Binder Jetting of metal functionally separates part creation from powder sintering, one can leverage understanding gained from well-studied powder metallurgy (PM) processes.

2.1.3. Context

In this paper, the authors present the results from a preliminary exploration of processing copper via Binder Jetting. Green parts were first fabricated by printing three different atomized copper powders (median diameter ranging from 15 to 75 µm) with an ExOne R2 3D printer. The green parts were then sintered in a tube furnace featuring controlled atmosphere. The experimental work (Section 2.2) focused on binder/powder formulation, powder-binder interaction testing, printing, and post-processing. Densification and mechanical strength were characterized for the resultant copper parts (Section 2.3). Section 2.4 presents a summary along with a discussion on future work to overcome the challenges encountered in this exploration.

2.2. Experimental procedure

Given the authors' goal of processing copper via Binder Jetting, they followed an established methodology for developing new materials for Binder Jetting [12,13]. The methodology includes the selection of binder/powder, the determination of printing parameters in order to fabricate green parts, and the determination of appropriate sintering cycles. In this section, the specific experimental procedure for each stage of the development is presented.

2.2.1. Binder selection

The criteria of binder selection focused on (i) binder interaction with candidate powders (wettability and penetration) and (ii) binder residue after debinding. The authors chose to work with ExOne's standard binder (PM-B-SR2-05), as it is a widely used binding agent for metal powders that has been shown to have minimal ash residue after debinding, and is compatible with the AM machine chosen for this study (ExOne R2).

The functional ingredient of the binder is a thermosetting polymer that hardens upon heating. The printed parts are cured at 190 °C for two hours to fully set the binder and provide satisfactory green part strength. A thermogravimetric analysis (TGA) has demonstrated the binder can completely burn off at 450 °C.

2.2.2. Powder selection

Powders are selected based on their particle size distribution, morphology, and chemical composition. In powder metallurgy, fine powder is preferred in order to lower the required sintering temperature and improve densification. However, in Binder Jetting, particles larger than 20 μm are typically preferred so that the powder can be successfully spread in the recoating step [14]. Small particles can be used, yet they need to be in small volume percentage and generally the size cannot be smaller than 1 μm [15]. A spherical particle shape is preferred over irregular shape for its tendency to flow in recoating and the wettability with binders.

Given these considerations, the authors chose gas atomized copper powders that feature spherical particle shapes. Three differently sized powders were chosen: AcuPowder 153A copper powder (75.2 μm median diameter), AcuPowder 500A ultra-fine atomized copper powder (15.3 μm median diameter), and Ozometal atomized copper powder (16.5 μm median diameter).

The powder particle size distribution was analyzed by laser scattering (Horiba LA-950 Laser Scattering Particle Size Distribution Analyzer). A FEI Quanta 600 FEG Environmental Scanning Electron Microscope (ESEM) using a voltage of 20 kV revealed the particle shape and size. The chemical composition of powder particles was determined by Energy-dispersive X-ray spectroscopy (Bruker EDX) using the same voltage with ESEM.

2.2.3. Green part creation

The compatibility between the powders with the ExOne metal binder was tested by a bench top powder-liquid interaction test before the printing [12]. A pile of powder was strafed with a syringe of the binder liquid. The binder absorption rate and the bonding strength of resulting agglomerates were examined.

The dominant printing parameters in green body creation include layer thickness and binder saturation ratio. For a successful recoating of powders, the layer thickness should be of at least one diameter of the largest particle and preferably three times of the particle size [15]. Saturation ratio (S) describes the percentage of the air space between powder particles (V_{air}) that is occupied by a binder volume (V_{binder}). The saturation ratio is determined from Equations (2.1) and (2.2), and is based on the packing density of the powder bed (PR) and the volume of solid particles in a defined envelope (V_{solid}). The ExOne R2 printing software calculates the required volume of binder to be printed once the binder saturation is input by the user.

$$S = V_{binder}/V_{air} \qquad (2.1)$$

$$V_{air} = (1 - \frac{PR}{100}) \times V_{solid} \qquad (2.2)$$

Saturation ratio needs to be carefully selected as it affects the printing quality and the final sintered density. Sufficient binder saturation is required to obtain green part strength. Conversely, oversaturation of the powder can result in dimensional inaccuracy and low sintered density, caused by bonding unwanted powders and leaving porosity after binder burn-out. For spherical particles, the binder saturation is relatively low because it uses binders efficiently by having small necking area between particles [16].

The layer thickness and binder saturation of each powder was determined experimentally and qualitatively. The binder saturation was estimated first based on the observation from the powder-binder interaction test. The specimens with different combinations of layer thickness and binder saturation were printed iteratively until satisfactory green part quality and strength were observed. A determination of these printing parameters via a systematic design of experiments will be performed in future work.

2.2.4. Post-processing

To determine the suitable sintering cycle for each powder, and to investigate how sintered densities are affected by sintering temperature, time and atmosphere, rectangular testing coupons (24 × 8 × 4 mm) were printed from each powder. The solid state sintering of copper was conducted in a MTI GSL-1600X tube furnace (101 mm tube outer diameter) in either air with a vacuum or in a controlled hydrogen/argon atmosphere.

The primary functions of each heating cycle consist of debinding, reducing and sintering. A 30-minute hold at 450 °C can ensure removal of the printed binder according to TGA. The peak sintering temperature and duration (Figure 2.2) was varied in order to explore their effect on sintered part density. Heating/cooling ramp of 5 °C /min was used for transition between stages.

A proper reduction process for sintering copper powders would fully reduce the oxidation and remove the water vapor before the closure of pores [17,18]. It has been found that an isothermal holding before reaching the relative density of 85%, or a holding temperatures no higher than 900 °C for most copper powders is effective [19]. To study the effects of reducing atmosphere another candidate thermal cycle was studied, which featured an additional hold at 700 °C to facilitate the reduction of copper oxides (Figure 2.2).

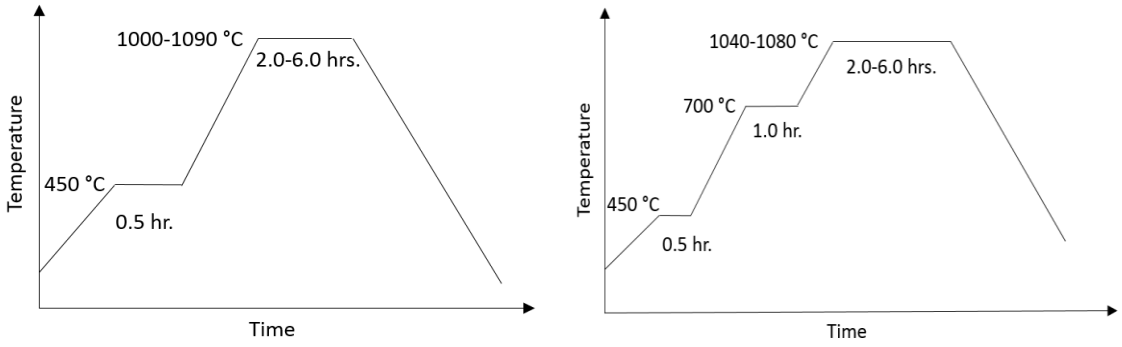

Figure 2.2 The heating schedules used for sintering copper: (left) in air/vacuum and (right) in reducing atmosphere

2.2.5. Part characterization

The density, porosity, shrinkage, microstructure, and tensile strength of the final printed and post-processed parts were characterized.

The sintered density was measured by helium pycnometery (Micromeritics AccuPyc II 1340) and immersion method using Archimedes' principal (Denver Instrument). Helium pycnometry measures the total displaced skeletal volume of the sample [20]. Archimedes' principle measures the volume of water displaced by an immersed object, of which the surface pores were sealed by oil impregnation before measurements [21]. The fractional density was obtained by comparing with the pore-free density of pure copper at room temperature. For open-pore contained objects, Archimedes' principal or gas pycnometry represents the true bulk density only if the open pores are sealed. Therefore, in this paper the Archimedes' principle density of oil impregnated parts is used to represent the bulk density of sintered parts.

To measure packing density of the powder bed, small cups were printed into the powder and later retrieved to measure the mass of packed powder and volume inside the cup. This method only gives an estimate, due to the uncertainty in emptying powders from the cup. The volumetric shrinkage was determined by measuring the dimensions of the sample before and after thermal treatments.

The microstructural features of the sintered copper were explored via SEM, and the weight percentage of copper in the sintered samples was determined by EDX. To observe the pore structure inside the sintered copper, sintered coupons were sectioned and polished for micrographs. The images were taken with a Zeiss AxioImager A2m upright microscope and the porosity was measured by the AxioVision 4 imaging software.

For testing mechanical strength, tensile test specimen was printed with 15 µm powder and sintered in hydrogen/argon [22]. The printed dimension was scaled up by a scaling factor based on the average shrinkage after sintering. The stress-displacement curve was obtained from an Instron (150 kN static rating) testing machine with a displacement rate of 50 mm/min.

2.3 Results and Discussion

2.3.1 Green part creation

Table 2.1 summarizes the powder information and characteristics using the characterization techniques in Section 2.2.2. The particle size distribution and particle shape micrographs of 15 µm and 16 µm powder are shown in Figure 2.3 & 2.4. The 16 µm powder has the highest packing density among three because of the relatively wider particle size distribution. It is hypothesized that the oxidation of copper at room temperature causes the measured purity to be less than the manufacturers' specifications.

Table 2.1 Particle size, packing density, and purity of received copper powders

Designation	*Powder name*	*Median particle size (µm)*	*Packing density*	*Purity of Cu (wt. %)*
75 µm powder	AcuPowder 153A copper powder	75.2	55%	91.0%
16 µm powder	Ozometal atomized copper powder	16.5	63%	95.3%
15 µm powder	AcuPowder 500A ultra-fine atomized copper powder	15.3	56%	96.4%

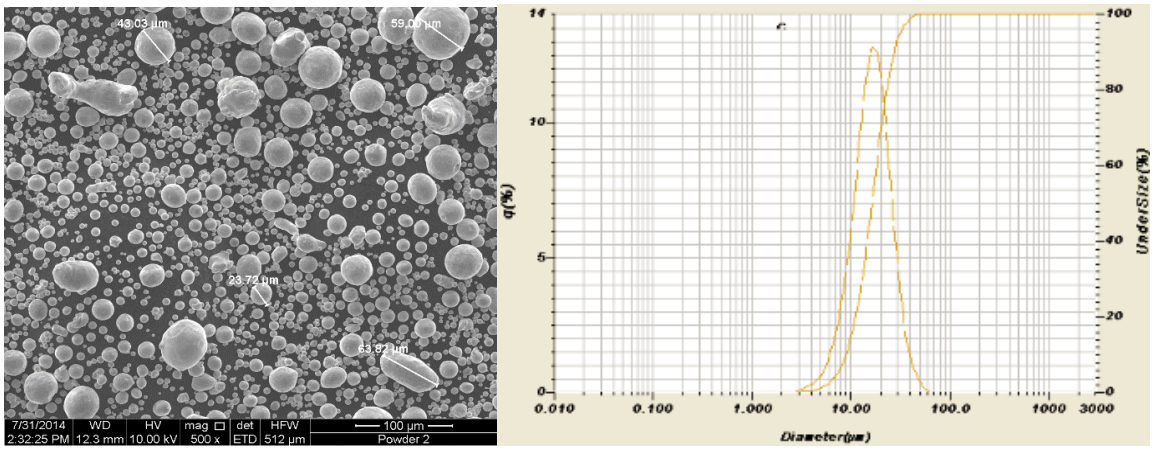

Figure 2.3 16 µm powder SEM (left) and particle size distribution (right)

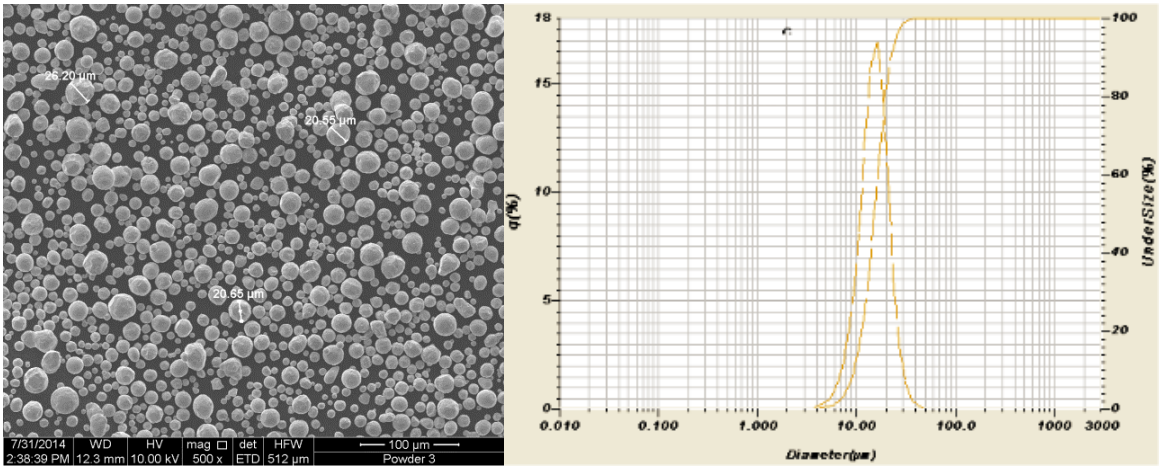

Figure 2.4 15 µm powder SEM (left) and particle size distribution (right)

In a bench-top powder-binder interaction test the binder showed good wetting and penetrating characteristic interacting with all three copper powders. Rectangular bars were successfully printed in each powder on an ExOne R2 3D printer with the settings listed in Table 2.2. The layer thickness was adjusted based on the median/largest particle size, and a binder saturation of 70% was demonstrated to have good shape creation and satisfactory green part strength for all three powders. Two binder saturation ratios, 60% and 80%, were used for printing 15 µm powder to study the effect of binder saturation on sintered density (Figure 2.7, Section 2.3.2).

Table 2.2 Printing parameters for the green part creation

Powder name	*Layer thickness (µm)*	*Binder saturation (%)*
75 µm powder	100	70
16 µm powder	80	70
15 µm powder	80	60 and 80

2.3.2 Densification and shrinkage

To identify the appropriate sintering profile for the printed copper green parts, the authors conducted a preliminary sintering study that leveraged post-processing procedures used in existing copper powder metallurgy research. For pressed and sintered pure copper, a temperature range from 900 °C to 1000 °C held for less than 2 hours can achieve a maximum of 95% sintered density [23,24]. Copper powders with a median size of 10 μm made by injection molding (MIM) was sintered below 1050 °C where a sintered density of 95% was obtained [19].

When similar sintering heating schedules were applied to copper green parts made by Binder Jetting, the final products were insufficiently sintered and densified, especially for the coarse 75 μm powder in Figure 2.5. After sintering in hydrogen at 1000 °C for 8 hours, the volumetric shrinkage was less than 15% and the sintered density was less than 70% of pore-free density. The SEM picture shows the limited degree of necking between copper particles. These observations indicate an initial stage sintering where no significant densification and elimination of the pores has occurred.

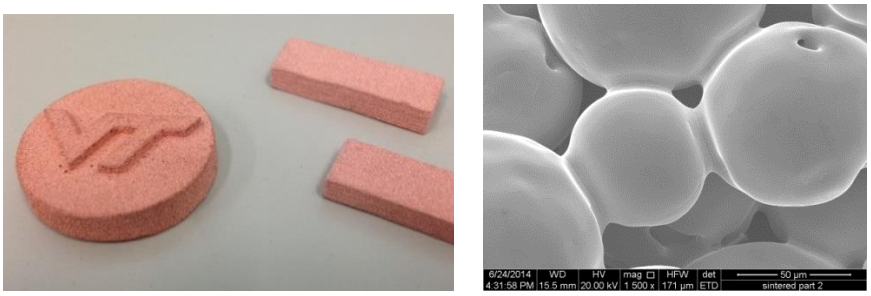

Figure 2.5 75 μm powder sintered in pure hydrogen at 1000 °C for 8 hours. Left: sintered copper samples. Right: SEM of the sintered copper particles

The difficulties in sintering copper prepared by Binder Jetting are not surprising given the large powder particle size and loose packing of the particles. Large space between the loosely packed particles lowers the sinterability in solid state sintering. Similar challenges were found in other powder bed fusion processes [2].

Due to this low sintered density, finer copper powders (15 and 16 μm) were sintered in hydrogen/argon atmosphere with higher temperatures and longer holding time. The sintering temperature (Figure 2.6) and duration (Figure 2.7) were varied to study their effects on the sintered density and shrinkage. Two different binder saturation ratios (60% and 80%) were compared in Figure 2.7.

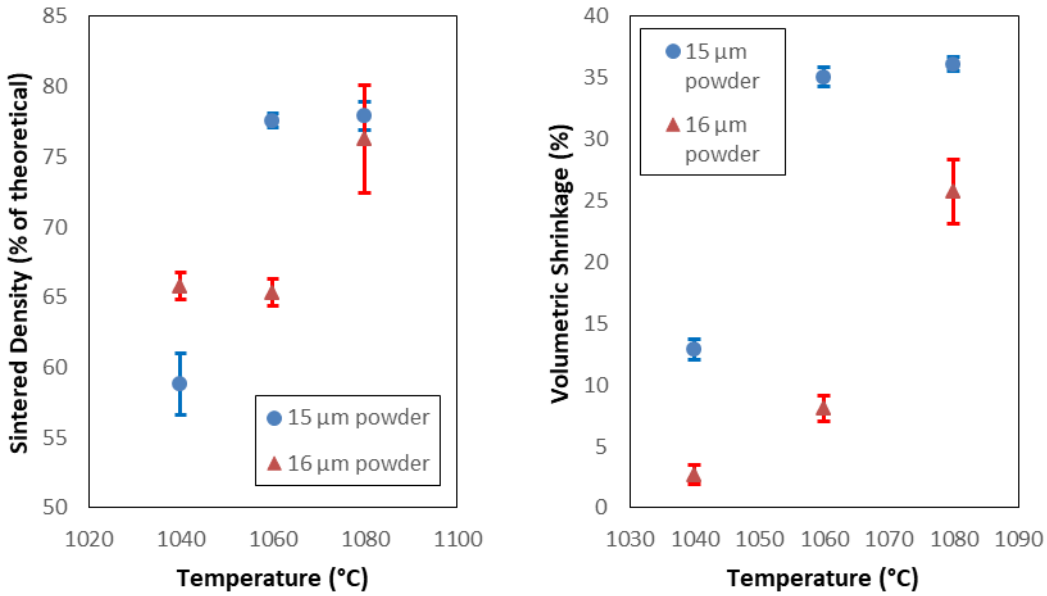

Figure 2.6 Sintered density/shrinkage vs. sintering temperature of 15 µm powder and 16 µm powder (both sintered in hydrogen/argon for 2 hrs.)

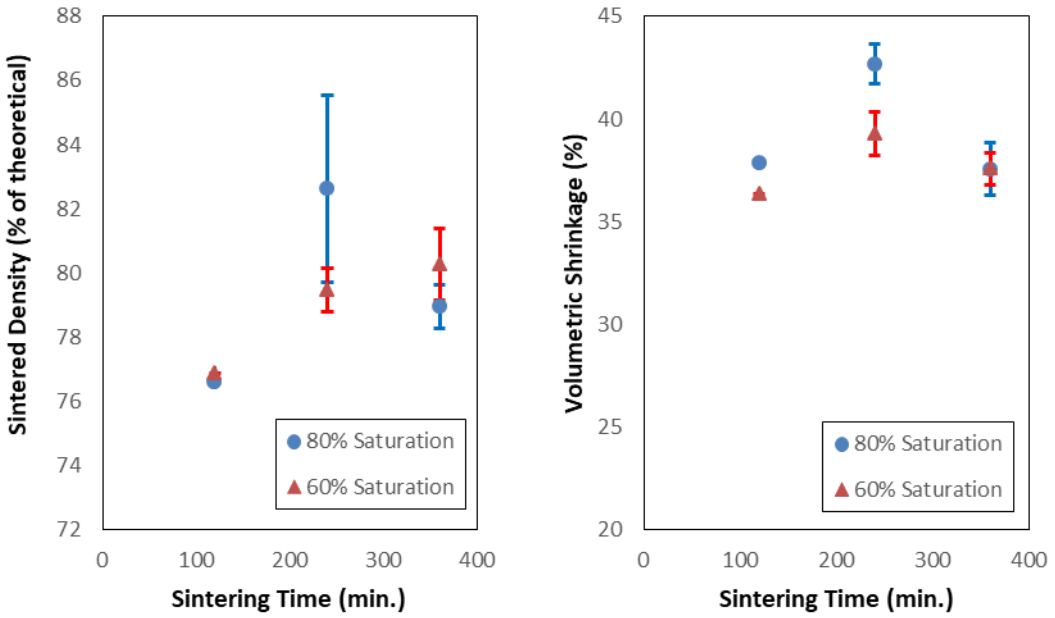

Figure 2.7 Sintered density/shrinkage vs. sintering time of 15 µm powder (60% and 80% binder saturation), both sintered in hydrogen/argon at 1080 °C.

The highest sintered density and volumetric shrinkage of each tested powder is summarized in Table 2.3. It is hypothesized that, because of the impurities in copper powder, the copper samples did not melt or lose shape at high temperatures near the melting point.

Table 2.3 The highest achievable sintered density and volumetric shrinkage

Powder	*Sintered temperature/time*	*Max sintered density (% of theoretical)*	*Max volumetric shrinkage*
75 µm powder	1090 °C/240 min.	63.2%	14.9%
16 µm powder	1080 °C/120 min.	77.6%	22.7%
15 µm powder	1080 °C/240 min.	85.5%	43.4%

As seen in Table 2.3, a finer particle improves the sinterability and the sintered density of copper. Although a wider particle size distribution of powder could potentially increase the packing density and thus better facilitates sintering, the 16 µm powder was not able to sinter to a density as high as the 15 µm powder. This is mostly due to the presence of irregularly shaped large particles (Figure 2.3) and impurities (Table 2.1) that hinders the sinterability.

As seen in Figure 2.6, higher sintering temperatures increased the parts' final sintered density and shrinkage. Generally, longer sintering time has a tendency to improve the densification, while within the range of 2-6 hours there was no strong correlation between sintering time and product properties (Figure 2.7). Similar sintering duration effect was also found in pressed and sintered copper powders [23]. In a comparison between binder saturation and its influence in sintering (Figure 2.7), there was no clear difference observed between 60% and 80%. However, the authors noticed the agglomerating effect of binder droplets in Figure 2.10 (Section 2.3.3), and it was hypothesized that reduced spacing between droplets/agglomerates can increase the sintered density. This can be done by increasing the binder saturation within a reasonable range. Therefore, experimentation with a larger range of binder saturation settings is recommended before drawing a final conclusion.

Using the most suitable powder and processing parameters identified in this section, geometrically complex copper parts were fabricated to show the capability of Binder Jetting (Figure 2.8).

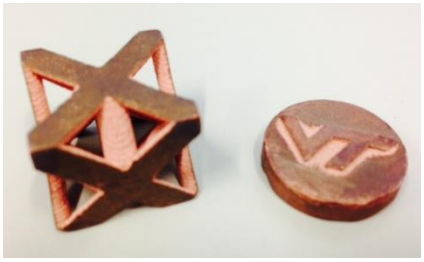

Figure 2.8 Complex shaped copper made via Binder Jetting

2.3.3 Pore structure and distribution

Using oil impregnation and Archimedes' principle (Section 2.2.5), the fractional density as well as the fractional porosity of the sintered parts was determined. Calculated from Table 2.3, one can tell the lowest porosity of all samples is 14.5% (the 15 µm powder product). An alternative approach is using microscopic graph and point counting software to measure the porosity of sectioned/polished surface. Such an analysis was shown Figure 2.9; the percent porosity was determined to be 11.2%, as the ultra-fine pores and surface porosity was not included in this measurement.

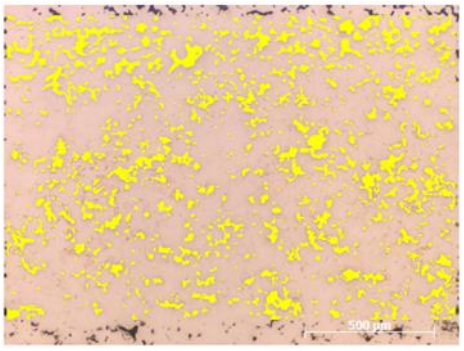

Figure 2.9 Percent porosity measurement using micrographs of the sectioned copper sample (15 µm powder sintered at 1080 °C/240 min.)

Using helium gas pycnometry, it was noticed that non-impregnated sintered parts have a nearly theoretical density of copper. However, when measured by the oil impregnation and immersion method, the sintered parts were 10-20% less dense, which is more realistic. These complimentary results indicate surface-connected and interconnected open pores exist inside sintered copper products.

The same conclusion can be made by examining the microstructure of the surface of sintered copper parts using SEM (Figure 2.10). In Binder Jetting, one droplet of binder combines multiple copper particles together forming a primitive. Each layer is composed of straight lines (Figure 2.10a) and each line is formed by stitching together individual primitives (Figure 2.10b & c). Copper particles in the same primitive sintered to a nearly pore-free state, while the necking between adjacent primitives is very limited due to the large spacing. The insufficient sintering between primitives generates interconnected and surface-connected pore structures.

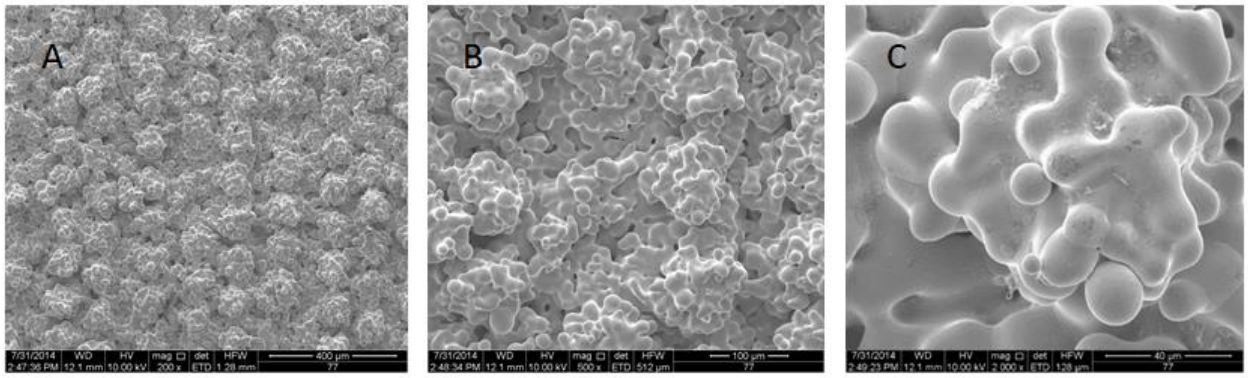

Figure 2.10 SEM of sintered 15 µm powder (1080 °C, 2 hours) at magnifications of (a) 200x, (b) 500x and (c) 2000x

2.3.4 Effect of reducing atmosphere on sintering

A reducing atmosphere not only improves the purity of final products by reducing copper oxides, but also has a positive effect on sintering as it is known the degree of surface oxidation can affect the sintered density of copper powders [19,25]. In the authors' experimentation, the hydrogen sintering atmosphere was able to improve the purity of the final copper product, as shown in Table 2.4. The highest achievable purity of copper across all parts is 97.32%.

Table 2.4 Chemical composition comparison before and after sintering in a reducing atmosphere

	75 µm powder (1000 °C for 4 hrs.)	*16 µm powder (1060 °C for 2 hrs.)*	*15 µm powder (1080 °C for 2 hrs.)*
Copper powder	91.04% Cu	95.32% Cu	96.36% Cu
Sintered parts	94.94% Cu	97.32% Cu	97.11% Cu

To explore the effect of reduction on sintering, the green parts printed from 15 µm powder were sintered in controlled reducing atmosphere (hydrogen) or non-reducing atmosphere (air/vacuum). The reducing atmosphere can improve the sintered density by more than 20% compared to the non-reducing atmosphere (Table 2.5).

Table 2.5 Densification comparison between parts sintered in reducing and non-reducing atmospheres (15 µm powder sintered at 1060 °C for 2 hours)

	Volumetric shrinkage (%)	*Sintered density (% of theoretical)*
Sintering in non-reducing atmosphere (air with vacuum)	5.5	52.9
Sintering in reducing atmosphere (pure hydrogen)	37.1	78.2

2.3.5 Tensile strength

To identify the mechanical strength of the copper parts fabricated for this study, a uniaxial tensile test was performed on printed copper tensile test specimens (Figure 2.11). The specimen was printed from 15 µm powder and was sintered for 2 hours at temperatures of 1080 °C, 1060 °C and 1040 °C.

Figure 2.11 Tensile test specimen sintered at 1060 °C (top) and 1080 °C (bottom)

The ultimate tensile strength of each specimen is shown in Table 2.6. As expected, an increase in sintering temperature (and thus sintered density) dramatically increases the tensile strength. The highest tensile strength of copper achieved by Binder Jetting is 116.7 MPa, while in traditionally made copper powder metallurgy the tensile strength of copper can be as high as 200 MPa [23]. The relatively low strength of the copper specimens fabricated thus far can be attributed to the porosity, as previous studies have shown that the strength of porous sintered copper powder compacts is proportional to their porosity.

Table 2.6 Ultimate tensile strength of specimen (15 μm powder) sintered with various temperatures

Specimen number	*Peak sintering temperature/time*	*Ultimate tensile strength (MPa)*
1	1080 °C, 2 hours	116.7
2	1060 °C, 2 hours	73.3
3	1040 °C, 2 hours	8.4

2.4 Summary and future work

In this work, the author explored the additive manufacture of copper via Binder Jetting. Three atomized copper powders with varied particle diameter and distribution were successfully printed on an ExOne R2 3D metal printer. The copper green parts were sintered in a tube furnace and a maximum of 85.5% density was achieved (Table 2.3). In the temperature range from 1060 °C to 1090°C, the sintered density and shrinkage was increased by higher temperature (Figure 2.6). A controlled sintering atmosphere with the presence of hydrogen was found to be able to increase the purity of the final parts to 97.3% (Table 2.4), and improve the sintered density by up to 25.3% (Table 2.5). The tensile strength of printed sintered copper parts was lower than traditional copper powder metallurgy due to the part's porosity (Table 2.6).

In Binder Jetting, large particle size is preferred for powder spreading while fine powders are critical to the sinterability and have the potential advantages in improving resolution and surface quality. A major challenge facing Binder Jetting of pure metal is to improve part sinterability and densification within the requirement of relatively coarse and loosely packed copper powders. Therefore, future work will focus on the techniques that have the potential to improve copper sinterability while still maintaining suitable powder spreading. Specifically, the authors will investigate multimodal mixture of powders and nanoparticle infiltration. In addition, the authors will explore the effect of printing parameters on sintered part density and characteristics.

2.5 References

[1] Bourell, D. L., Leu, M. C., and Rosen, D. W., 2009, Roadmap for Additive Manufacturing: Identifying the Future of Freeform Processing, the University of Texas at Austin

[2] Badrinarayan, B., and Barlow, J. W., 1992, "Metal Parts from Selective Laser Sintering of Metal-Polymer Powders," Solid Free. Fabr. Symp., (1), pp. 141–146.

[3] Badrinarayan, B., and Barlow, J. W., 1991, "Selective Laser Sintering of a Copper-PMMA System," Solid Free. Fabr. Symp., pp. 245–250.

[4] Frigola, P., Agustsson, R., Boucher, S., Murokh, a., Badakov, H., Fukasawa, a., Musumeci, P., Rosenzweig, J., Travish, G., Faillace, L., La, R., Cormier, D., and Mahale, T., 2009, "Development of Solid Freeform Fabrication (SFF) for the Production of RF Photoinjectors EBM Fabrication Process," Proc. 23rd Part. Accel. Conf., pp. 2015–2017.

[5] Yang, L., Harrysson, O., West II, H., and Cormier, D., 2011, "Design and characterization of orthotropic re-entrant auxetic structures made via EBM using Ti6Al4V and pure copper," Solid Free. Fabr. Symp., pp. 464–474.

[6] Ramirez, D. a., Murr, L. E., Li, S. J., Tian, Y. X., Martinez, E., Martinez, J. L., Machado, B. I., Gaytan, S. M., Medina, F., and Wicker, R. B., 2011, "Open-cellular copper structures fabricated by additive manufacturing using electron beam melting," Mater. Sci. Eng. A, 528(16–17), pp. 5379–5386.

[7] Ramirez, D. a., Murr, L. E., Martinez, E., Hernandez, D. H., Martinez, J. L., Machado, B. I., Medina, F., Frigola, P., and Wicker, R. B., 2011, "Novel precipitate–microstructural architecture developed in the fabrication of solid copper components by additive manufacturing using electron beam melting," Acta Mater., 59(10), pp. 4088–4099.

[8] Murr, L. E. L. E., Gaytan, S. M. S. M., Ramirez, D. A. D. a., Martinez, E., Hernandez, J., Amato, K. N., Shindo, P. W., Medina, F. R., and Wicker, R. B., 2012, "Metal Fabrication by Additive Manufacturing Using Laser and Electron Beam Melting Technologies," J. Mater. Sci. Technol., 28(1), pp. 1–14.

[9] Sriraman, M. R., Babu, S. S., and Short, M., 2010, "Bonding characteristics during very high power ultrasonic additive manufacturing of copper," Scr. Mater., 62(8), pp. 560–563.

[10] Truog, A. G., Sriraman, R. M., and Babu, S. S., 2012, "Surface Modification of Very High Power Ultrasonic Additive Manufacturing (VHP UAM) Aluminum and Copper Structures," Trends in Welding Research, 9th International Conference, pp. 757–762.

[11] Janaki Ram, G. D., Johnson, D. H., and Stucker, B. E., 2007, "Ultrasonic Consolidation with aluminum and copper," 3rd Int. Conf. Adv. Res. Virtual Rapid Prototyp. Virtual Rapid Manuf. Adv. Res. Virtual Rapid Prototyp., pp. 603–610.

[12] Utela, B., Storti, D., Anderson, R., and Ganter, M., 2008, "A review of process development steps for new material systems in three dimensional printing (3DP)," J. Manuf. Process., 10(2), pp. 96–104.

[13] Utela, B. R., Storti, D., Anderson, R. L., and Ganter, M., 2010, "Development Process for Custom Three-Dimensional Printing (3DP) Material Systems," J. Manuf. Sci. Eng., 132(1), p. 11008.

[14] Sachs, E. M., 2000, "Powder dispensing apparatus using vibration", US Patent 6,036,777

[15] Sachs, E. M., Cima, M. J., Caradonna, M. A., Grau, J., Serdy, J. G., Saxton, P. C., Uhland, S. A., and Moon, J., 2003, "Jetting layers of powder and the formation of fine powder beds thereby", U.S. Patent 6,596,224

[16] Cima, M. J., Lauder, A., Khanuja, S., and Sachs, E., 1992, "Microstructural Elements of Components Derived from 3D Printing," Solid Freeform Fabrication Symposium, pp. 220–227.

[17] Lim, T., and Hayashi, K., 1991, "Effects of Addition of Al, Cr and Si on Complete Densification Characteristic in Sintering of Cu Fine Powder," J. Japan Soc. Powder Metall., 38(2), pp. 114–120.

[18] Lim, T., and Hayashi, K., 1993, "Effects of Equilibrium Pressure of Gas Generated by Reduction Reaction in Sintering Densification of MIM Fine Powders," J. Japan Soc. of Powder and Powder Metall., 40(4), pp. 373–378.

[19] Chan, T.-Y., Chuang, M.-S., and Lin, S.-T., 2005, "Injection moulding of oxide reduced copper powders," Powder Metall., 48(2), p. 129.

[20] ASTM Standard B923, 2010, "Standard Test Method for Metal Powder Skeletal Density by Helium or Nitrogen."

[21] ASTM Standard B962, 2008, “Standard Test Methods for Density of Compacted or Sintered Powder Metallurgy (PM) Products Using Archimedes’ Principle.”

[22] ASTM Standard E8/E8M, 2013, “Standard Test Methods for Tension Testing of Metallic Materials.”

[23] Ullrich, W. J., 2003, “Fabrication of copper P/M structural parts,” Int. J. Powder Metall., 39(5), pp. 40–46.

[24] Taubenblat, P. W., and Goller, G., 1970, “The preparation of high-conductivity compacts from copper powder,” J. Inst. Met., 98, pp. 225–227.

[25] Ono, K., Kaneko, Y., and Kankawa, Y., 1994, “Effects of Oxidation on Debinding Process for Sintered Properties of Injection Molded Copper Powders,” J. Japan Soc. of Powder and Powder Metall., 41(3), pp. 227–231.

3. Effect of Particle Size Distribution on Powder Packing and Sintering in Binder Jetting of Copper

3.1. Introduction

3.1.1. Achieving full density in binder jetting of metals

The primary challenge in fabricating metal parts using binder jetting is in achieving a fully dense product following the sintering post-process. Pores typically exist in solid-state sintered ceramics [1–3] or metals [4] fabricated in binder jetting without post-processing. For example, while the authors were able to create complex structures from copper powders in their prior work, the overall mechanical strength is limited by the substantial porosity (15%) in sintered parts [5]. Porosity is challenging to eliminate during sintering because of a low powder bed density and the inability to process ultra-fine powders. Coarse powders are suitable for spreading and packing, but the large particles significantly inhibit sintering densification due to the low sintering driving force. Fine powders are preferred for sintering; however, the powder bed is typically poorly packed and the powder recoating can be difficult due to powder's low flowability and agglomeration. As such, metal parts made by binder jetting are typically infiltrated with a lower melting point material in order to obtain full density [6].

Fabricating highly dense metal parts in binder jetting without infiltration has been a major focus for binder jetting research. Spray-dried granules and slurry-based powders have been used to overcome the difficulty to recoat fine powders [4,7]. A powder compaction mechanism has been developed to increase the powder packing density [8,9]. Liquid phase sintering mechanism or optimized sintering parameters can also increase sintered density [10,2,11]. Pressure assisted sintering has been demonstrated to be able to approach full density in binder jetting of ceramics [12].

3.1.2. Improving sintered density via bimodal powder mixtures

One well-established theory to improve powder packing and increase green density in powder processing techniques is using bimodal powder mixtures. The well-packed powder mixtures, wherein the small particles fill the interstitial voids between large particles, has many benefits such as (i) improved green part property (density and strength) and (ii) less shrinkage after sintering.

However, compared with the certainty and reliable prediction in improving powder packing and green density by bimodal powder, the sintered density improvement is often complicated and uncertain. While small particles have rapid sintering rate and enhanced sintering stress [13], in bimodal powder mixtures the added smaller particles typically bond to the large particles and offer little influence on the overall densification. The addition of coarse powders to a fine powder matrix may increase the packing density, but the difficulty to sinter large particles also hinders densification. German developed a prediction of sintered density of bimodal mixtures and validated with a series of experiments using various materials [14]. In this prediction, the sintered density improvement in a bimodal mixture is influenced by many factors including coarse-fine particle size ratio, powder constituents' packing density and sintering shrinkage, and powder mixing homogeneity. According to the bimodal powder sintering experiments known to the authors, fine powder constituent should be used rather than the bimodal mixture in order to achieve the maximum sintered density.

Particle size distribution and bimodal mixtures have been explored in powder-bed based AM processes. The modeled powder bed formation process using discrete element method shows a dependency on layer thickness in predicting bimodal powder bed's packing density [15]. The experiments with bimodal powder has demonstrated capabilities of increasing layer density by 15% [16]; preventing balling phenomenon and achieving higher radiative heat flux in the powder bed [17]; and influencing final density and mechanical properties [18]. However, the study of sintering bimodal powder mixtures in

the context of binder jetting of metals is limited. Lanzetta et al. studied the improved surface finish and printed primitive morphology in unfired bimodal powders parts [19]. Verlee et al. explored the sintered density of stainless steel bimodal mixtures with experimental and prediction model results similar to the understanding in traditional powder metallurgy [20].

3.1.3. Context

It is hypothesized that in binder jetting the bimodal powder mixture has a greater potential to improve sintered density when compared with the of the use of coarse or ultra-fine powder constituents. Unlike traditional powder shaping methods, the poor flowability of fine powders in binder jetting inhibits achieving satisfactory powder bed packing and green density, which becomes a main obstacle in achieving fully dense parts. Bimodal powder mixture overcomes the poor powder packing of fine powder, and is capable of producing dense green parts that contain high sintering stress small particles, which may finally lead to an improved sintered density.

Additional benefits also exist in using bimodal powder mixture in binder jetting. As most metal parts in Binder Jetting undergo a large degree of shrinkage after sintering (without infiltration), there is a need to increase powder bed packing density to reduce shape distortion for a better product dimensional control. In addition, a powder mixture containing coarse powders typically lowers the powder cost as compared to a powder bed composed of solely fine powders.

The main research goals of this work are to (i) validate the hypothesis that bimodal powder mixtures can improve sintered part density in binder jetting, (ii) develop an understanding in the manufacturing process's influence on the relationship between particle size distribution and final green/sintered part property, and (iii) develop a framework in material property improvement through powder particle size optimization in binder jetting. To achieve these goals, the authors experimentally investigated the use of bimodal powder mixtures in binder jetting of copper.

3.2. Experimental Method

Five powder mixtures (Section 3.2.1) were created to evaluate (i) powder bed density (Section 3.2.2), (ii) green and sintered part density, and (iii) part shrinkage (Section 3.2.5). In addition, experiments were conducted to explore the impact of sintering conditions on powder mixtures (Section 3.2.4). The printing process parameters are detailed in (Section 3.2.3).

3.2.1. Powder selection and characterization

Binder jetting of metals inherently impose upper and lower limits of particle size selection for a successful powder recoating and printing [21], therefore the coarse-fine particle size ratio was limited in a small range in this work (1:3-1:6). The gas atomized copper powders (over 99% purity) used for mixing are listed in Table 3.1 with particle size information. Five bimodal mixtures were created by mixing fine powder with coarse powder with 73-27 (a ratio that is efficient in maximizing powder packing density [22]) or 27-73 weight ratios. Each mixture was mixed for 2 hours in a rotating drum without media to ensure homogeneity. Laser scattering with a Horiba LA-950 was used to analyze particle size distribution (ASTM B822) of the powder mixtures.

Table 3.1 Copper powders used for creating mixtures

Powder name	*D10 (10% particle pass diameter)*	*D50 (median particle diameter)*	*D90 (90% particle pass diameter)*
75 μm powder	58.0 μm	77.0 μm	101.5 μm
30 μm powder	15.0 μm	30.0 μm	37.5 μm
15 μm powder	8.0 μm	17.0 μm	28.0 μm
5 μm powder	0.65 μm	5.5 μm	9.0 μm

3.2.2. Powder packing density assessment

Powder apparent density, tap density and powder bed density were measured for evaluating powder packing efficiencies. Apparent density (lower density threshold of powder bed) was measured using a Hall flow meter (ASTM Standard 212). Tap density (upper threshold of powder bed) was measured using a graduated cylinder with tapping apparatus (ASTM Standard 527). The ratio of apparent and tap density (Hausner ratio) was used to assess powder flowability (lower ratio corresponds to better flowability).

3.2.3. Printing process parameters

An ExOne R2 printer and solvent-based polymeric binder was used for all experiments; 18mm x 6mm x 3 mm test coupons were printed for density evaluations.

The layer thickness should be larger than the largest particle and is recommended to be at least three times of the particle diameter for higher packing density and smoother surface finish [21]. Given the powder size ranges from 5 μm to 75 μm, all samples were printed with 80-100 μm layer thickness (except for 150 μm thick layer for 75 μm powder). The counter-rotating roller spread powder with a constant speed of 5 mm/s to maintain a similar compaction effect across the tested powder mixtures.

Binder saturation ratio describes the amount of binder in the void space between powder particles (a detailed description of binder saturation variable is available in the authors' previous publication [5]). While 100% saturation ratio was used for all parts to obtain satisfactory printing quality, 150% was used for 5 μm powders, as its large total surface area requires extra binder for sufficient bonding. The measured apparent density (Section 3.2.2) was used for each powder to ensure accurate binder saturation.

The powder bed temperature was maintained at 80 °C during printing and an overhead heater (185 °C) was used to dry each printed layer with a scanning speed of 5 mm/s.

3.2.4. Post-processing and sintering

Sintering experiments were conducted in a tube furnace with atmosphere control. All sintering cycles used in this work feature a pure hydrogen atmosphere for copper oxide reduction and an isotherm at 450 °C for 30 min to facilitate debinding. Peak sintering temperature, duration and heating rates were later altered to study the sintered density of bimodal mixtures under different sintering conditions. Three samples were printed and sintered for each sintering condition.

3.2.5. Green and sintered part characterization

The sintered density was measured by an immersion method with Archimedes principle following ASTM Standard 962. Green density, on the other hand, was calculated by the measured printed part weight and dimensions as the immersion method is not applicable to green parts printed with water-soluble binder.

An FEI Quanta 600 FEG Environmental Scanning Electron Microscope (SEM) was used to examine the surface morphology of sintered parts. Sintered parts were also sectioned and polished for optical microscopy imaging to observe pore morphology and porosity.

3.3. Results and Discussion

3.3.1. Bimodal powder mixture's impact on powder packing

3.3.1.1. Particle size distribution

The median particle size and standard deviation of the powder mixtures and their constituents is shown in Table 3.2. With the exception of the 75+15 powder, most powder mixtures exhibit expanded particle size deviation without discrete bimodal distribution, due to the insufficient large-to-small particle size ratio used in this work (3:1 – 6:1).

Table 3.2 Particle size and density of the powder mixtures

Mixture name	*Powder components*	*Median size (D50)*	*Standard deviation*	*Apparent density*	*Tapped density*	*Hausner ratio*
75	75 μm	77.9 μm	23.2 μm	56.1 %	64.9%	1.16
75+15	75 μm (w.t.73%)+15 μm	27.0 μm	39.2 μm	59.7 %	66.9%	1.12
30	30 μm	26.4 μm	10.9 μm	48.5 %	60.8 %	1.25
30+5	30 μm (w.t.73%)+5 μm	17.4 μm	12.4 μm	53.7 %	63.9 %	1.19
15	15 μm	17.0 μm	6.7 μm	52.9 %	65.1%	1.23
15+5	15 μm (w.t.73%)+5 μm	10.8 μm	4.7 μm	54.6 %	67.4 %	1.23
5+30	5 μm (w.t.73%)+30 μm	8.3 μm	15.4 μm	54.4 %	61.2 %	1.13
5+15	5 μm (w.t.73%)+15 μm	5.8 μm	2.7 μm	47.3 %	60.5 %	1.28
5	5 μm	5.5 μm	N/A	41.7 %	55.6 %	1.33

3.3.1.2. Measured powder density and printed part green density

Tables 3.2 shows that the apparent/tap density in bimodal mixtures noticeably surpass the constituent powders. For example, after introducing a small portion of large particles to the 5 μm powder, the apparent density has improved by 12.7% (30 μm) and 5.6% (15 μm), and the tap density has improved by 5.6% (30 μm) and 4.9% (15 μm) respectively. The increase in apparent density is higher than that in tap density, which is particularly useful for binder jetting due to the relatively loosely-packed powder bed.

A similar trend is also seen in the printed green part density (Figure 3.1). For example, after mixing 15 μm or 30 μm particles into the 5 μm powder, the printed green part density improves by 3.0%-9.4%. While the counter-rotating roller typically densifies the powder in powder bed based AM processes, Figure 3.2 shows that green part density is lower than the powder apparent density. This can be explained by (i) the inherent inaccuracy in the green density measurement method (Section 3.2.5) and (ii) green part expansion as binder drains from saturated core to surrounding loose powder and bounds extra powder.

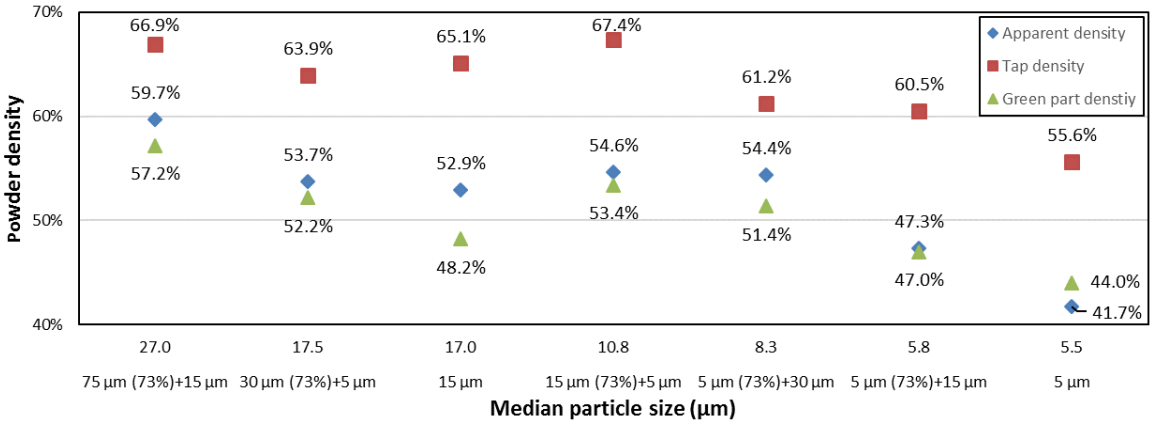

Figure 3.1 Comparison of apparent density, tap density and green density for different powders

3.3.1.3. Powder flowability

The Hausner ratio (tap density over apparent density) shows the powder flowability in bimodal mixtures noticeably improved over the fine constituent powder (Table 3.2). The improved flowability is critical in achieving smooth and dense powder layers in the binder jetting process.

3.3.2. Sintered density and shrinkage of bimodal powder mixtures

With a demonstrated benefit in improving green part density and spreading quality, the bimodal powder mixture's impact on sintered density was then explored. 5 µm powders were mixed with 15 and 30 µm powders at two different mixing ratios (73:27 and 27:73), and then sintered by a sintering profile with a 2-hour hold at 1080 °C peak temperature and 2 °C/min heating/cooling rate (Section 3.2.4).

As seen in Figure 3.2, there exists a trend in improved sintered density for all bimodal mixtures compared to the 5 µm powder, of which the sintered density is stymied by the low green density (44%) due to poor powder flowability.

As compared with the fine constituent powder (5 µm), the bimodal powder is capable of improving sintered density while reducing the shrinkage (Figure 3.2). While a 40-50% volumetric shrinkage (about 15% linear shrinkage) is normal for Binder Jetting of metals and can be compensated by scaling the STL file, the reduced shrinkage achieved by bimodal mixtures can provide additional dimensional control for printing high precision parts.

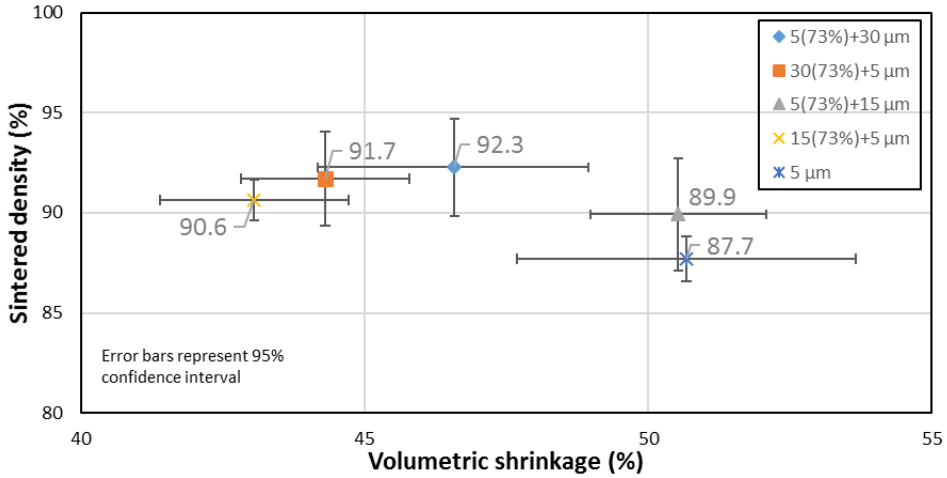

Figure 3.2 Sintered density and volumetric shrinkage of 5 µm powder and its bimodal mixtures, sintered at 1080 °C for 2 hours

3.3.3. Influence of sintering conditions on bimodal powder mixtures

3.3.3.1. Effect of isotherm temperature and duration

In order to explore the impact of sintering conditions on bimodal powder mixtures, the author evaluated three powder mixtures (15+5 μm, 75+15 μm, 30+5 μm), which were sintered under different heating profiles (Figure 3.3), where a peak temperature was held at 1020 °C or 1060 °C for a duration of 30 minutes or 120 minutes.

The sintered density and densification was compared across the powder mixtures in each quadrant of Figure 3.3. The densification in this result corresponds to the density gain from green density to sintered density. While a powder part typically densifies upon sintering, the 75 + 15 μm powder mixture in Figure 3.3(a) has shown a slight reduction in density after sintering, due to the strong sintering inhibition effect of the large particles under insufficient sintering conditions and possible part expansion due to debinding outgassing.

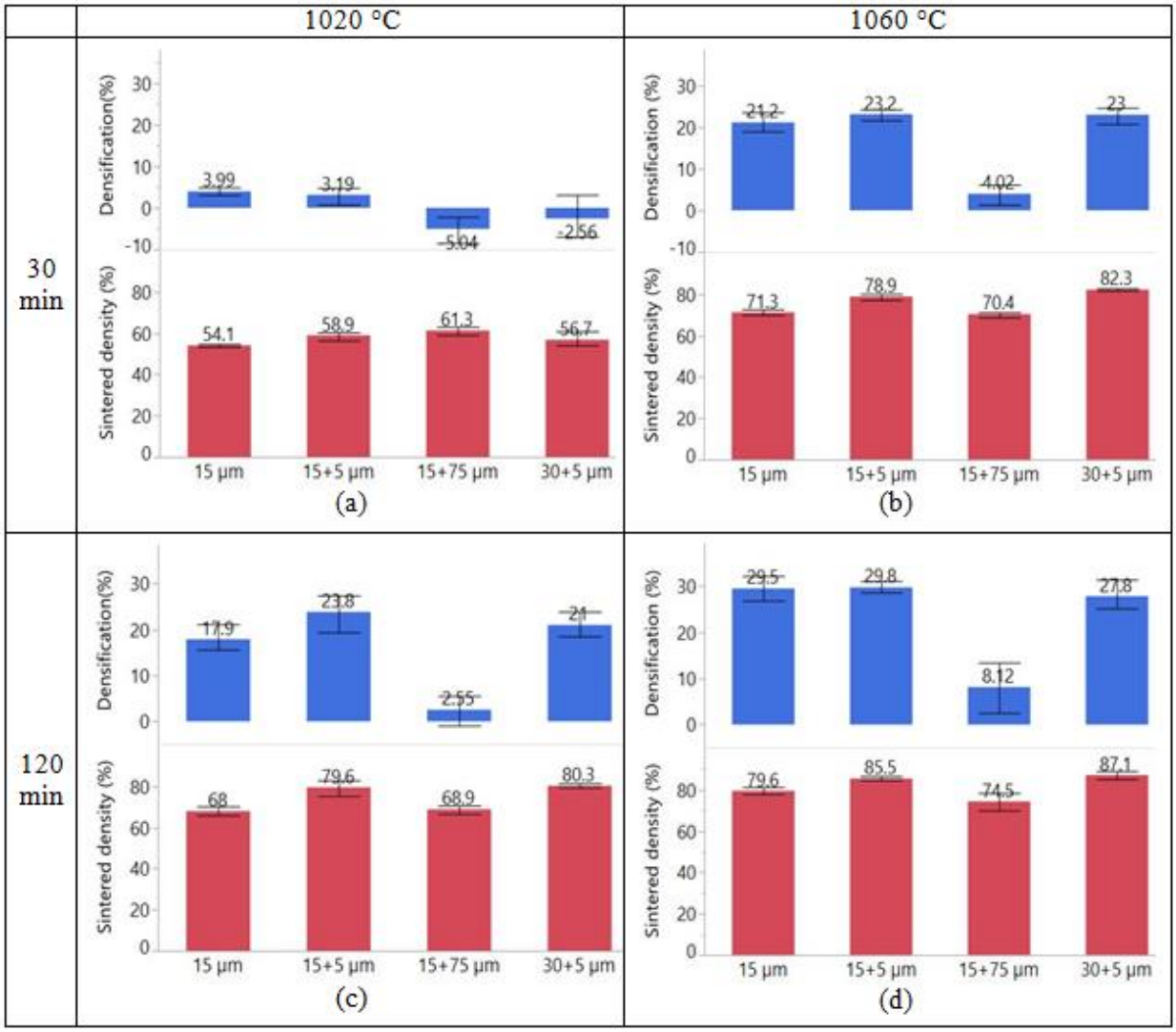

Figure 3.3 Sintered density and densification comparison under various sintering conditions (error bars are constructed with the min and max of the data)

Under the least sufficient sintering condition, the powder bed density dominates in determining sintered density, as the sintering densification is limited. For example, when the powder mixtures that

contain large particles (e.g., 75 µm) are sintered with the insufficient condition (Figure 3a), the initial green density is most influential on final sintered density. However, when treated with additional energy during sintering (Figure 3.3b-d), the high green density in 75 + 15 µm powder parts has failed to generate dense sintered parts as compared to the 15 µm powder.

The powder mixtures without extra coarse powders were able to improve powder bed packing and green density without dramatically shifting median particle size was effective in improving sintered density. Compared with the 15 µm powder (median size of 17.0 µm), the 30+5 µm powder mixture has a similar median particle size (17.4 µm) but a wider distribution, which results in a 4.0% more dense green parts and a 7.5%-11.7% more dense sintered parts depends on the sintering condition (Figure 3.3).

3.3.3.2. Effect of heating ramp

The influence of heating/cooling rate on bimodal powder mixtures was studied by sintering loosely packed powders contained in crucibles at 1080 °C for 120 minutes with different heating rates (Figure 3.4). While heating rate is usually associated with facilitating debinding outgassing in sintering powder compacts, this experiment isolated the debinding effect from sintering and solely studied the heating rate's impact on sintered density. There exists a general trend from the result that monosized powders (5, 15 and 30 µm powder) are more sensitive to heating rates than the powder mixtures. For example, 5 µm and 15 µm powder have seen approximately 10% increase in sintered density by lowering heating rate from 5 °C/min to 3 °C/min, while the sintered density of bimodal powder mixtures does not rely on lowering heating rate to achieve maximum density.

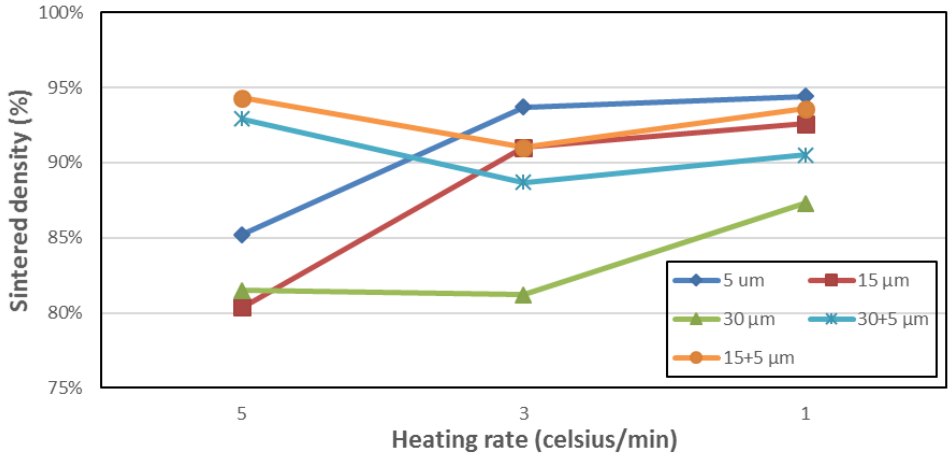

Figure 3.4 Sintered density of loosely packed powders in crucible with different heating rates

Low heating rates provides more energy input into solid state diffusion and provides longer time window that allows particles to rearrange and densify. It is believed that the improved green density provides more contacting areas among particles and creates a network of particles as a diffusion path in bimodal powder mixtures, which makes it less sensitive to total energy input compared with the monosized powders.

3.3.4. Microscopic analysis of sintered bimodal powder parts

Figure 3.5(a) shows the necking has developed between 15 µm and 75 µm particles, however, direct necking and merging between 75 µm particles is limited. The sintered part therefore is composed of a rigid skeleton of 75 µm particles, wherein the high sintering rate of fine powders has little contribution to the overall densification, which corresponds to the limited densification of the 75+15 µm powder in Figure 3.3. 30+5 µm powder, on the other hand, has a better densification result through the merging of

30 µm and 5 µm particles into a coherent body (Figure 3.5b). The powder mixture provided more contact points as available neck formation sites and formed an integrated structure by surface reduction.

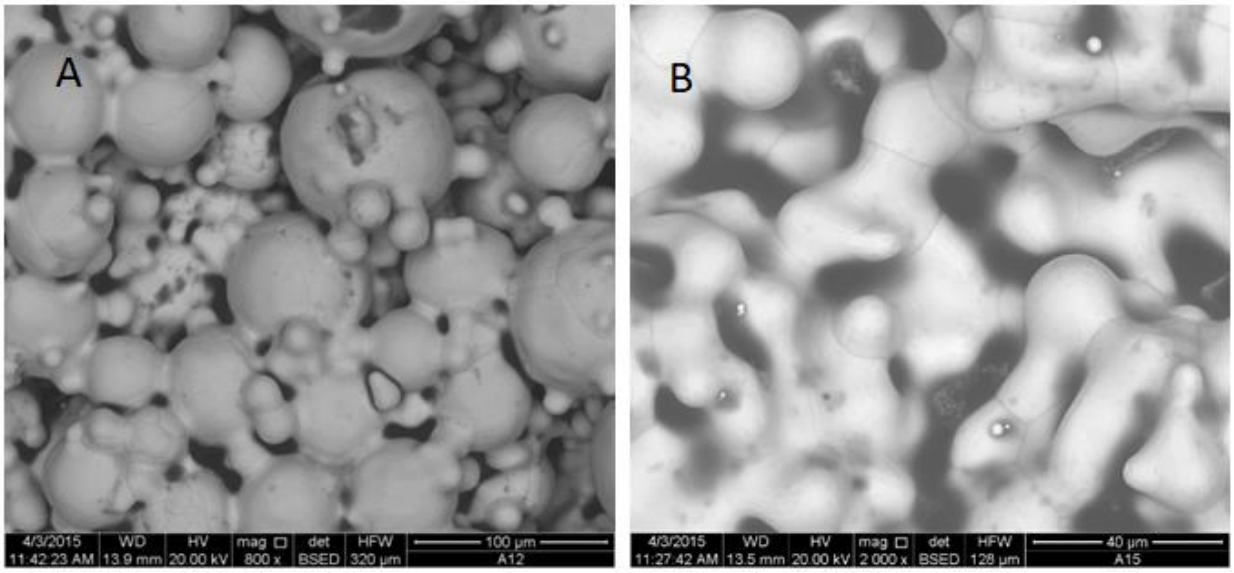

Figure 3.5 Surface microscopic images of bimodal powder parts sintered at 1060 °C for 120 minutes: (a) 75+15 µm powder (800X) and (b) 30+5 µm powder (2000X)

The sintering advantage of bimodal powders is also evident in the optical microscope images of the sectioned and polished sintered parts (Figure 3.6). The 30+5 µm sintered part has fewer pores with smaller sizes and a smoother outer surface compared with the 5 µm sintered sample. The sectioned XY plane (perpendicular to build orientation) shows pores aligned between the lines of printed primitives. As the binder droplet wets and penetrates powder, the surface tension of the binder typically leads to powder balling and rearrangement of powder particles within the primitive, leaving behind more porosity between primitives, especially in a loosely packed powder.

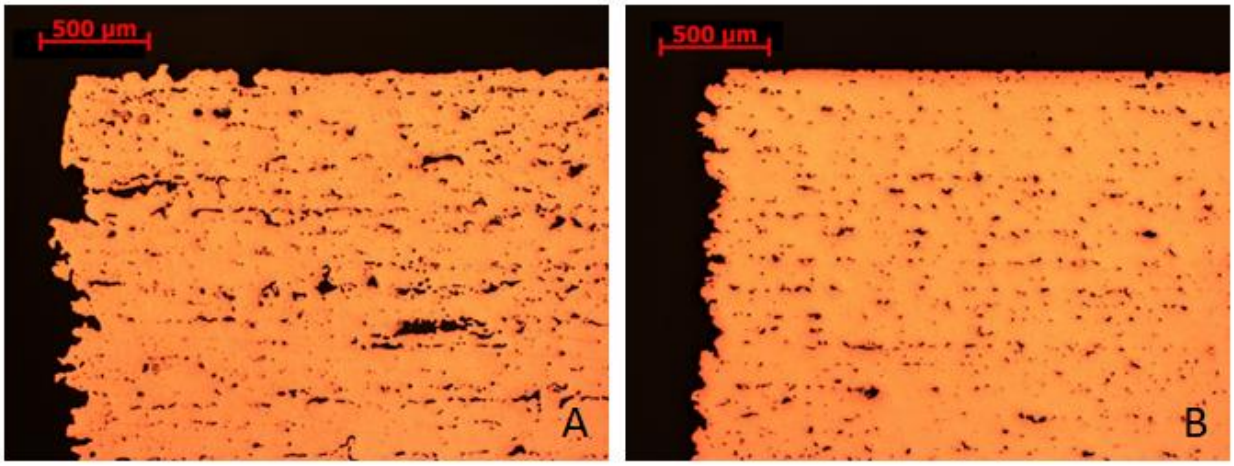

Figure 3.6 Optical microscopy of (a) 5 µm powder and (b) 30(73%) + 5 µm powder, sintered under the conditions in Section 3.3.2

3.3.5. Discussion

In German's specific volume based model, powder packing density and sintered density of bimodal powder mixtures can be predicted by providing packing density and sintering shrinkage information of

the constituent powders [14]. In this model, particle size ratio and powder mixing homogeneity are taken into consideration, and assumptions are made based on sintering theories that small particles do not significantly influence the densification of bimodal compositions rich in large particles.

Figure 3.7 and 3.8 compare the experimental results with the prediction model for two bimodal powder mixtures. Overall, the trend in how packing and sintered density of powder is affected by mixing ratio agrees with the prediction model. Discrepancy exists in sintered density prediction mainly because the constituent powders are not truly monosized particle size ratio is not large enough.

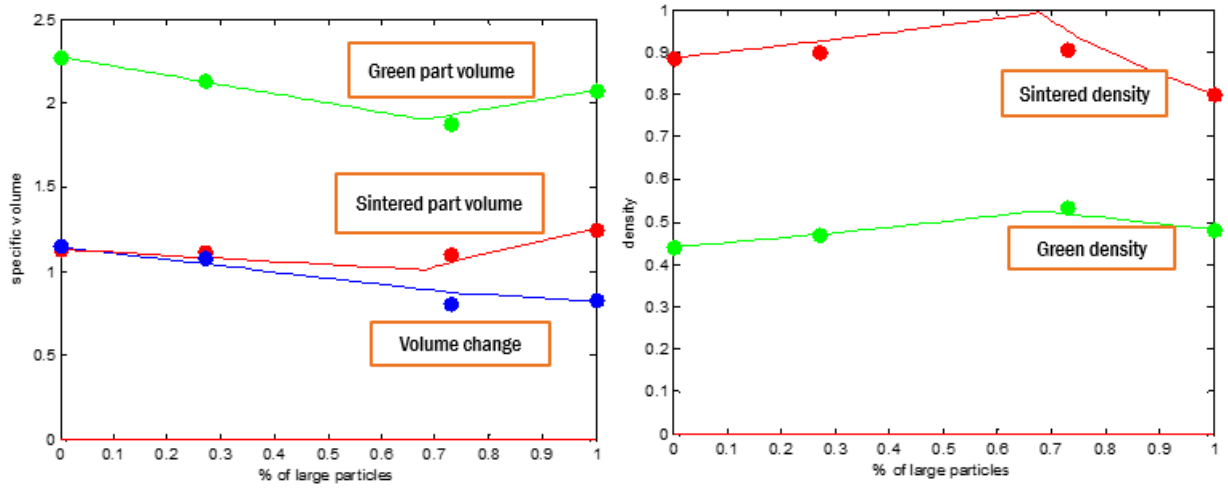

Figure 3.7 Prediction model (line) and experimental results (dot) in specific volume and density of 15+5 μm powder mixture

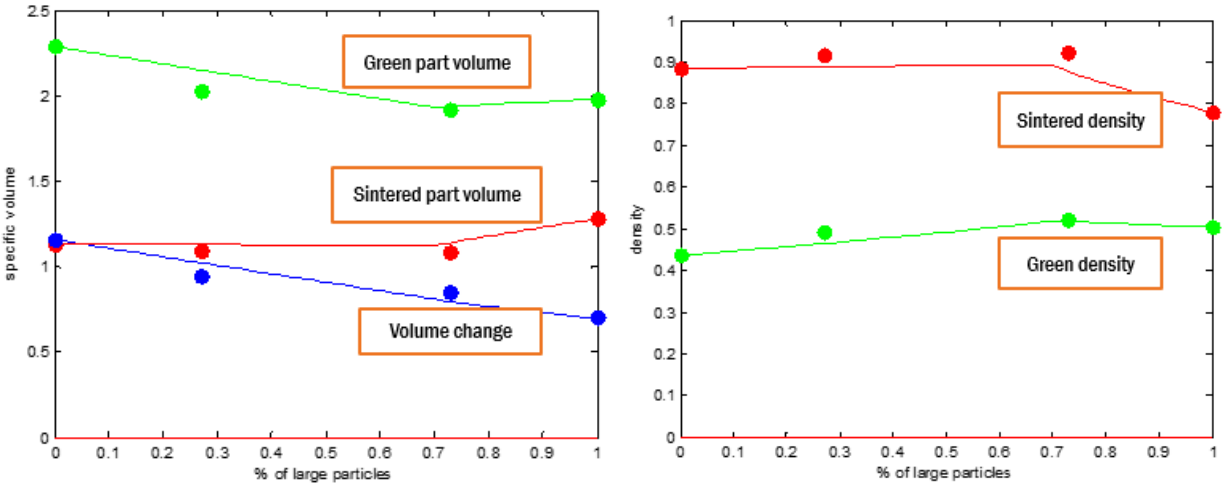

Figure 3.8 Prediction model (line) and experimental results (dot) in specific volume and density of 30+5 μm powder mixture

While prior literature in sintering of compacted powders suggests using the fine powder constituent to achieve maximum sintered density, the results from these sintering trials and prediction model suggest the maximum sintered density can be achieved by using the bimodal powder mixtures. What makes binder jetting unique is the limited sintering shrinkage in sintering ultra-fine powders, where packing density and interparticular contact points is significantly reduced by poor powder flowability.

In general, when a powder mixture contains small particles with large sintering shrinkage, and large particles with small sintering shrinkage, the highest density is achieved by only using the small particles (Region A in Figure 3.9); when a powder mixture is a combination of small particles with small sintering shrinkage and large particles with large sintering shrinkage, the highest density is achieved with bimodal mixture (Region B in Figure 3.9).

In binder jetting, the sintering shrinkage of fine powders is usually constrained by the poor powder flowability and low packing density, which makes the bimodal powder to have a stronger tendency to fall in Region B. In this work, when 5 μm powder is mixed with 15 μm or 30 μm powder, the sintering shrinkage difference between small and large particles is relatively small, and therefore the maximum sintered density is achieved by bimodal mixture. When 15 μm powder is mixed with 75 μm, the sintering shrinkage of coarse powder is significantly reduced, therefore the bimodal powder mixture is not effective at improving sintered density.

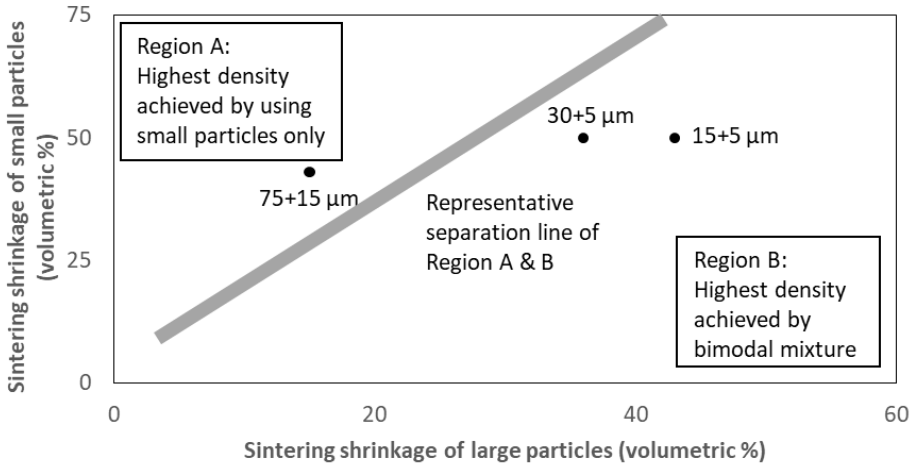

Figure 3.9 An illustration of the relationship between the constituent powder shrinkage and the design of powder mixtures for maximum sintered density (the separation line is only representative in this figure and needs to be determined for each powder mixture based on particle size ratios)

As a result, while it is more likely to achieve the maximum sintered density through bimodal powder mixtures in Binder Jetting than compacted powders, its effectiveness is still affected by many factors, especially the sintering shrinkage of the constituent powders of the material in question.

3.4. Conclusion

Several benefits of using bimodal powder mixture in binder jetting of metals have been demonstrated in this work with copper powders. The bimodal powder mixtures have successfully improved powder packing density and powder flowability. As a result, the printed green part density is able to increase by up to 9.4% as compared to the monosized powder counterparts (Figure 3.1).

The use of bimodal powder mixtures in binder jetting can also improve sintered density. For example, by replacing the monosized 15 μm powder with the 30+5 μm powder mixture, the sintered density improved by 12.3% (Figure 3.3); However, when large particles (75 μm) were mixed into a fine powder (15 μm), the sintered density was not improved due to the rigid skeleton formed by large particles where the sintering contribution of fine powders is constrained (Figure 3.3). The feasibility of improving sintered density by bimodal mixtures over the constituent powders has also been demonstrated by the sintering experiments, however its effectiveness is complicated by many factors, especially the particle size ratio and the relative difference in sintered shrinkage of the constituent powders (Section 3.3.5).

In addition to increased sintered density, the use of bimodal powder mixtures shows additional benefits: (i) the shrinkage is reduced due to increased green density (Figure 3.2); (ii) the bimodal powder mixture is less sensitive to sintering conditions, and potentially can be sintered with less energy input compared to monosized powders (Figure 3.4).

There is an opportunity to explore the effects of bimodal powder on additional materials and powder sizes. This work provides (i) an evidence of improved sintered density by bimodal mixture in binder jetting of copper, (ii) an insight on how powder size distribution affect product property in powder bed based Additive Manufacturing, and (iii) a framework for powder optimization in order to achieve high sintered density in binder jetting of metals.

3.5. References

[1] Gonzalez, J. A., Mireles, J., Lin, Y., and Wicker, R. B., 2016, "Characterization of ceramic components fabricated using binder jetting additive manufacturing technology," Ceram. Int., 42(9), pp. 10559–10564.

[2] Gaytan, S. M., Cadena, M. A., Karim, H., Delfin, D., Lin, Y., Espalin, D., MacDonald, E., and Wicker, R. B., 2015, "Fabrication of barium titanate by binder jetting additive manufacturing technology," Ceram. Int., 41(5), pp. 6610–6619.

[3] Miyanaji, H., Zhang, S., Lassell, A., Zandinejad, A., and Yang, L., 2016, "Process Development of Porcelain Ceramic Material with Binder Jetting Process for Dental Applications," JOM, 68(3), pp. 831–841.

[4] Williams, C. B., Cochran, J. K., and Rosen, D. W., 2011, "Additive manufacturing of metallic cellular materials via three-dimensional printing," Int. J. Adv. Manuf. Technol., 53(1–4), pp. 231–239.

[5] Bai, Y., and Williams, C. B., 2015, "An exploration of binder jetting of copper," Rapid Prototyping Journal, 21(2), pp. 177–185.

[6] Doyle, M., Agarwal, K., Sealy, W., and Schull, K., 2015, "Effect of Layer Thickness and Orientation on Mechanical Behavior of Binder Jet Stainless Steel 420 + Bronze Parts," Procedia Manuf., 1, pp. 251–262.

[7] Holman, R. K., 2001, "Effects of the Polymeric Binder System in Slurry-Based Three Dimensional Printing of Ceramics", Doctoral Dissertation, Massachusetts Institute of Technology.

[8] Gregorski, S. J., 1996, "High green density metal parts by vibrational compaction of dry powder in three dimensional printing process," Thesis, Massachusetts Institute of Technology.

[9] Yoo, J., Cima, M. J., Khanuja, S., and Sachs, E. M., 1993, "Structural ceramic components by 3D printing," Solid Free. Fabr. Symp., pp. 40–50.

[10] Zhang, S., Miyanaji, H., Yang, L., Ali, A., and Dilip, J. J. S., 2014, "An Experimental Study of Ceramic Dental Porcelain Materials Using A 3D Print (3DP) Process," Solid Freeform Fabrication Symposium, pp. 991–1011.

[11] ORANGE, M. J., Kuhn, H. A., KNOR, P. P., and Lizzi, T., 2015, "Process for making nickel-based superalloy articles by three-dimensional printing", Patent No. WO 2015/183796 A1.

[12] Kernan, B. D., Sachs, E. M., Oliveira, M. a., and Cima, M. J., 2007, “Three-dimensional printing of tungsten carbide-10 wt% cobalt using a cobalt oxide precursor,” Int. J. Refract. Met. Hard Mater., 25(1), pp. 82–94.

[13] Coble, R. L., 1973, “Effects of Particle-Size Distribution in Initial-Stage Sintering,” J. American Ceram. Soc., 56(9), pp. 461–466.

[14] German, R. M., 1992, “Prediction of sintered density for bimodal powder mixtures,” Metall. Trans. A, 23(5), pp. 1455–1465.

[15] Xiang, Z., Yin, M., Deng, Z., Mei, X., and Yin, G., 2016, “Simulation of Forming Process of Powder Bed for Additive Manufacturing,” J. Manuf. Sci. Eng., 138(8), p. 81002.

[16] Karapatis, N., and Egger, G., 1999, “Optimization of powder layer density in selective laser sintering,” International Solid Freeform Fabrication Symposium, pp. 255–264.

[17] Zhou, J., Zhang, Y., and Chen, J. K., 2009, “Numerical simulation of laser irradiation to a randomly packed bimodal powder bed,” Int. J. Heat Mass Transf., 52(13–14), pp. 3137–3146.

[18] Spierings, A B., Herres, N., Levy, G., and Buchs, C., 2010, “Influence of the particle size distribution on surface quality and mechanical properties in additive manufactured stainless steel parts,” International Solid Freeform Fabrication Symposium, pp. 397–406.

[19] Lanzetta, M., and Sachs, E., 2003, “Improved surface finish in 3D printing using bimodal powder distribution,” Rapid Prototyp. J., 9, pp. 157–166.

[20] Verlee, B., Dormal, T., and Lecomte-Beckers, J., 2011, “Properties of Sintered Parts Shaped by 3D-Printing from Bimodal 316L Stainless Steel Powder Mixtures,” Euro PM2011, pp. 357–362.

[21] Utela, B., Storti, D., Anderson, R., and Ganter, M., 2008, “A review of process development steps for new material systems in three dimensional printing (3DP),” J. Manuf. Process., 10(2), pp. 96–104.

[22] Zheng, J., Carlson, W. B., and Reed, J. S., 1995, “The packing density of binary powder mixtures,” J. Eur. Ceram. Soc., 15, pp. 479–483.

4. Effect of Inkjetted Nanoparticles on Metal Part Properties in Binder Jetting Additive Manufacturing

4.1. Introduction

4.1.1. Binder selection in binder jetting of metals

The selection of the binder material for binder jetting AM is critical as it determines the success of accurately creating desired geometries and affects the final properties of sintered parts. Different types of binders have been used in binder jetting, including solvents, colloids, and organics [1]. In modern commercial metal binder jetting systems, solvent-based binders that contain thermosetting polymers are commonly used to print metal parts by curing and crosslinking the jetted polymer via in situ thermal treatment.

Polymeric binders with suspended particles have also been used for binder jetting for different contexts and purposes, including tailoring alloy compositions and enabling material gradients [2], enhancing sintering properties [3,4], and reducing sintering shape distortion [5]. While suspended particles can alter printed part properties, crosslinking of the polymer matrix is still responsible for the powder binding mechanism in these embodiments. This prior work has provided proof of concept for changing printed material properties through suspending particles in organic binders, but there is an insufficient understanding of the process-property relationships in the use of these binders.

While polymer binders have demonstrated success with many metal systems, its use in binder jetting adds complexity to the manufacturing process and can adversely affect the final product performance metrics. The debinding of polymer binders typically requires a refined sintering profile to facilitate polymer pyrolysis and degassing, and can compromise printed part structural integrity during sintering, especially when the onset sintering temperature of powders is higher than the binder burn-out temperature. The pyrolysis of polymer binder can also leave residual carbon content, thus compromising purity (and related mechanical, optical, electrical/thermal properties) of the final part. As a result, there exists a benefit of using a colloidal system that is free of organic adhesives as the binder for printing metals.

Yoo *et al.* jetted water-based carbonyl iron (1.7 μm) suspension into a stainless steel powder (60 μm) followed by firing the entire powder bed in forming gas at 600-700 °C, under which temperature the interstitial carbonyl iron particles sintered without sintering the base powder, generating weak but retrievable printed parts [6]. Similarly, Hadjiloucas *et al.* used silver suspensions as the binder for printing molybdenum powders [7]. The printed interstitial silver particles melted and bonded the base powder particles after heating at 1000 °C; at this temperature, the base powder remained loose and ensured part retrieval from the powder bed. Techapiesancharoenkij et al. printed iron and nickel oxide suspensions into Fe-30Ni base powders for printing bimetallic bars [8]. After heat treatment at 400 °C in a reducing atmosphere, the printed bars can be retrieved from unbound powders.

While the concept of colloidal binder has been demonstrated in the literature, the success of printing and material system selection has been contingent upon the large sintering temperature gap between the base powder material and the binder material. As a result, dissimilar material systems composed of refractory powders and low-melting-point-material binders have been used with the requirement of sintering the powder bed in a controlled atmosphere furnace after printing. The feasibility of using a metal binder of the same material as the powder in a single material system has yet been demonstrated.

4.1.2. Roadmap

The goals of this work are to (i) establish an understanding on how jetted nanoparticles affect printed green and sintered part properties, and (ii) explore the use of an inorganic nanosuspension as the binder for printing metals. Two different types of nanoparticle inks are explored in this study (Figure 4.1): (i) colloidal organic binder, made by suspending nanoparticles into an existing off-the-shelf solvent-based organic binder that contains adhesive polymers) and (ii) inorganic nanosuspension, a nanoparticle suspension in non-adhesive dispersion mediums). A traditional organic binder is used for printing control specimens as a point of comparison.

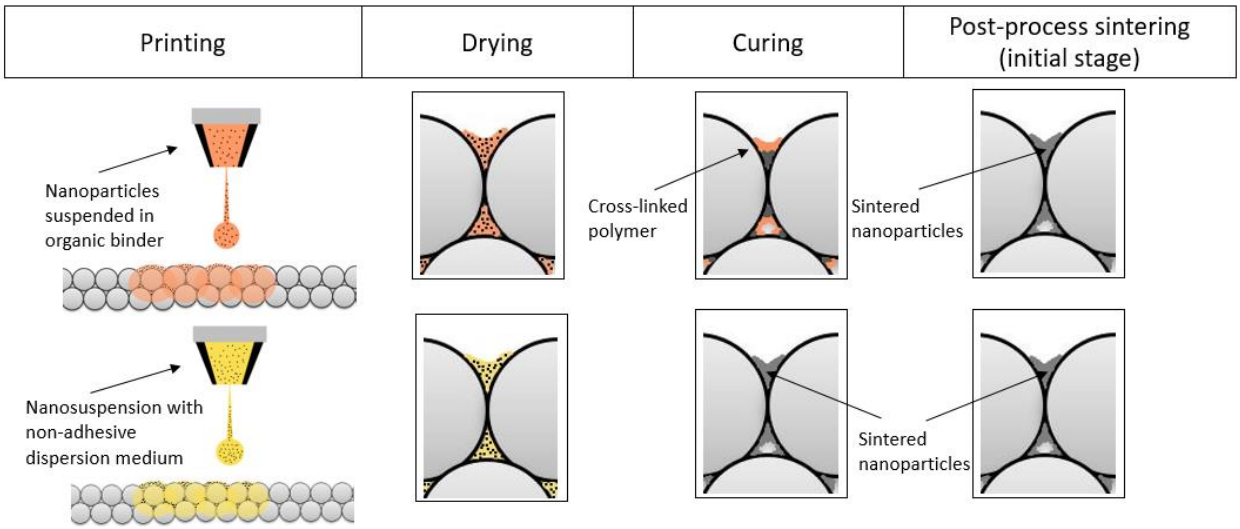

Figure 4.1 Schematics of the use of colloidal organic binder and nanosuspension at different stages of binder jetting

Colloidal organic binder is evaluated first (Section 4.3.1). The sintered part properties (e.g. density, shrinkage, strength) are measured to gain an insight in jetted nanoparticles' impact on sintering densification and microstructure.

To validate the concept of "binderless jetting" (i.e., no organic adhesive), the green part strength produced by printing nanosuspension as the binder needs to be evaluated. Copper nanoparticles are jetted into the powder bed interstices and then fuse the larger copper powders by the heat provided to the powder bed. The low temperature sintering of nanoparticles provides strength to the green part without sintering the large powder particles, thus ensures that the printed green parts can be retrieved from the powder bed.

The binder saturation ratios for printing both binders are varied to gain an understanding on how the printed green and sintered part density is affected by the concentration of the jetted nanoparticles. It is hypothesized that, unlike the use of the organic binder, a higher binder saturation ratio used in printing metal binders can improve sintered density through increased metal content in the printed parts.

4.2. Experimental methods

The description of the two nanoparticle binders is offered in Section 4.2.1. Following an established manufacturing process chain for printing copper [9], the colloidal binders were jetted into copper powders with appropriate drying conditions (Section 4.2.2). Printed green and sintered copper parts were characterized for each material system created under varied binder saturation ratios (Section 4.2.3).

4.2.1. Material systems

A gas atomized copper powder with median particle size of 17 μm (AcuPowder) was chosen as the powder bed material in this work. ExOne's solvent-based organic (polymer) binder was used to print parts as control groups for the experiments.

The colloidal organic binder was prepared by dispersing copper nanoparticles (in the form of a dispersible nanoparticle paste) into the ExOne's solvent-based polymer binder to generate a solid loading of 17.4 wt%. The copper nanoparticle paste used in this study is a commercially available product designed for screen printing and low temperature sintering (Sun Chemical). Satisfactory suspension stability was obtained through sonicating and magnetic stirring (30 minutes) the prepared dispersions.

The inorganic copper nanosuspension is a commercially available conductive ink with a measured solid loading of 23.3 w.t.% and average particle size under 100 nm (Sun Chemical). This product is designed for electronics printing and has a rheology (30 mN/m surface tension and 13 cps viscosity) that is suitable for inkjetting by commercial piezoelectric printheads.

4.2.2. Specimen manufacturing process

Copper green parts were printed with polymer binder and two colloidal binders on an ExOne R2 3D printer, with 100 μm layer thickness. To ensure an accurate binder saturation ratio, the binder drop volume for each binder was measured before and after printing, by sending a waveform pulse to the printhead to fire a known amount of binder droplets to a removable substrate that was then measured for weight differential (Table 4.1). While the drop volume measured for organic based binders is relatively consistent across the printing process, the drop volume measured for copper nanosuspension was inconsistent and varied, potentially due to nozzle clogging. The binder saturation ratio for the nanosuspension was therefore selected by using an average drop volume (70 pL).

Table 4.1 Measured drop volume and adopted binder saturation ratio

	Measured drop volume (before printing)	*Measured drop volume (after printing)*
Organic binder	128.5 pL	132.8 pL
Colloidal organic binder	118.1 pL	119.3 pL
Nanosuspension	64.7 pL	75.0 pL

Finding an appropriate drying condition is critical to ensure the success of printing a new binder, as subsequent layer recoating on top of a wet layer can cause spreading defects. The ExOne 3D printer used in this work features a heated powder box that maintains the powder bed at an elevated temperature, and an overhead heater that scans each layer after printing to dry printed layer with higher temperatures. Guided by results of the thermogravimetric analysis (TGA), which show the solvent removal temperatures (Figure 4.2), the drying conditions in Table 4.2 were determined to remove the jetted solvent and ensure defect-free recoating. An infrared thermometer was used to measure the powder bed temperature during printing, to achieve the desired powder bed temperature by the printer overhead heaters.

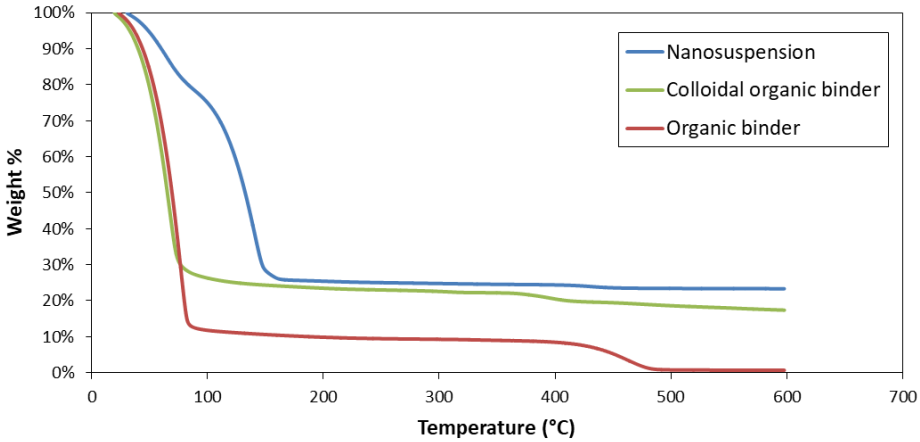

Figure 4.2 TGA of the tested binders

The heat provided for drying nanosuspension binders is also used for the in situ sintering of nanoparticles in the powder bed (Figure 4.1). Theories and microscopic observations have shown that metal nanoparticles manifest size-dependent meting behaviors and lower melting/sintering temperatures compared with the bulk materials [10]. For example, the melting temperature of copper nanoparticles can be reduced to a temperature range of 400-1200 K based on the nanoparticle size, calculated by the Gibbs-Thomson equation [11]. In practice, copper nanoparticles can form necking at reduced temperatures (150-300 °C) [12].

In order to determine the required heating conditions for the nanoparticles to develop necking, the inorganic nanosuspension ink was applied to a silicon wafer substrate and heated at different temperatures (SEM results provided in the appendix). It was observed that heating the powder bed to 260 °C (in both reducing and non-reducing atmospheres) can enable nanoparticle necking while ensuring printed part retrieval (i.e., not sintering the copper powder), and defect-free powder recoating using a prolonged interlayer drying time.

Table 4.2 Drying conditions used for the printing of the tested binders

	Overhead heater set temperature	*Powder bed temperature (during printing)*	*Powder bed temperature (during drying)*	*Heater scanning speed*
Organic binder	200 °C	37 °C	160 °C	5 mm/s
Colloidal organic binder	200 °C	37 °C	160 °C	5 mm/s
Nanosuspension (no organic adhesives)	300 °C	60 °C	260 °C	Pausing for 120 seconds

When an organic binder is used, a post-printing curing of the part at 200 °C is needed to fully cure and crosslink the jetted polymers. While it is possible to integrate post-printing curing into interlayer drying with prolonged drying interval, binder curing is typically conducted separately as a post-process to save printing time. Therefore, the green parts printed with organic binders were cured in an oven at 200 °C for 1 hour after printing. The post-print curing for the nanosuspension binder was not mandatory due to the extensive drying condition adopted for sintering nanoparticles and ensuring printing quality.

The depowdered printed green parts were then sintered in a controlled-atmosphere furnace with hydrogen gas, following a sintering profile featuring 5 °C/min heating to an isotherm held at 1075 °C. A long (600 min.) and short (120 min.) sintering time held at the peak isotherm was varied to explore the effects of nanoparticles on sintering densification and grain growth at different sintering conditions. An additional isotherm at 450 °C was incorporated into the heating schedule for the organic binder printed parts to debind jetted polymers. While there was no need to debind the nanosuspension printed part, a similar isotherm was used in the sintering cycle to eliminate the impact of different heating isotherms on sintering.

4.2.3. Printed part characterization

A series of 18mm × 6mm × 3mm test coupons were printed for evaluating the density of parts printed by each binder, with a sample size of 3 for each material and printing condition (binder saturation ratio and sintering temperature/time). Green part density was calculated from the measured part mass and dimensions. Sintered density was measured by immersion method with oil impregnation (ASTM Standard 962).

While green part strength is not directly linked to final sintered part performance, it is an important factor to qualify a newly developed material system in binder jetting, in order to determine whether a binding agent is capable of producing green parts with satisfactory strength and integrity to withstand depowdering. As a result, the strength of parts printed by nanosuspension was evaluated by its flexural strength, and compared with the organic binder printed counterparts. Using ASTM B312 standard as a reference, the flexural strength was evaluated by identifying the peak load at specimen rupture in a 3-point bending test (MTS platform, 1kN load cell), using a constant displacement rate of 0.1 mm/s.

The mechanical strength of printed and sintered copper was evaluated by tensile test. Two tensile specimens were fabricated (based on ASTM Standard E8) for each test. A tensiometer was used to ensure a strain rate of 0.05/min for displacement, which is suitable for determining ultimate tensile strength of metallic materials.

A LEO (Zeiss) 1550 field-emission SEM was used for micrographic imaging of printed parts. Metallographic analysis using an optical microscope was performed on sintered parts after polishing and etching with ammonium hydroxide and hydrogen peroxide water solutions. Energy-dispersive X-ray spectroscopy (EDS) with 20 kV electron voltage was used for chemical composition analysis of sintered parts. Knowing that EDS is limited in its surface characterization nature, an Optical Emission Spectroscopy (BRUKER Q4 TASMAN) was used to perform metal analysis of the final bulk material properties.

4.3. Results

4.3.1. Jetting colloidal organic binder

4.3.1.1. Green and sintered part density

Figure 4.3 compares the green part density between pure organic binder and colloidal organic binder with suspended nanoparticles. When higher binder saturation ratio was used, it was noticeable that the green parts printed by colloidal organic binder produced higher density, due to the additional metal content added through the deposition of extra amount of binder.

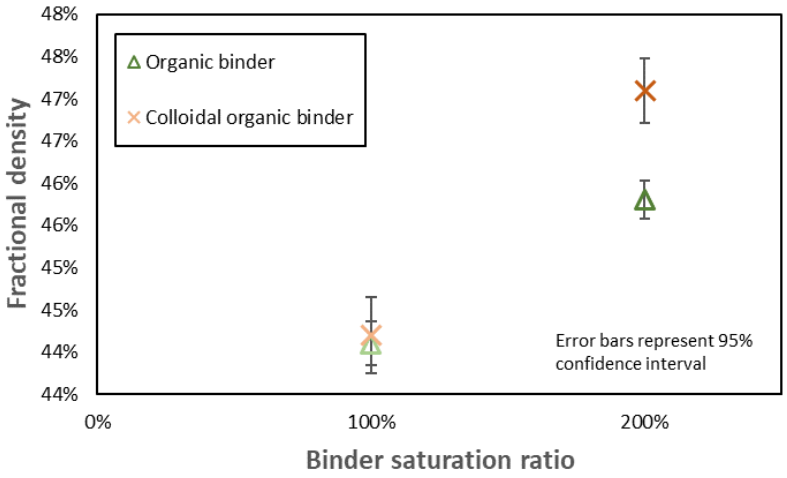

Figure 4.3 Green density of polymer binder and nanoparticle-polymer suspension printed parts

The sintered density is plotted against sintering shrinkage, for the parts sintered with a short isotherm (Figure 4.4) and long isotherm (Figure 4.5). Both sintering densification and sintered density have been improved after sintering at peak temperature for 10 hours.

When the organic binder was used, the sintering densification was hindered by a high binder saturation ratio, as the extra amount of organic contents inhibited new contact formation between particles and produced more binder pyrolysis byproducts that constrained pore shrinkage. The sintering shrinkage was further reduced when nanoparticles were jetted along with the organic binder, which hindered powder particle rearrangement during sintering.

The sintered density comparison between different binder types and binder saturation ratios was statistically insignificant (indicated by Student's T-test). While it has been demonstrated in prior work that high green density can lead to improved sintered density in binder jetting of copper [13], this work has shown that the green part densified through jetting nanoparticles may not lead to a higher sintered density, as the green density increase was countered by the sintering densification reduction.

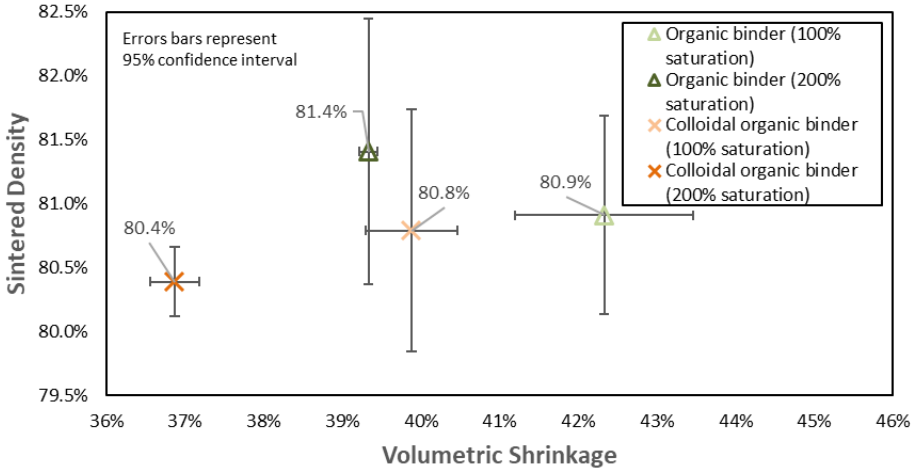

Figure 4.4 Sintered density vs. sintering shrinkage of organic binder and nanoparticle-polymer suspension printed parts (sintered at 1075 °C for 120 min.)

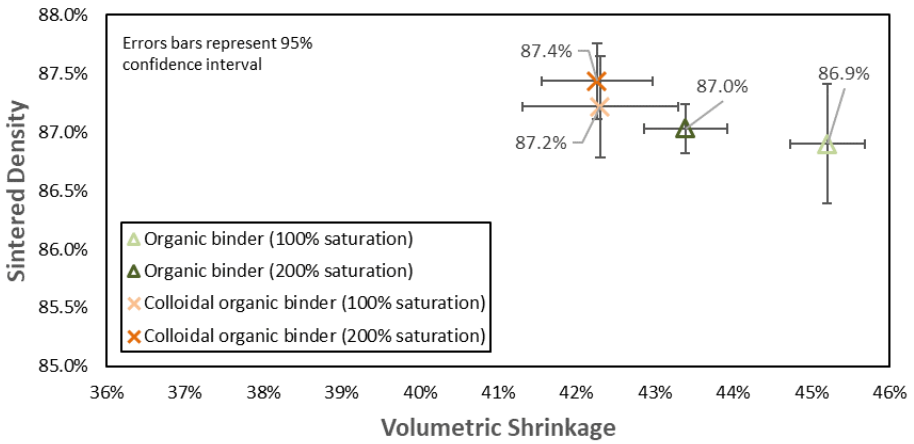

Figure 4.5 Sintered density vs. sintering shrinkage of organic binder and nanoparticle-polymer suspension printed parts (sintered at 1075 °C for 600 min.)

4.3.1.2. Microstructure-property relationship

Figure 4.6 and Figure 4.7 show the microstructure of sintered parts and allows comparison of the grain structure between pure organic binder and colloidal organic binder. As the grains experienced significant growth under the prolonged heat treatment (e.g., sintering at peak temperature for 600 minutes), the jetted nanoparticles have reduced the grain size. Compared to the organic binder printed parts, the use of a nanoparticle binder reduced the average grain diameter from 40.0 µm to 31.8 µm, and average grain area from 0.0016 mm^2 to 0.0010 mm^2. The nanoparticle's effect on grain size reduction in the sintering of a powder with doped nanoparticles is hypothetically caused by a lowered grain boundary mobility, due to the pinning effects [14] and/or Ostwald ripening in sintering nanoparticles [15].

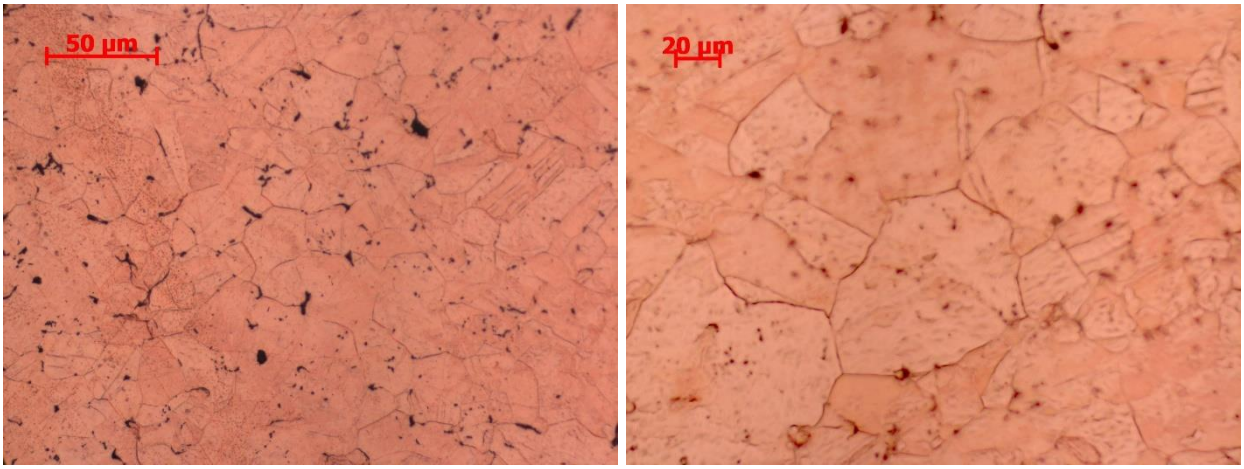

Figure 4.6 Metallographic analysis (100x) of polymer binder printed parts (200% binder saturation), sintered at 1075 °C for 120 min. (left) and 600 min. (right)

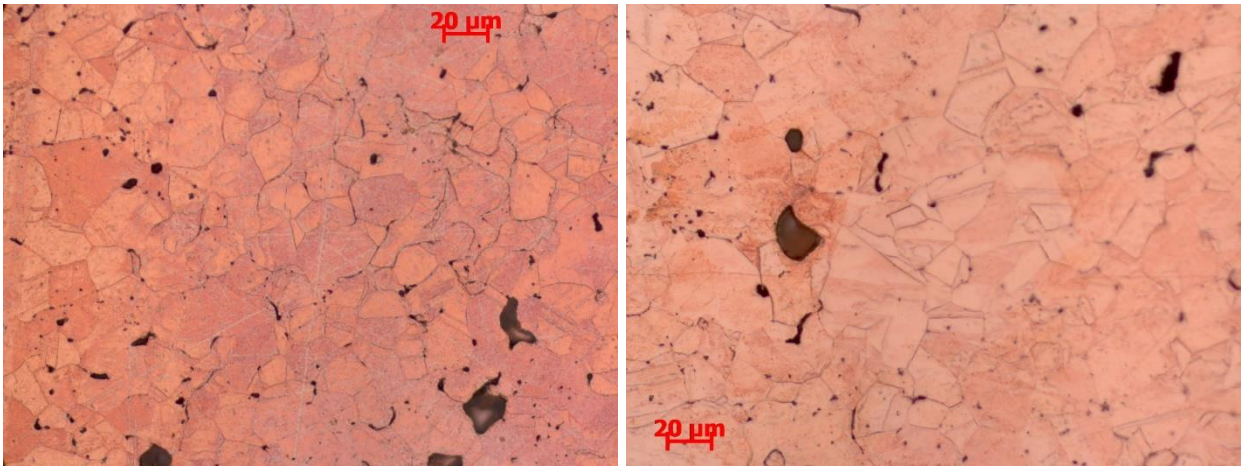

Figure 4.7 Metallographic analysis (100x) of nanoparticle in polymer binder printed parts (200% binder saturation), sintered at 1075 °C for 120 min. (left) and 600 min. (right)

The colloidal binder's reduction on grain size was also reflected in the ultimate tensile strength of sintered parts (Figure 4.8). In porous metal parts, the mechanical strength is mainly determined by the porosity, but can be also further reduced by a large grain size. As a result, despite having similar sintered density as compared to the organic binder (Figure 4.5), a higher tensile strength was obtained in colloidal binder printed parts when the binder saturation ratio was sufficiently high. For the same reason, due to the nanoparticle's inhibition effect on grain growth, a higher binder saturation ratio of colloidal binder has a tendency to produce stronger sintered parts, which was opposite than the use of pure organic binder.

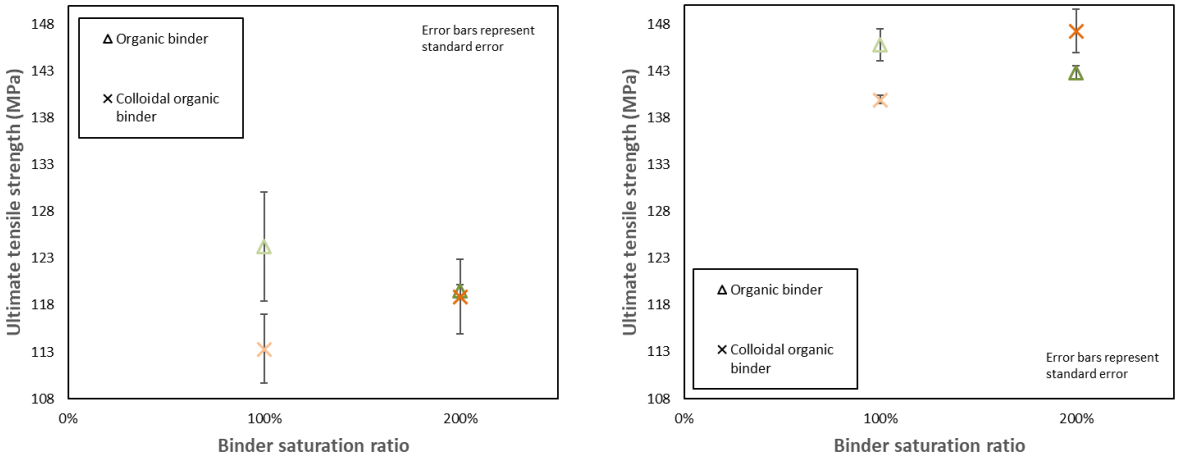

Figure 4.8 Ultimate tensile strength comparison between parts sintered at 1075 °C for 120 min. (left) and 600 min. (right)

4.3.2. Jetting inorganic nanosuspension as the binder

4.3.2.1. Nanoparticle bonding

Using the binder drying and sintering conditions specified in Table 4.2, green parts were successfully printed by jetting inorganic nanosuspension as the binder. Compared to the use of organic binder, in which powders were held by a cross-linked polymer, the binding mechanism in nanosuspension printed parts was completely different, as the powders were linked by the sintered metal bonds made of the same material (Figure 4.9).

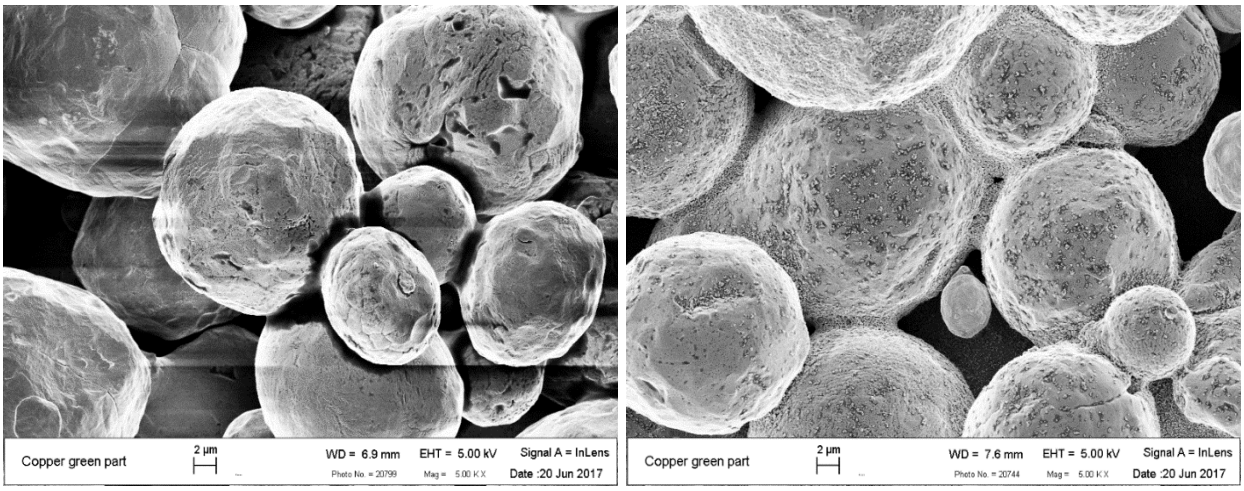

Figure 4.9 Electron micrographs of the surface of green parts printed by polymer binder (left) and nanoparticle suspension (right) following the curing condition in Table 4.2

A further magnified imaging of the necking region in the green parts printed by nanosuspension binder reveals a network of sintered copper nanoparticles that provided the interparticle bonding to the copper powders (Figure 4.10). The microscopic images also reveal the distribution of nanoparticles within printed parts. As the jetted binder penetrated into powders driven by capillary pressure, the channels formed between powder particle contact points acted as capillary tubes, which have a higher capillary pressure than the powder voids as a result of the smaller capillary radius. Therefore, while some nanoparticles were distributed across the copper powder surface, the vast majority of jetted nanoparticles have concentrated to the necking regions between powders.

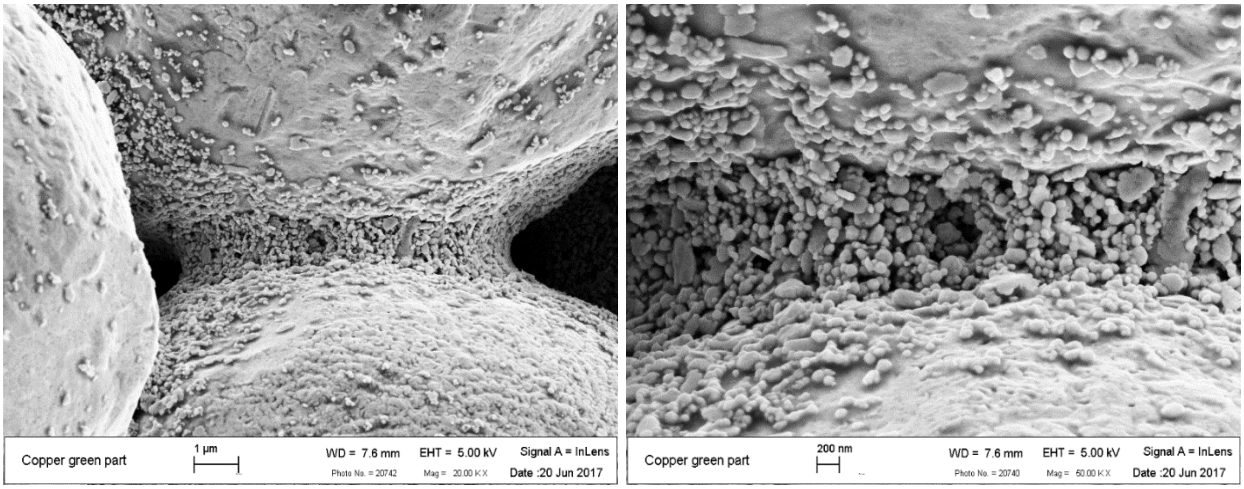

Figure 4.10 Electron micrographs at 20kx (left) and 50kx (right) of the nanoparticle bonding formed after curing at 260 °C

4.3.2.2. Green part properties

Figure 4.11 compares the green strength of organic binder printed parts and copper nanosuspension printed parts with different binder saturation ratios and curing temperature. Initial green part strength was gained through the in-situ nanoparticle sintering during printing, using a high powder bed temperature (260 °C). Additional post-print curing has allowed further nanoparticle sintering, which further improved the green part strength.

Compared to the commonly used organic binder as a reference, the nanoparticle suspension can produce equally or superiorly strong green parts. Using a higher binder saturation ratio has significantly strengthened the nanoparticle bonding through more contact points formed between nanoparticles.

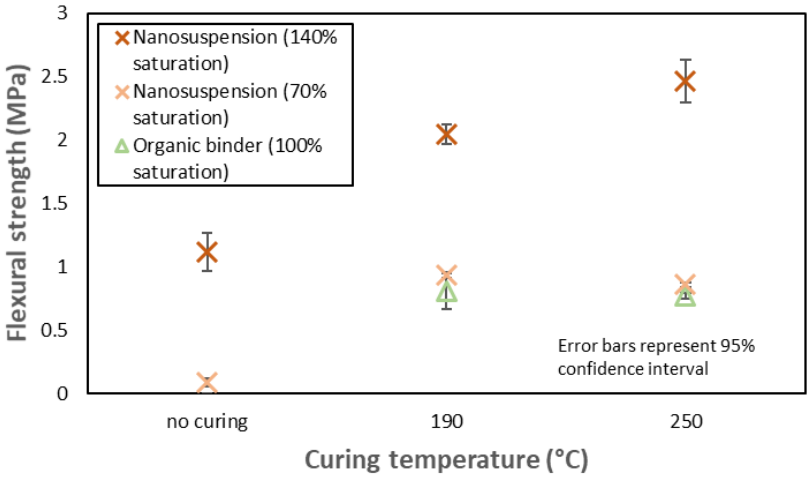

Figure 4.11 Flexural strength of printed green parts after curing at different temperatures

Similar to the results in the use of colloidal organic binder (Figure 4.3), a higher green part density was achieved through depositing extra nanoparticles via using a higher binder saturation ratio to the powder particle necking regions (Figure 4.12).

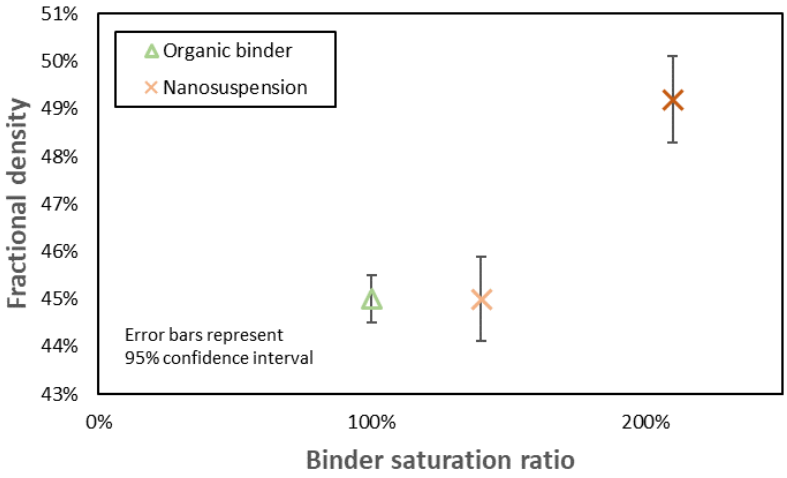

Figure 4.12 Green density of polymer binder and nanoparticle suspension printed parts

4.3.2.3. Sintered part properties

The use of nanosuspension without organic adhesives as a binder hypothetically allows the use of higher binder saturation ratios, as the need to debind organic binders is eliminated. However, the increased binder saturation ratio achieved through overlapping binder droplets has created part distortion caused by shifting unanchored layers during powder recoating (Figure 4.13). When binder droplets are overlapped on the same powder layer to create a high binder saturation ratio, the powder imbibition of newly jetted binder is constrained by the shrinking capillary pores that are filled by previously jetted nanoparticles. As jetted nanoparticles accumulate on powder surface due to slowed or refused entry into powder, it can cause uneven printed layer surface that leads to recoating issues.

Figure 4.13 Sintered copper parts printed by the nanosuspension with different binder saturation ratios

The jetted nanoparticles' impact on sintering densification is shown in Figure 4.14, with the sintered density plotted against the shrinkage . Similar to the findings in printing the colloidal organic binder (Figure 4.4 and 4.5), the sintering shrinkage was reduced by the jetted nanoparticles that constrained the powder particle rearrangement during sintering densification. Without the need to debind an organic adhesive content, the sintered density can be improved by printing the inorganic nanosuspendion with a higher binder saturation ratio (Figure 4.15), as the metal contents deposited into the printed parts was increased.

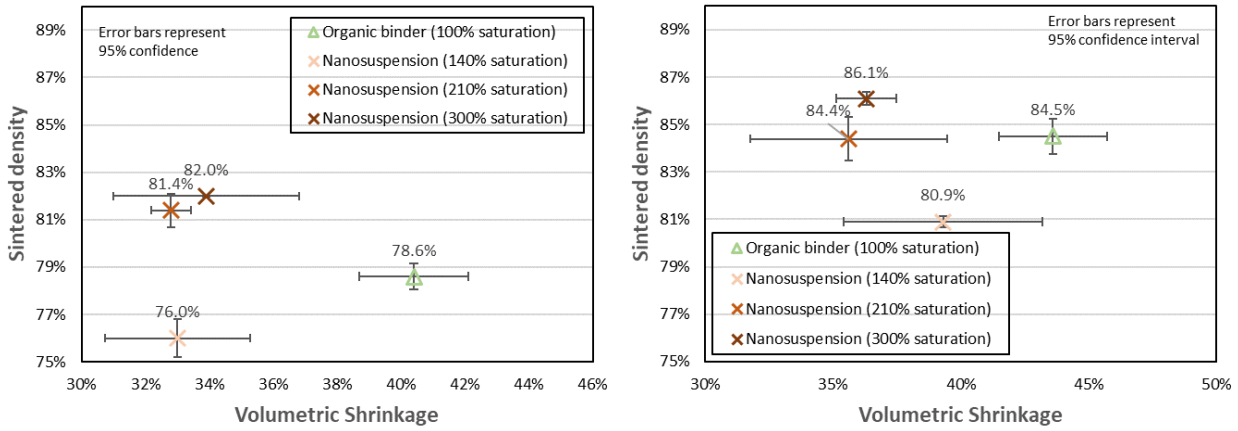

Figure 4.14 Sintered density vs. sintering shrinkage after sintering at 1075 °C for 120 min. (left) and 600 min. (right)

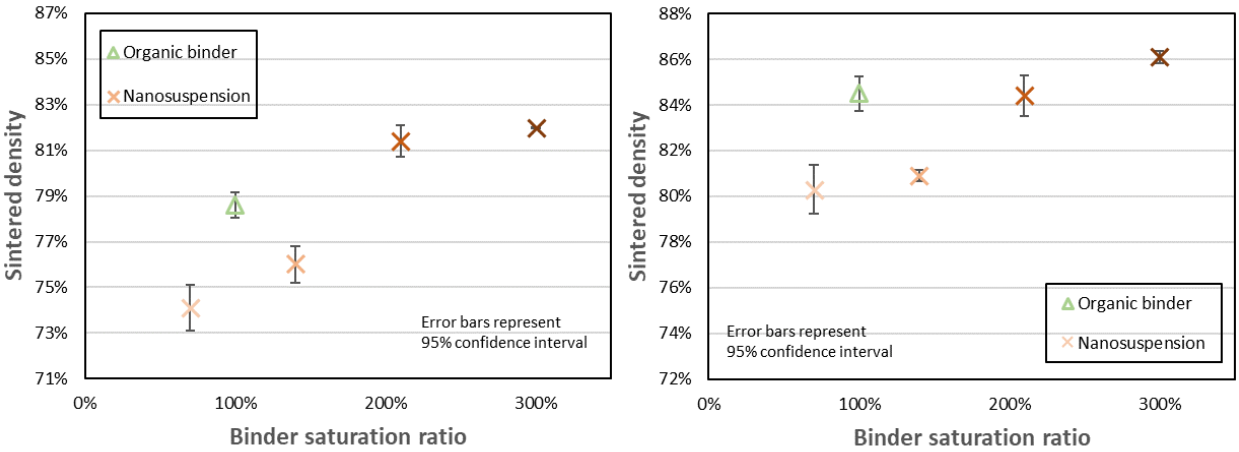

Figure 4.15 Sintered density vs. binder saturation ratio after sintering at 1075 °C for 120 min. (left) and 600 min. (right)

The relationship between the binder saturation ratio and the sintered part density can be understood by converting the binder saturation ratio to the weight percentage of powder particles (% of large particles) in the nanosuspension binder printed parts (Figure 4.16). As shown in Equation 4.1, the weight percentage of powder particles can be calculated by the powder packing density (φ), binder saturation ratio (S), and binder nanoparticle solid loading ($\emptyset$). As nanoparticles were deposited into the powder necking regions, the sintered density reduced first due to the reduced sintering shrinkage, and then increased as the reduced densification was compensated by the weight gain from increasing the content of nanoparticles. A similar trend has been reported in the literature of sintering a mixture of micron and nano-sized alumina powders [16].

$$\%\ of\ large\ particles = \frac{\varphi}{(1-\varphi)S\emptyset+\varphi} \qquad (4.1)$$

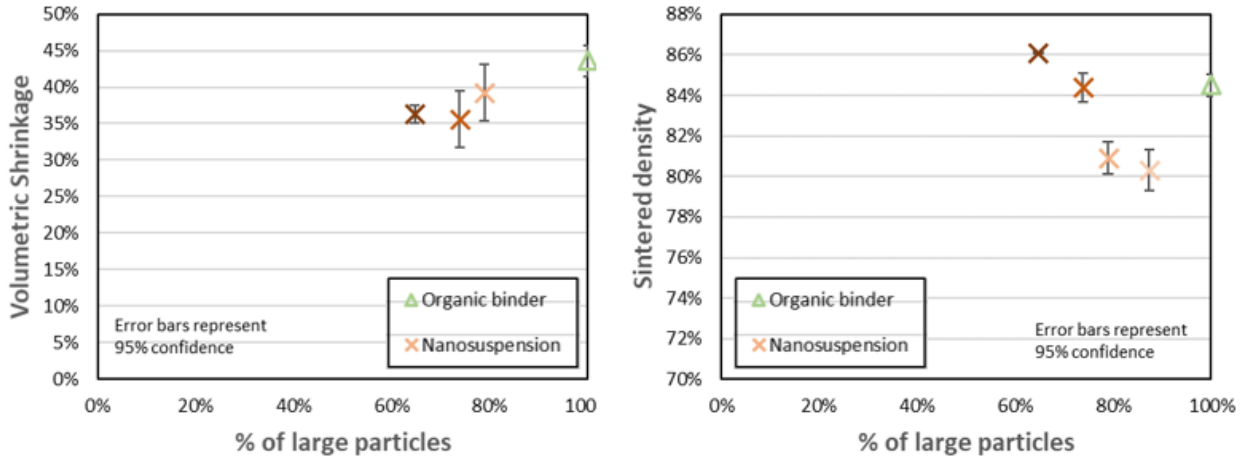

Figure 4.16 Sintering shrinkage (left) and sintered density (right) vs. weight percentage of large powder particles in the printed parts, after sintering at 1075 °C for 600 min.

Similar findings have been observed in printing nanosuspension into a powder bed of bimodal powder mixture (Figure 4.17), created by mixing 5 μm particles into 30 μm particles with improved powder packing density [13]. As the sinter density was significantly improved in bimodal powder compared to monosized particles, the sintered density was not noticeably improved by replacing polymer binder with nanosuspension binder. However, it is clear that the extra content of nanoparticles can produce denser sintered parts, whereas additional organic binder content is harmful for achieving high sintered density.

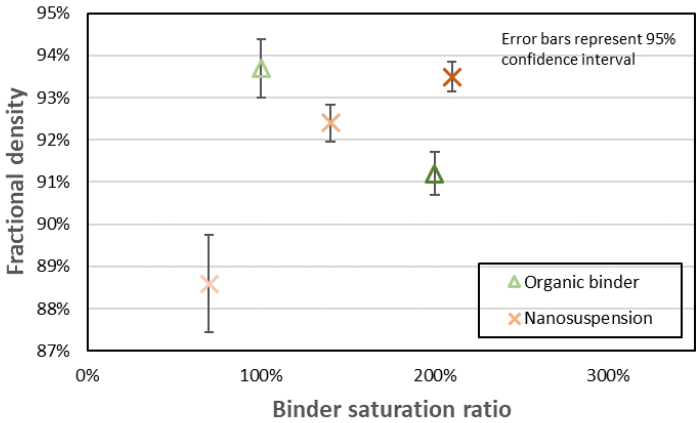

Figure 4.17 Density of parts made by bimodal powder after sintering at 1075 °C for 600 min.

The structural integrity of the printed structure was also improved by the use of nanoparticle binder. While one of the advantages of binder jetting compared to powder bed fusion metal AM processes is the eliminated need to print supports for overhang structures, the sintering of such structure still requires supports to prevent slumping. As the binder pyrolyzes at early sintering stage (450 °C for pyrolizing the organic binder used in this work), it can cause the insufficiently sintered powder skeleton to collapse, or even lead to the loss of printed geometry if the onset of sintering temperature is higher than binder removal temperature (especially in sintering refractory powders). Figure 4.18 shows that the use of nanosuspension as a substitute for organic binder has a potential to improve printed part structural integrity during sintering. Unlike organic binders, the metal binder did not debind during sintering, but rather provided a permanent and structural bonding to the powders. While the creep deformation of overhanging structure still existed, it can be reduced by jetting larger amounts of nanoparticles, according to the previous literature that found the creep deformation of sintered steel can be reduced by over 90% after multiple nanoparticle infiltrating steps [17].

Figure 4.18 Overhang structure after sintering without supports, printed by: polymer binder printed with 100% binder saturation ratio (A), nanoparticle suspension printed with 70% (B) and 140% (C) binder saturation ratio

Finally, the use of metal nanosuspension binder was proved to be capable of improving purity of printed parts (Table 4.3). The purity of printed copper is critical to deliver targeted performance in electrical and thermal conduction applications; however, impurities such as carbon can be introduced to the sintered copper parts as organic binder pyrolysis during sintering. Shown by both surface (EDS) and bulk (OES) spectroscopies, the carbon content was reduced when the polymer binder is substituted with metal binders.

Table 4.3 Carbon content in sintered parts measured by different spectroscopy methods

Binder type	*Carbon content (measured by EDS)*	*Carbon content (measured by OES)*
Polymer binder	4.69 wt%	0.0098-0.013 w.t.%
Copper nanosuspension	2.97-4.11 wt%	0.0044-0.0072 w.t.%

4.4. Conclusions

The goal of this work is to (i) validate the hypothesis of using a nanoparticle suspension ink as the binder for binder jetting, (ii) explore the inkjetted nanoparticle binder's impact on the printed green and sintered part properties. By accomplishing these goals, a correlation between the sintered density and the binder saturation ratio has been established for printing nanoparticle binders. Two different nanoparticle binder systems with different binding mechanisms were investigated: an existing organic binder enhanced with suspended nanoparticles (colloidal organic binder), and a pure metal nanosuspension ink that can be used as a binder (nanosuspension).

The colloidal organic binder can print parts using an identical printing setting with the off-the-shelf organic binder. While the jetted nanoparticles were capable of producing denser green parts (Figure 4.3), the sintered density was not significantly different than the regular organic binder printed parts, as the

density gained in the green part was offset by the reduced sintering densification (Figure 4.4 and Figure 4.5). However, the inkjetted nanoparticles were shown to improve the tensile strength of the sintered parts (Figure 4.8) through a reduced grain size, as they inhibited the grain growth occurred during the prolonged sintering process (Figure 4.6).

This work has shown that the nanosuspension created with a non-adhesive dispersing medium can replace organic binders for printing metal parts. Enabled through the reduced sintering temperature of the nanoparticles, the jetted nanosuspension can be sintered in a heated powder bed to provide necking between powder particles (Figure 4.9 and Figure 4.10), thus providing strength to the printed green parts (Figure 4.11). The use of this metal binder was capable of improving the structural integrity (Figure 4.18) and metal purity (Table 4.3) of the printed sintered parts. As the weight percentage of nanoparticles in the printed parts was increased by the binder saturation ratio, it displayed a positive correlation with the green part strength (Figure 4.11), green part density (Figure 4.12), and sintered part density (Figure 4.16 and Figure 4.17). Compared to the use of organic binders, the jetted nanoparticles constrained the sintering densification and reduced over sintering shrinkage. While it was possible to increase the sintered density with an ultra-high binder saturation ratio, recoating defects can be caused by oversaturated layers and/or the nanoparticle accumulation on top of printed layers (Figure 4.13).

4.5. References

[1] Utela, B. R., Storti, D., Anderson, R. L., and Ganter, M., 2010, "Development Process for Custom Three-Dimensional Printing (3DP) Material Systems," J. Manuf. Sci. Eng., 132(1), p. 11008.

[2] Godlinski, D., and Morvan, S., 2005, "Steel Parts with Tailored Material Gradients by 3D-Printing Using Nano-Particulate Ink," Mater. Sci. Forum, 492–493, pp. 679–684.

[3] Bai, J. G., Creehan, K. D., and Kuhn, H. A., 2007, "Inkjet printable nanosilver suspensions for enhanced sintering quality in rapid manufacturing," Nanotechnology, 18(18).

[4] Bailey, A., Merriman, A., Elliott, A., and Basti, M., 2016, "Preliminary Testing of Nanoparticle Effectiveness in Binder Jetting Applications," Int. Solid Free. Fabr. Symp., pp. 1069–1077.

[5] Bai, J. A., Creehan, K. D., and Kuhn, H. A., 2013, "Powder Particle Layerwise Three-Dimensional Printing Process", US patent application US 2015/0069649 A1

[6] Yoo, H. J., 1995, "Reactive binders for metal parts produced by Three Dimensional Printing," Thesis, Massachusetts Institute of Technology.

[7] Hadjiloucas, C., 1997, "Low Shrinkage Metal Skeletons by Three Dimensional Printing," Thesis, Massachusetts Institute of Technology.

[8] Techapiesancharoenkij, R., 2004, "Bimetallic Bars with Local Control of Composition by Three-Dimensional Printing," Thesis, Massachusetts Institute of Technology.

[9] Bai, Y., and Williams, C. B., 2014, "An exploration of binder jetting of copper," International Solid Freeform Fabrication Symposium, Austin, TX, pp. 793–814.

[10] Asoro, M., Damiano, J., and Ferreira, P., 2009, "Size Effects on the Melting Temperature of Silver Nanoparticles: In-Situ TEM Observations," Microsc. Microanal., 15(S2), p. 706.

[11] Sdobnyakov, N. Y., Samsonov, V. M., Bazulev, A. N., and Kul'pin, D. a., 2008, "On the size dependence of the melting temperature of nanoparticles," Bull. Russ. Acad. Sci. Phys., 72(10), pp. 1371–1373.

[12] Yu, E.-K., Piao, L., and Kim, S.-H., 2011, "Sintering Behavior of Copper Nanoparticles," Bull. Korean Chem. Soc., 32(11), pp. 4099–4102.

[13] Bai, Y., Wagner, G., and Williams, C. B., 2017, "Effect of Particle Size Distribution on Powder Packing and Sintering in Binder Jetting Additive Manufacturing of Metals," J. Manuf. Sci. Eng., 139.

[14] Koju, R. K., Darling, K. A., Kecskes, L. J., and Mishin, Y., 2016, "Zener Pinning of Grain Boundaries and Structural Stability of Immiscible Alloys," JOM, 68(6), pp. 1596–1604.

[15] Hansen, T. W., Delariva, A. T., Challa, S. R., and Datye, A. K., 2013, "Sintering of catalytic nanoparticles: Particle migration or ostwald ripening?" Acc. Chem. Res., 46(8), pp. 1720–1730.

[16] Ravi, B. G., and Chaim, R., 1999, "Sintering of bimodal alumina powder mixtures with a nanocrystalline component," NanoStructured Mater., 11(2), pp. 179–185.

[17] Crane, N. B., Wilkes, J., Sachs, E., and Allen, S. M., 2006, "Improving accuracy of powder-based SFF processes by metal deposition from a nanoparticle dispersion," Rapid Prototyp. J., 12(5), pp. 266–274.

4.6. Appendix A: Electron micrographs of the sintered inorganic nanosuspension inks on solid substrates

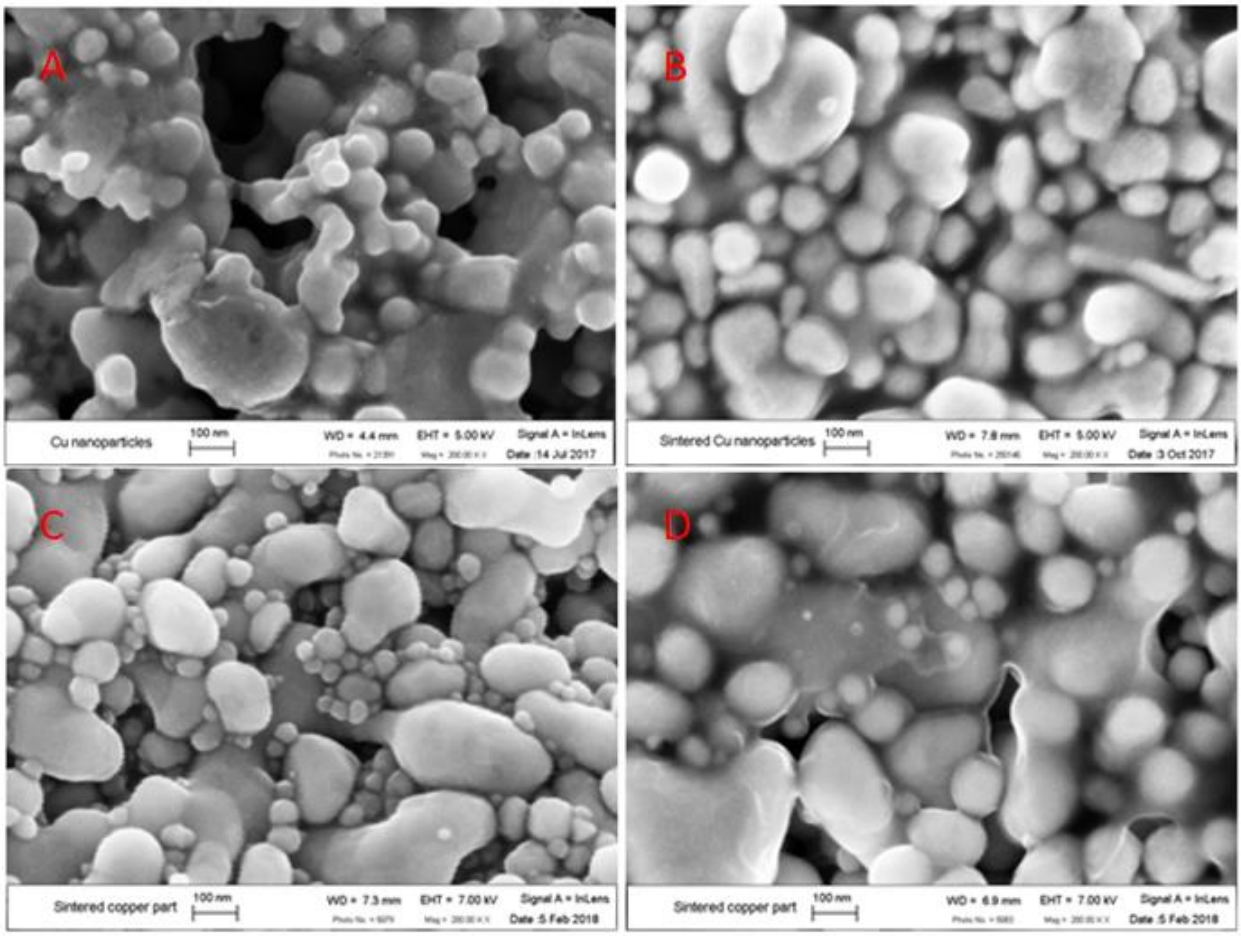

Figure 4.19 Electron micrographs of the inorganic copper nanosuspension heated on a silicon wafer in hydrogen atmosphere, at (A) 190 °C, (B) 250 °C, (C) 400 °C and (D) 600 °C

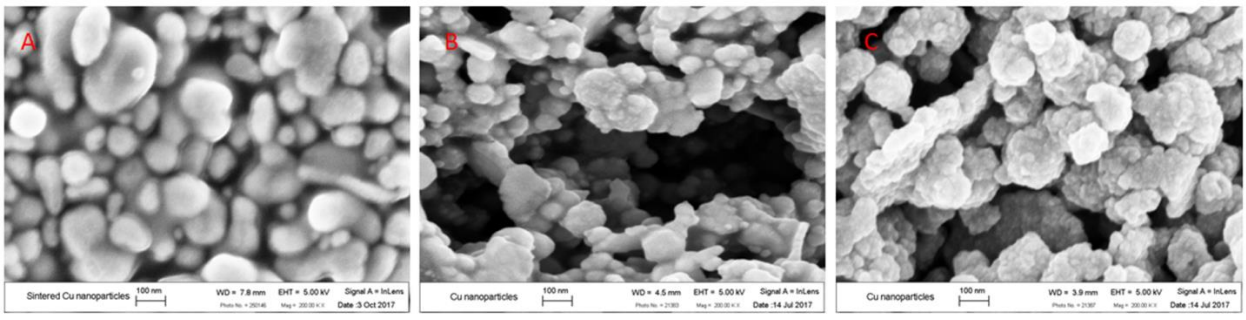

Figure 4.20 Electron micrographs of the inorganic copper nanosuspension heated on a silicon wafer in at 250 °C, in an atmosphere of (A) hydrogen, (B) nitrogen and (C) air

5. Interaction between Nanoparticle Suspension Binder and Metal Powder in Binder Jetting Additive Manufacturing Process

5.1. Introduction

5.1.1. Binder-powder interaction

Understanding and characterizing the binder-powder interaction (binder permeating through powder) is critical for advancing the binder jetting process accuracy, precision, and finished mechanical properties. When a droplet is released from the inkjet nozzle and brought into contact with a powder bed, it begins to spread and simultaneously penetrate into the powder. The result of binder penetration into the powder is a powder-binder granule formed within the loosely packed powder bed. This granule is also the primitive in binder jetting and the fundamental building block that constitutes a printed part. Printing resolution in binder jetting can be determined when the primitive size and morphology is known

The ability of a binder wetting and permeating into a powder constitutes the main criteria of determining a material's compatibility with the binder jetting process. Separately studying spreading (e.g., static contact angle) or penetration (e.g., binder absorption time) is insufficient to describe the binder permeating powder process and determine whether a material is "printable", as the binder-powder interaction in binder jetting is a simultaneous occurrence of both. As a result, there is a need to define a metric to fully describe the binder permeation into a powder.

Studying the binder-powder interaction can also guide the selection of printing parameters in binder jetting. The strength of a printed green part is gained from overlapping the primitives within a layer (i.e., drop spacing) and stitching primitives across the printed layers (i.e., layer thickness) (Figure 5.1). Therefore, knowing primitive size and morphology can guide the selection of layer thickness and binder droplet spacing, the two most essential binder jetting printing parameters, to achieve desired primitive overlapping and green strength. Layer thickness and binder droplet spacing, along with a known droplet volume, can be used to calculate binder saturation ratio (defined as the ratio of total amount of binder versus total pore volume in a printed part), which is another common printing parameter that is usually determined from experimental design [1,2].

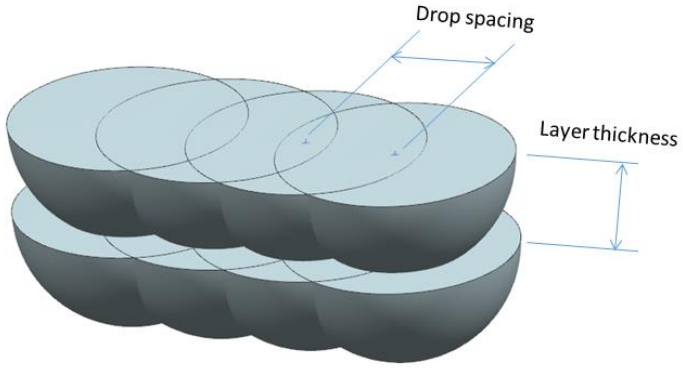

Figure 5.1 Overlapping primitives to form printed parts

Recognizing the importance of understanding the binder-powder interactions, capillary models developed for liquids wetting porous materials [3–5] have been applied in the context of binder jetting. Holman et al. studied how binder infiltration rate is affected by the pore size in slurry-based ceramic powder beds, and how it determines the drop diameter (drawing area) on powder [6]. Miyanaji *et al.* addressed the binder imbibition and drainage behaviors by establishing a relationship between capillary pressure and binder saturation level at equilibrium state of binder permeation [7]. While the capillary flow

characteristics are considered to describe the in the binder-powder interaction in the literature, the contact angle was determined from static-based experiments and did not reflect the dynamic fluid behaviors inside capillary pores.

The printed primitive in binder jetting was studied by Cima *et al.* through creating primitives by sieving printed individual binder-powder agglomerates from loose powder [8]. The printed primitives have shown spherical curvature and higher packing density than loosely packed powder, as a result of the surface tension in binder that rearranges powder particles. However, the information on primitive morphology and binder penetration depth was difficult to be directly interpreted due to the small scale of the printed primitives in binder jetting.

To address these gaps, there exists an opportunity to create an experimental approach to suitably characterize the binder-powder interactions in binder jetting. Coupled with models of capillary flow, the dynamic behaviors of the binder flow inside powder capillary pores needs to be described.

5.1.2. Nanoparticle suspension binders

A better understanding of binder-powder interactions and an experimental technique to characterize binder permeation and primitive formation can be used to screen material and define process parameters for new binder developments. Among different types of binding agents used in binder jetting [9], colloidal suspensions of particles in polymer binder have been investigated for printing metals or ceramics, with demonstrated benefits of (i) improving sintered part strength and structural integrity [10], (ii) improving sintered density [11], and (iii) spatial control of chemical composition of printed parts [12]. While the material properties of the parts printed by nanoparticle binder have been studied the literature, there exists gap to understand the effects of a nanoparticle binder on the binder jet printing process, as the binder-powder interactions are typically influenced the binder rheology and the nanoparticle solid loading in a suspension is known for having impacts on its viscosity and surface tension.

The viscosity of a particle suspension (μ) is a complex function of its physical properties, including particle volume fraction ($\emptyset$), particle shape, original fluid viscosity (μ_0), and interactions between particles [13]. Non-Newtonian fluid properties can be observed in particle suspensions, but it is more evident in suspensions with high particle concentration and strong inertia effects (i.e., high Reynolds number) [14], or strong fluid-solid coupling (i.e., small Stokes number) [15]. The particle volume fraction in a suspension usually has the dominant role in affecting its viscosity. The Krieger & Dougherty model (Equation 5.1) correlates the solid loading of a particle suspension to the fractional viscosity by considering the contribution of successive packets of suspension to the maximum allowed particle volume fraction ($\emptyset_m$) [16], where B (Einstein coefficient) and $\emptyset_m$ can be determined by fitting to experimental data.

$$\frac{\mu}{\mu_0} = \left(1 - \frac{\emptyset}{\emptyset_m}\right)^{-B\emptyset_m} \qquad (5.1)$$

The impact on liquid –vapor interfacial surface tension (γ_{LV}) imposed by suspended particles is complicated, as different colloidal systems have displayed contradictory trends in the literature. When the solid loading of suspended particles increases, the surface tension may (i) increase due to the attractive force (e.g., Van der Waals force) between particles that increases surface free energy at the liquid –vapor interface [17,18], (ii) decrease due to Brownian motion and reduced effective interface area when nanoparticles with repulsive forces accumulate to the interfaces [19-21], or (iii) decrease at low concentration and then increase at high concentration [22]. Despite the fact that different trends in changes of surface tension as a result of suspending nanoparticles have been reported in the literature, it is believed that particle solid loading typically has a significant impact on the surface tension of a

suspension. Furthermore, the base fluid is also an important factor as it has shown that the presence of polymer groups in a suspension can increase the electrostatic force between particles and thus reduce surface tension [18].

As a result, it is hypothesized that the suspended nanoparticles impose strong influence on binder rheology, which ultimately affects the powder wettability and primitive formation in binder jetting.

5.1.3. Context

The objectives of this work are to (i) create a characterization tool to describe binder permeation and measure primitive size, (ii) develop a fundamental understanding of how primitive formation is affected by binder-powder interaction, and use this gained understanding to (iii) investigate the effect of nanoparticle suspension binder on the size of printed primitives.

To achieve these goals, an experimental approach based on powder bed sessile drop goniometry is created to characterize the binder-powder interaction and primitive size for binder jetting. The dynamic contact angle of binder inside the powder capillary pores is defined as the metric for evaluating binder permeation process, which is calculated from the measured penetration time obtained from the sessile drop experiment. The powder granules created by binder sessile drops mimic the shape of primitives created by inkjet drops in binder jetting, and therefore is used to predict primitive dimensions and to guide printing parameter selections. It is hypothesized that the dynamic contact angle formed at the interface between binder and powder pores determines the primitive size, as a smaller contact indicates a better powder wettability and deeper penetration depth (Figure 5.2).

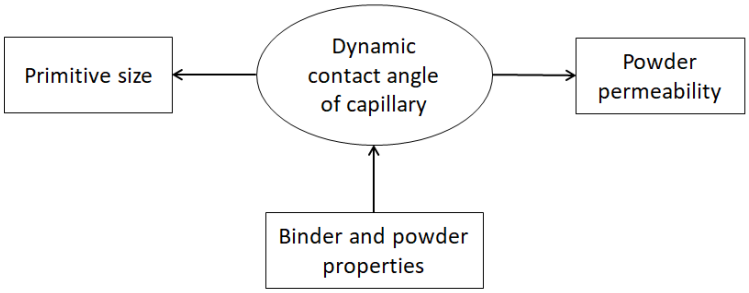

Figure 5.2 Linking binder rheology to binder-powder interaction and primitive formation using the dynamic contact angle in capillaries

This developed methodology is then used to study how suspended copper nanoparticles in the binder affect its interaction with copper powder and selection of printing parameters. Section 5.2 provides a review of the powder granulation theories and models that can be applied to binder jetting, to understand the binder-powder interaction mechanisms and define a suitable metric for describing the process. Section 5.3 describes the sessile drop goniometry experimental approach to characterize binder-powder interaction. Experimental results from this approach to evaluate the impact of nanosuspension binder relative to organic binder are discussed in Section 5.4.

5.2. Powder bed sessile drop goniometry

In the powder-bed based sessile drop goniometry, a binder drop is released from a needle and impacts the powder bed. As a contact angle forms at the binder-powder interface and progresses as the binder drop spreads and penetrates into powder (Figure 5.3), a contact angle – time plot is constructed. This plot can be used to provide information on binder penetration characteristics.

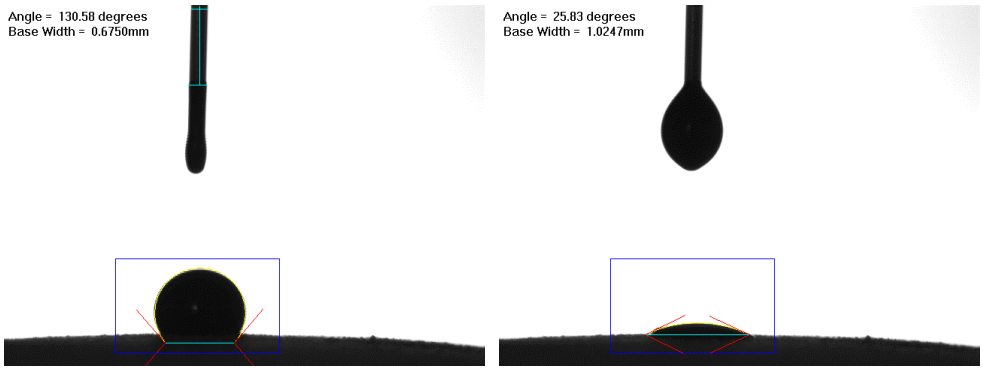

Figure 5.3 Recorded contact angle from initial contact (left) to completed absorption (right)

Despite the drop volume difference between the size of sessile drops and inkjet drops, the sessile drop goniometry conducted on a powder bed substrate is believed to be able to provide a suitable simulation of binder jetting process, and derive useful information for understanding the binder-powder interaction. A description of the binder-powder interaction mechanisms in binder jetting is offered in Section 5.2.1. The capillary dynamic contact angle as a metric is firstly defined in Section 5.2.2 to describe the binder-powder interaction. Section 5.2.3 describes the process for deriving the defined metric from powder bed sessile drop goniometry. The characterization for primitive formation is discussed in Section 5.2.4.

5.2.1. Physical picture of binder-powder interaction

As a binder droplet impacts the powder surface (Figure 5.4A), a contact angle forms at the binder-powder interface as a result of binder wetting powder (Figure 5.4B). As soon as the binder is in contact with powder, the pores between powder particles act as capillary tubes to absorb the liquid into the powder. The contact angle therefore decreases as the droplet imbibes into the powder (Figure 5.4C).

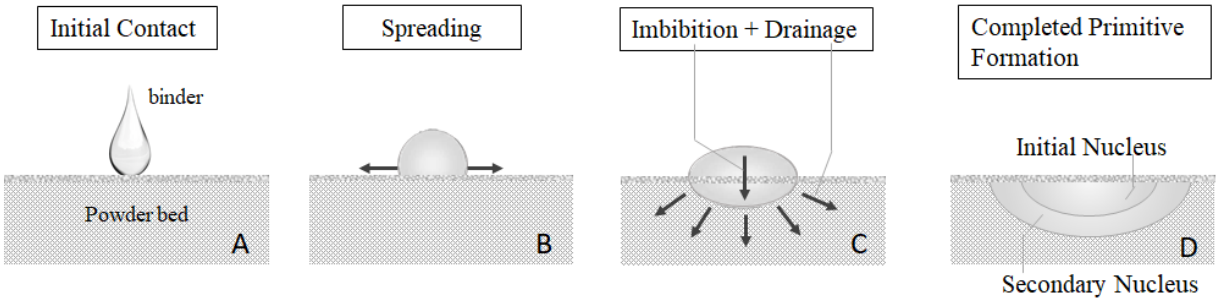

Figure 5.4 Binder-powder interaction and primitive formation process in binder jetting

As the binder droplet wets and penetrates into powder bed, an initial nucleus forms with the entire pore space filled with binder (100% saturation ratio). Surrounded by dry loose powder with zero saturation, the initial nucleus undergoes a secondary nucleus growth driven by capillary pressure, wherein the binder drains from saturated regions to dry regions and simultaneously imbibes more binder from the powder bed surface (Figure 5.4D). The nucleus growth will stop once an equilibrium state is reached. The saturation ratio of the nucleus at this state is called equilibrium binder saturation ratio [23], which is an intrinsic property of the binder-powder combination that describes how much binder a powder can sustain in its pore. The equilibrium saturation ratio should be differentiated from the overall printed part saturation ratio, which is calculated from printing parameters (detailed in Section 5.4.3).

5.2.2. Defining a metric for describing the binder-powder interaction

The solid-liquid contact angle (θ) is the angle formed by a liquid drop placed on a solid surface at the three phase contact line (Figure 5.5). It is the most common parameter used to describe the wetting ability of a liquid on a solid surface.

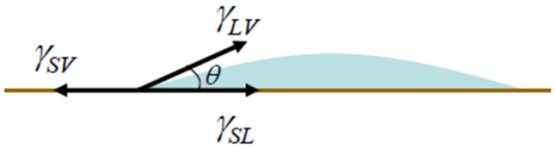

Figure 5.5 Static contact angle at solid-liquid-vapor interface

When a liquid approaches a smooth and non-porous solid surface, a static contact angle will form once an equilibrium state is reached from the force balance of interfacial surface tensions, as described by the Young's equation in Equation 5.2.

$$\gamma_{SV} = \gamma_{SL} + \gamma_{LV} cos\theta \qquad (5.2)$$

There is a need to distinguish the difference between intrinsic contact angle (θ) in Figure 5.5, apparent contact angle on powder bed (θ_a), and dynamic contact angle of binder wetting the powder particle in capillary pores (θ_d) in Figure 5.6.

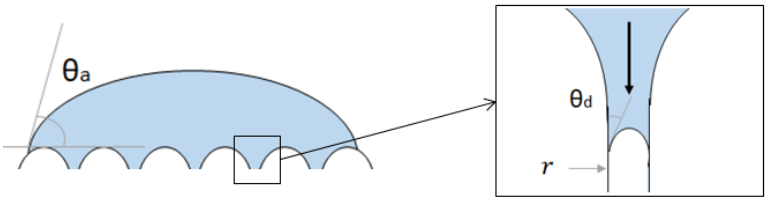

Figure 5.6 Apparent contact of binder spreading on powder bed (θ_a) vs. dynamic wetting contact angle in the powder capillary pores (θ_d)

The apparent contact angle formed between a binder drop spreading on powder bed (θ_a) does not equal to the intrinsic contact angle (θ), due to the heterogeneous rough powder surface [24]. In fact, the contact angle on rough surface is smaller than that on polished surface [6]. Several methods exist for measuring apparent contact angle on a nonabsorbing powder surface, including using a thin layer of powder or compacted powder disks in sessile drop, Wihelmy plate, and Washburn capillary rise experiments [25]. On a realistic absorbing powder surface, the apparent contact angle experiences two stages from the initial contact with a powder surface to complete absorption: (i) advancing angle as it spreads over the surface, and (ii) receding angle as the liquid penetrates into the powder [26]. As both advancing and receding angles display an exponential decay over time (recorded with high speed camera), the static apparent angle can be estimated by curve fitting the experimental data.

While a static apparent contact angle (θ_a) measured from sessile drop goniometry can provide information on binder spreading, it is insufficient to describe the binder-powder interaction in binder jetting. The dynamic contact angle (θ_d) formed between binder and powder particles inside capillary pores during binder penetration is more suitable for binder jetting, as it includes both binder spreading and binder penetration factors. For dynamic wetting where the interface line moves, the dynamic contact angle (θ_d) is typically different than static contact angle (θ). A correlation between dynamic and static contact angle has been established using an empirical factor (a) and capillary number (Ca), which depends on binder surface tension (γ_{LV}), viscosity (μ), and liquid velocity (v) (Equations 5.3 & 5.4) [27].

$$Ca = \frac{\mu v}{\gamma_{LV}} \qquad (5.3)$$

$$cos\theta_d - cos\theta = a\sqrt{Ca} \qquad (5.4)$$

5.2.3. Deriving dynamic contact angle

While dynamic contact angle in capillaries cannot be directly measured from the powder bed sessile drop goniometry, it can be derived from the measured penetration time.

Capillary pressure is the main driving force behind binder penetration. When a small capillary tube is brought into contact with a pool of liquid, the liquid will spontaneously rise due to capillary pressure as the fluid tends to wet the interior of the tube and spread up the capillary walls. The pressure difference that drives a liquid rise in motion is capillary pressure (P_{cap}), which depends on interfacial surface tension (γ_{LV}), dynamic contact angle (θ_d), and capillary radius (r) [26]:

$$P_{cap} = \frac{2\gamma_{LV}cos\theta_d}{r} \qquad (5.5)$$

If the fluid is assumed to be Newtonian laminar flow with low Reynolds number, the volume flow rate driven by capillary pressure can be expressed by the Poiseuille equation (Equation 5.6), showing capillary driven flow is resisted by viscous flow. Two forms of Washburn equation, derivative and integrative (Equations 5.7 & 5.8), can therefore be derived by applying capillary pressure (Equation 5.5) in the expression of flow rate (Equation 5.6).

$$\frac{dV}{dt} = \frac{\pi P_{cap} r^4}{8\mu h} \qquad (5.6)$$

$$\frac{dh}{dt} = \sqrt{\frac{r\gamma_{LV}cos\theta_d}{8\mu t}} \qquad (5.7)$$

$$h = \sqrt{\frac{r\gamma_{LV}cos\theta_d t}{2\mu}} \qquad (5.8)$$

The Washburn equations describe the rate (dh/dt) and height (h) of a liquid rise into a capillary tube with radius (r). In binder jetting, the penetration depth corresponds to the capillary rise height (h), and is proportional to the square root of the capillary radius and surface tension, and inversely proportional to the square root of the fluid viscosity (Equation 5.8).

Further models have been to developed in the literature to specifically describe the liquid penetrating powder process based on Washburn equations [4,5]. The models simplify the powder surface as a solid consisting of a number of parallel capillaries. The flow rate of liquid penetrating powder (dV/dt) can be expressed as Equation 5.9, where R is the liquid wetting area and φ is powder porosity.

$$\frac{dV}{dt} = \pi R^2 \varphi \frac{dh}{dt} \qquad (5.9)$$

Substituting the Washburn equation (Equation 5.7) into the flow rate expression (Equation 5.9) and integrating over time (t) gives Equation 5.10, which leads to the total time duration of binder penetration (T) when setting droplet volume (V_0) to zero and assuming the radius of the affected powder area (R) equals to the radius of liquid droplet, which is simplified as spherical-shaped (Equation 5.11).

$$V = V_0 - \pi R^2 \varphi \sqrt{\frac{r\gamma_{LV}cos\theta_d t}{8\mu}} \qquad (5.10)$$

$$T = 1.35\frac{{V_0}^{2/3}\mu}{\varphi^2 r\gamma_{LV}cos\theta_d} \qquad (5.11)$$

The capillary radius (r) in a powder is difficult to be directly measured, but can be estimated by the porosity (φ), surface area (S), material density (ρ), and Sauter mean diameter (d) of a powder [5] with different models (Equation 5.12 & 5.13). Sauter mean diameter is an average of particle size in fluid mechanics that is defined as the diameter of a sphere that has the same volume/surface area ratio as a particle of interest. For simplicity, it is estimated by the average diameter (d) of the powder used in this study.

$$r = \frac{2\varphi}{(1-\varphi)S\rho} \qquad (5.12)$$

$$r = \frac{d\varphi}{3(1-\varphi)} \qquad (5.13)$$

Prior work has shown that Equation 5.13 is more accurate to estimate pore size as it accounts for the large voids in a loosely packed powder that does not contributes to total capillaries; while the surface area (S) measured by BET does not reflect the actual wetting areas [5]. Ultimately, the dynamic contact angle in capillaries can be expressed by combining Equation 5.11 and 5.13 (Equation 5.14).

$$cos\theta_d = \frac{4.05\mu(1-\varphi){V_0}^{\frac{2}{3}}}{T\varphi^3\gamma_{LV}d} \qquad (5.14)$$

The dynamic contact angle in capillary pores (θ_d) can therefore be calculated by the measured binder rheology (γ_{LV} and μ), powder size (d) and packing density (φ), and the drop volume (V_0) and total penetration time (T) that are measured from the sessile drop goniometry.

5.2.4. Powder granulation and equilibrium binder saturation ratio

The powder agglomerates formed by a single binder droplet penetrating into the powder can mimic a scaled-up printed primitive in binder jetting. The powder granules obtained from the sessile drop goniometry were retrieved from the loose powder after heating the entire powder substrates at 200 °C to cure the binder. The diameter (D) and height (H) of retrieved powder granules were measured using an optical microscope. For approximation purpose, the volume of the granule was calculated by assuming it is spherical cap shaped (Equation 5.15). The approximation is validated through the fact that the surface tension of a liquid tends to form a spherical frontier during penetration [8].

$$V_{granule} = \frac{1}{6}\pi H(\frac{3}{4}D^2 + H^2) \quad (5.15)$$

Equilibrium saturation ratio is another metric for liquid-powder interaction that is directly related to the capillary action and nucleus growth. The equilibrium saturation ratio (S_e) can be estimated by the ratio of binder drop volume (V_{binder} measured by the pendant drop goniometry) to the pore volume of the binder-powder granules (Equation 5.16), as indicated in Equation 5.16.

$$S_e = V_{binder}/[V_{granule}(1-\varphi_{powder})] \qquad (5.16)$$

The deeper a binder penetrates into powder driven by large capillary pressure, the larger the nucleus becomes, resulting in less binder content in the pore and smaller equilibrium binder saturation ratio. This trend is evident in a relationship that exists between capillary pressure and equilibrium saturation ratio (Figure 5.7), where large capillary pressure typically results in less moisture content [28,29]. In the high saturation ratio region, the small capillary pressure drop usually results in large saturation loss. The exact relationship can be obtained from experimental approaches (e.g., soil moisture tensiometer or filter paper

method), and has been used in binder jetting contexts to predict equilibrium binder saturation ratio after the capillary pressure is determined [7,30].

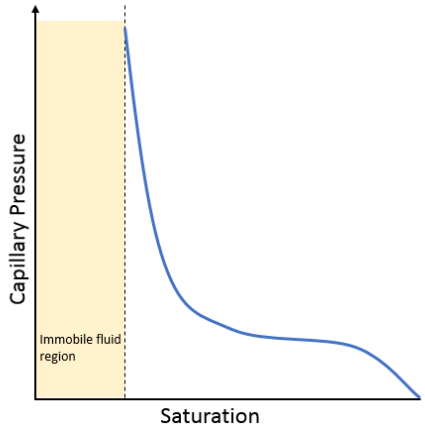

Figure 5.7 Typical capillary-saturation curve for liquid-powder interaction

It is noted that the powder bed sessile drop experiment does not exactly match the process conditions in binder jetting in (i) droplet volume, (ii) droplet velocity, and (iii) powder bed temperature, but can still provide a viable platform to simulate the binder jetting process and reveal the fundamental relationships in binder-powder interaction.

5.3. Experimental methods

In order to (i) validate the powder bed sessile drop goniometry approach and (ii) gain an understanding on how nanoparticle binders affect the binder jetting process, experiments were conducted in the context of binder jetting copper nanoparticle binder to print copper parts [31]. Solid loadings of nanoparticle inks were varied in the experiments to study their impacts on powder wettability and primitive formation. Powder size was varied in order to gain further insight in how particle size distribution and pore size affect binder-powder interaction

The binder-powder interaction and primitive formation in using nanoparticle suspension as the binder was studied by the models and approaches established in Section 5.2. The apparent contact angle was measured at the binder-powder interface and plotted against time, which was then interpreted to derive the information on powder permeability in the form of dynamic contact angle. The penetration depth was evaluated by measuring the dimensions of the binder-powder granules generated from the sessile drop experiment.

5.3.1. Nanoparticle binder preparation and characterization

ExOne's solvent-based binder was chosen for its success of printing copper parts demonstrated in prior work [32]. The nanoparticle binders were prepared by dispersing copper nanoparticles (in the form of nanoparticle paste with 75 wt% metal content) into the ExOne's organic binder at weight percentages of 10%, 20% and 30% to generate solid loadings from 7.5 to 22.5 wt%. The copper nanoparticle paste used in this study is a commercially available product designed for screen printing and low temperature sintering (Sun Chemical). Satisfactory suspension stability was obtained through sonicating and magnetic stirring (30 minutes) the prepared nanoparticle in polymer dispersions.

The viscosity and surface tension of the polymer binder and the nanoparticle binders were measured by a rotational rheometry (TA hybrid rheometer with concentric cylinder) and a pendant drop goniometry. The binder density was measured by a graduated cylinder.

To ensure the nanoparticle suspension binders are suitable for inkjet printing, the binder jettability was predicted by the Ohnesorge number (*Oh*) (Equation 5.17), which is a function of an ink's viscosity (μ), density (ρ), surface tension (γ), and nozzle diameter (D). Specifically, if the inverse of the Ohnesorge number of an ink has a value between 1 and 10, then the ink is likely to be successfully jetted on most commercial Drop-On-Demand (DOD) platforms [33].

$$Oh = \frac{\sqrt{We}}{Re} = \frac{\mu}{\sqrt{\rho\gamma D}} \qquad (5.17)$$

Jettability was experimentally validated on an inkjet printing test setup (MicroFab Technologies). The setup consists a single nozzle piezoelectric printhead, a controller to deliver researcher-determined waveforms to the printhead, and a strobe and coupled CCD camera, which enables the imaging of jetted fluids.

5.3.2. Powder preparation

Three copper powders were evaluated in this study to gain further insight in how particle size distribution (Figure 5.8) and pore size (Table 5.1) affect binder-powder interaction. The pore size was estimated by powder packing density and particle size (Equations 5.13). The particle size distributions were measured by laser diffraction (Horiba LA-960 Laser Particle Size Analyzer) with distribution curve shown in Figure 5.8. Compared to the powders with narrow size distribution, 30+5 µm powder is a powder mixture created by mixing 27 wt% 5 µm powder into 30 µm powder, which has been shown to improve powder packing [34]. Powder packing density was measured using a Hall flow meter (ASTM Standard 212). Tap density was measured using a graduated cylinder with tapping apparatus (ASTM Standard 527).

Petri dishes containing loose copper powder were used as the substrate in the powder bed sessile drop goniometry. The petri dish was gently tapped to create a flat surface for contact angle measurement, but apparent density can still be assumed for the powder packing density as extensive powder tapping or compacting was avoided.

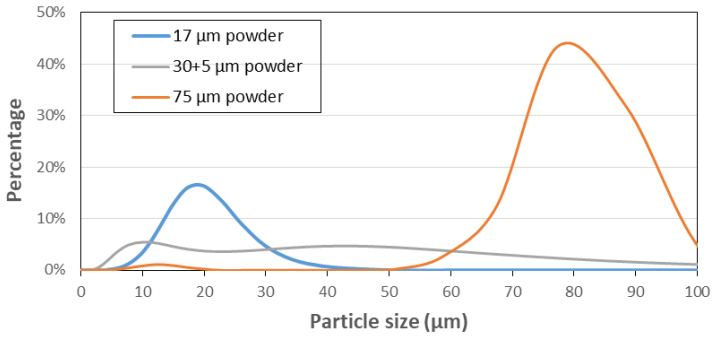

Figure 5.8 Particle size distribution of tested powders

Table 5.1 Summary of powder properties

Powder name	*Median particle size*	*Packing density*	*Tap density*	*Pore size*
17 µm powder	17.0 µm	52.9%	65.1%	5.0 µm
30+5 µm powder	17.4 µm	53.7%	63.9%	5.0 µm
75 µm powder	77.9 µm	56.1%	64.9%	20.3 µm

5.4. Results and discussion

5.4.1. Ink rheology and jettability

The measured viscosity of the polymer binder and the nanoparticle binders with various solid loadings is shown in Figure 5.9. Despite the rise of viscosity at high shear rate that was caused by the measurement error associated with fluid vortex, the tested binders have shown a Newtonian behavior without clear shear thinning or thickening effect. A higher solid loading has increased the binder viscosity according to the Krieger & Dougherty model, which is shown in a curve fitted model based on the plot of the viscosity (averaged across the tested shear rate range) versus nanoparticle volume fraction (Figure 5.10).

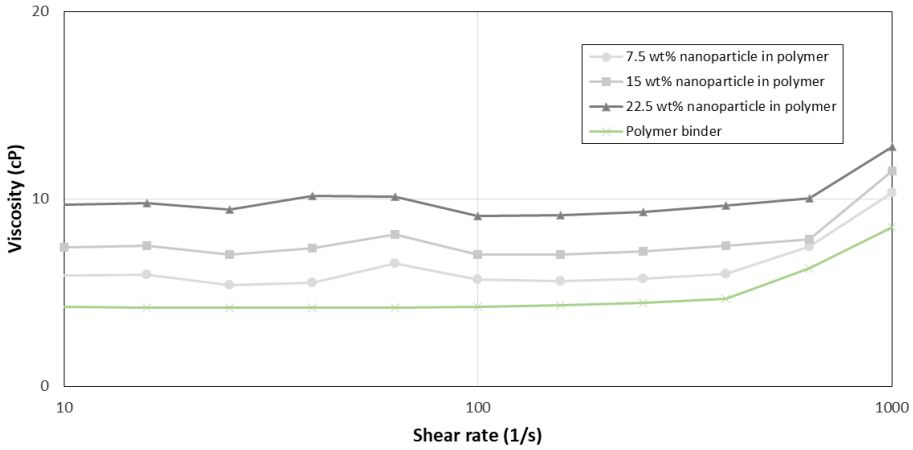

Figure 5.9 Viscosity of polymer binder and nanoparticle-polymer dispersions at different solid loading

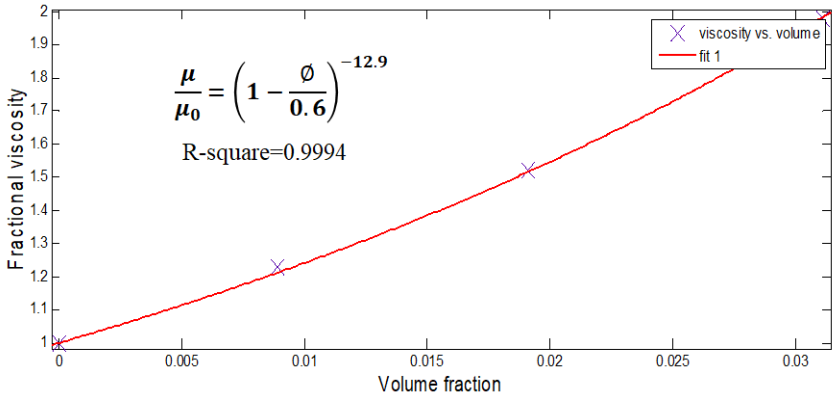

Figure 5.10 Fractional viscosity versus nanoparticle volume fraction with a curve fitted model

The interfacial surface tension at liquid-vapor interface (γ_{LV}) has shown a declining trend as the nanoparticle solid loading was increased (Table 5.2). This is believed to be caused by the repulsive force between nanoparticles as a result of polymer attachment, according to the literature reviewed in Section 5.1.2. The calculated Ohnesorge number shows that all binders investigated in this work were within jettable range using a piezoelectric nozzle with 55 µm diameter. The jettability was experimentally verified in a single nozzle inkjet test (Figure 5.11) using a trapezoidal waveform (70 V voltage, 20 µs dwell time, 5 µs rise/drop time).

Table 5.2 Summary of rheology and calculated Oh numbers for polymer binder and nanoparticle-polymer dispersions at different solid loading

Solid loading (wt%) of suspended nanoparticle in polymer binder	*Density (g/mL)*	*Viscosity (cP)*	*Surface tension (mN/m)*	*Ohnesorge number (Oh)*	*1/Oh*
0%	0.99	4.86	28.16	0.12	8.06
7.5%	1.08	5.98	22.92	0.16	6.17
15.0%	1.14	7.40	22.55	0.20	5.08
22.5%	1.23	9.63	19.76	0.26	3.80

Figure 5.11 Inkjet testing of polymer binder (A), 15wt% (B) and 22.5 wt% (C) nanoparticle binder

5.4.2. Binder-powder interaction

5.4.2.1. Powder bed sessile drop goniometry

The time profile of the directly measured contact angle at the interface between binder and powder is presented in Figure 5.12. In the literature of powder apparent contact angle measurement [35], exponential decay has been observed for both advancing angle (from initial contact to the equilibrium state of spreading) and receding angle (from spreading equilibrium to completed absorption). While the contact angle measurement in this work exhibited an exponential decay over time, no clear distinction between advancing and receding angle was observed, due to fast absorption and relatively slow image capture frequency of the camera (67 milliseconds interval). The binder penetration time was then extracted from the contact angle plots by assuming 80% of the binder volume is absorbed when the powder apparent contact recedes below 15 degrees.

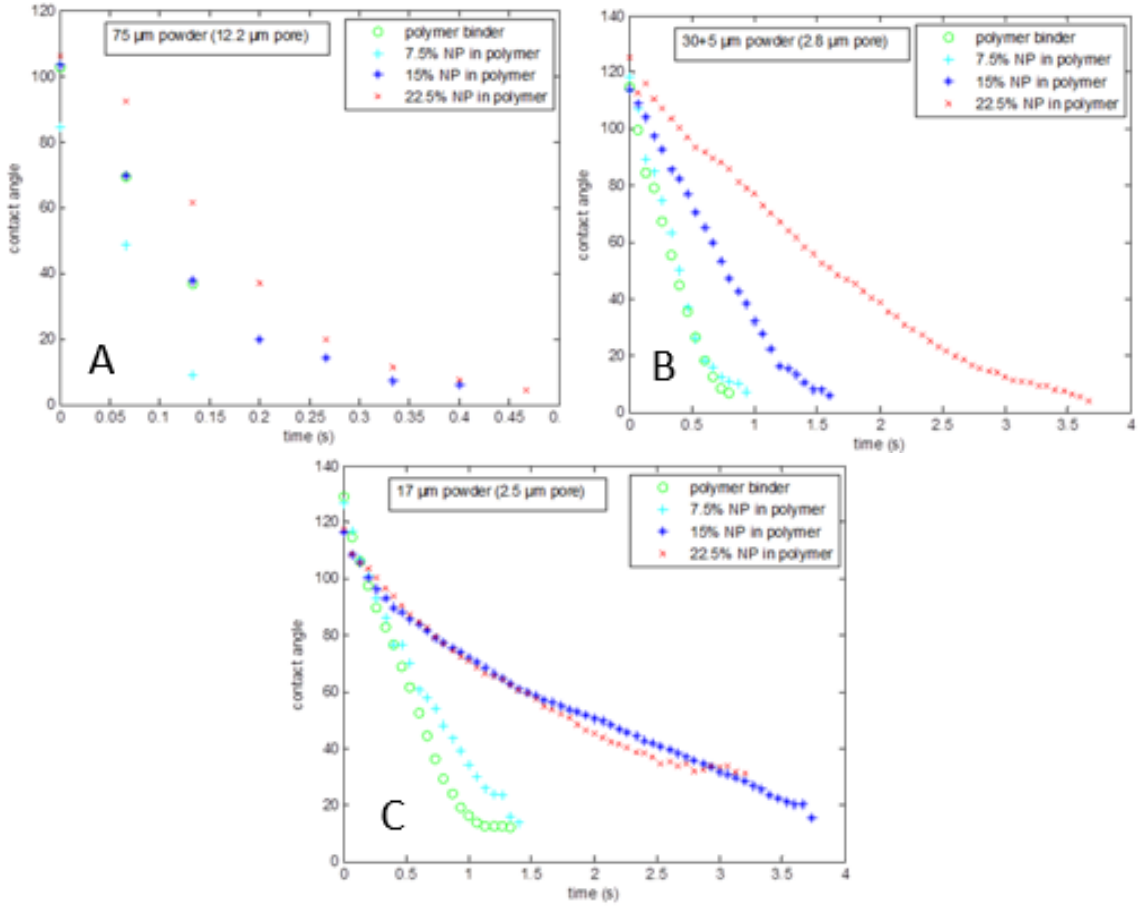

Figure 5.12 Measured apparent contact angle as binder penetrates into the (A)75 µm, (B) 30+5 µm, and (C) 17 µm powder with a decreasing pore size of 12.2 µm, 2.8 µm, and 2.5 µm respetively

The powder sessile drop experiment has shown that the high nanoparticle solid loading and small powder pore size significantly increased the binder penetration time (Figure 5.12). The normalized penetration time (second per unit drop volume) against solid loading of nanoparticles for each powder is plotted in Figure 5.13. The penetration time was estimated as the time span from the initial binder-powder contact to the contact angle receding below 15 degrees.

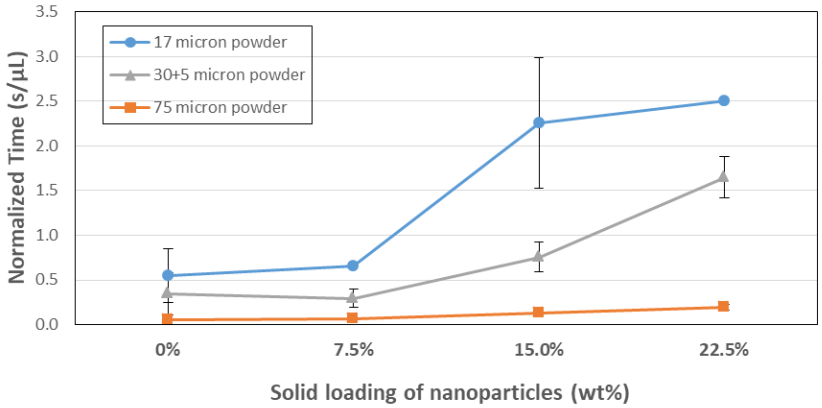

Figure 5.13 Penetration time vs. solid loading of nanoparticles for different powder

The higher viscosity (Figure 5.10) and lower surface tension (Table 5.2) in high solid loading nanoparticle binders has led to a prolonged binder penetration process (Figure 5.13), as a result of the reduced capillary pressure and increased fluid resistance. It is also evident that the coarse powders (75 µm) allowed faster binder penetration through enlarged pore (Table 5.1). While 30+5 µm and 17 µm powder have a similar pore size, the bimodal powder's wider particle size distribution created a more powder contact points and more available capillary tubes, which contributed to a reduction of penetration time compared to the monosized powder.

5.4.2.2. Dynamic capillary contact angle

The calculated dynamic contact angle is plotted against nanoparticle solid loading in polymer binders for each recipient powder (Figure 5.14). It can be observed that the dynamic contact angle in capillary pores was affected by both binder solid loading and powder pore size, but ultimately determined by the capillary number, a measure of the relative effect of viscous forces versus surface tension (Equation 5.3).

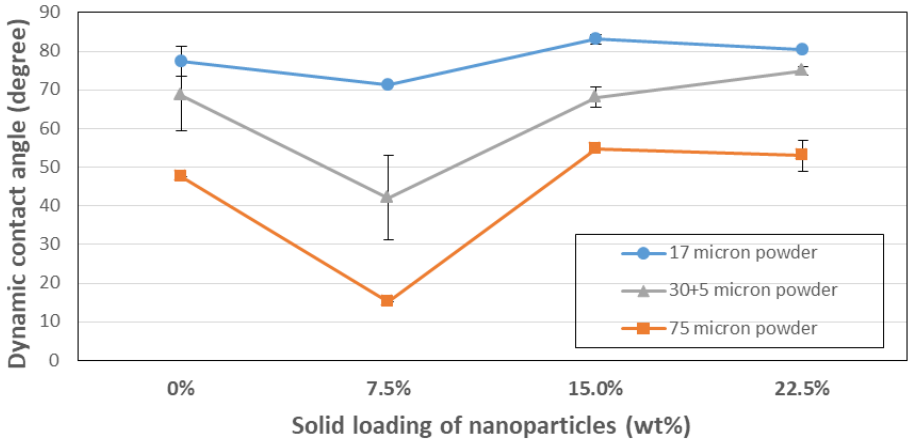

Figure 5.14 Dynamic contact angle vs. solid loading of nanoparticles for different powder

Figure 5.15 shows the calculated capillary number for each binder-powder combination. The average capillary flow velocity was calculated from the estimated binder flow rate by treating it as a laminar 1D Newtonian flow. Compared to the pure polymer binder, the initial introduction of nanoparticles (7.5 wt% solid loading) generated a larger capillary number as a result of enhanced capillary action around nanoparticles [20]. As the solid loading increased in the nanoparticle binder (7.5-22.5 wt%), the capillary pressure was reduced due to the increased fluid resistance, which resulted in smaller capillary number. A large capillary number is an indication of good wettability in capillary pores, and therefore is associated with smaller dynamic capillary contact angle [27].

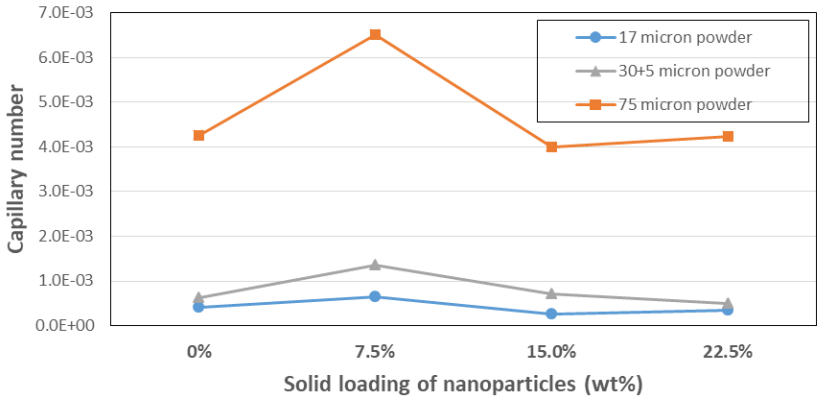

Figure 5.15 Calculated capillary number for each binder-powder combination

5.4.3. Primitive formation

5.4.3.1. Binder penetration

Figure 5.16 shows an example of the powder granules retrieved from the powder substrates used in binder sessile drop experiment. The normalized radial diameter and vertical depth of the powder granules generated from sessile drop goniometry is presented in Figure 5.17. The normalized values were used by dividing the measured granule dimensions by the diameter of the binder droplet (treating the droplet as spherical shaped) to eliminate the drop volume's impact.

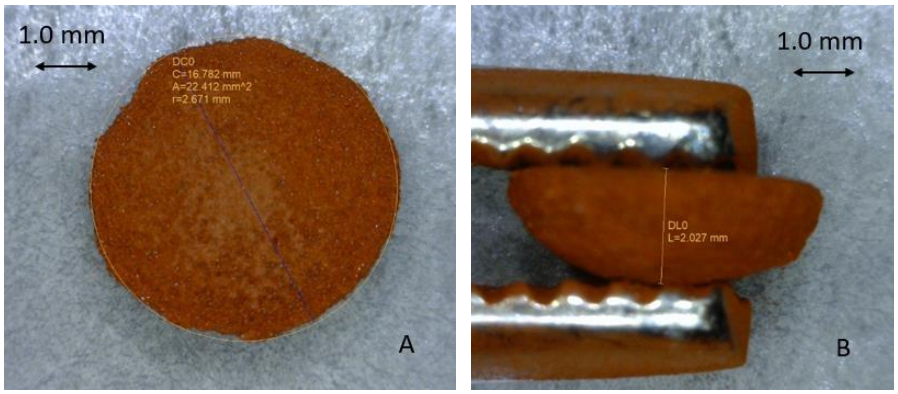

Figure 5.16 Top view (A) and side view (B) of powder granule generated from binder sessile drop absorbed into powder

Despite the data variance, a general trend can be observed that (i) the low solid loading of copper nanoparticles (7.5 wt%) increased the binder penetration depth relative to the polymer binder, and (ii) higher nanoparticle solid loadings reduced the binder penetration depth. The trend observed in penetration depth was correlated to the dynamic contact angle, especially in the diameter of 17 and 30+5 µm powder granules. The powder with a larger pore (75 µm) was less sensitive to the nanoparticle solid loading change. It can be concluded that small dynamic contact angle and higher capillary number correlates to better wettability in the capillary pore, and typically generates larger powder granules as the drop penetrates further.

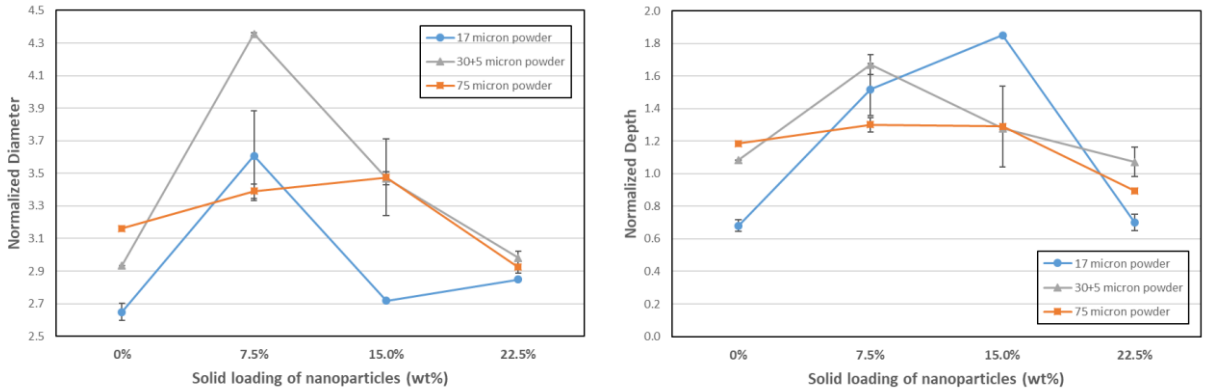

Figure 5.17 Normalized radial diameter and vertical depth of the binder agglomerated powder generated from the binder penetrating powder goniometry

5.4.3.2. Equilibrium binder saturation ratio

The binder penetration driven by capillary action leads to a growth of binder-powder nuclei and reduction of binder moisture level per unit volume (i.e., equilibrium saturation ratio). Therefore, the equilibrium saturation ratio of a binder-powder combination is another metric to describe the binder-powder interaction. The equilibrium saturation ratio (S_e) was estimated by the ratio of binder drop volume (V_{binder} measured by the pendant drop goniometry) to the volume of binder-powder granules (Equation 5.18), and is plotted for each binder-powder combination in Figure 5.18.

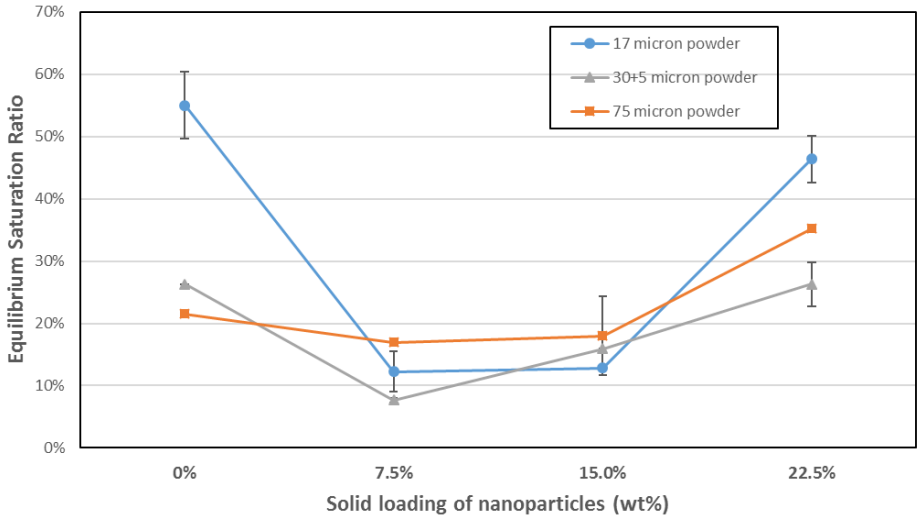

Figure 5.18 The equilibrium binder saturation ratio vs. nanoparticle solid loading for different powders

As the equilibrium saturation ratio is inversely proportional to the binder penetration depth, the trend displayed in equilibrium saturation ratio (Figure 5.18) was opposite to that of penetration depth (Figure 5.17). For the less porous powder bed (17 μm and 30+5 μm powders), the first addition of 7.5 wt% suspended nanoparticles to the polymer binder resulted in lower equilibrium saturation ratio as the binder penetrated deeper driven by the larger capillary number (Figure 5.15). The further increase of solid loading in nanosuspension has led to a higher equilibrium saturation ratio due to the reduced capillary pressure, which is evident in Figure 5.19 where calculated capillary pressure (Equation 5.4) is plotted against measured equilibrium saturation ratio.

When only nanoparticle-polymer suspension is considered (7.5-22.5 wt% solid loading), a capillary-saturation curve can be established (Figure 5.19). The established capillary-saturation curve is similar to the typical trend of capillary-saturation relationship for liquid penetrating powder (Figure 5.7). In the low capillary pressure region, a small reduction of capillary pressure has resulted in a significant increase in equilibrium saturation ratio. The particle-free polymer binder, however, cannot be fitted into the curve established for the particle suspensions.

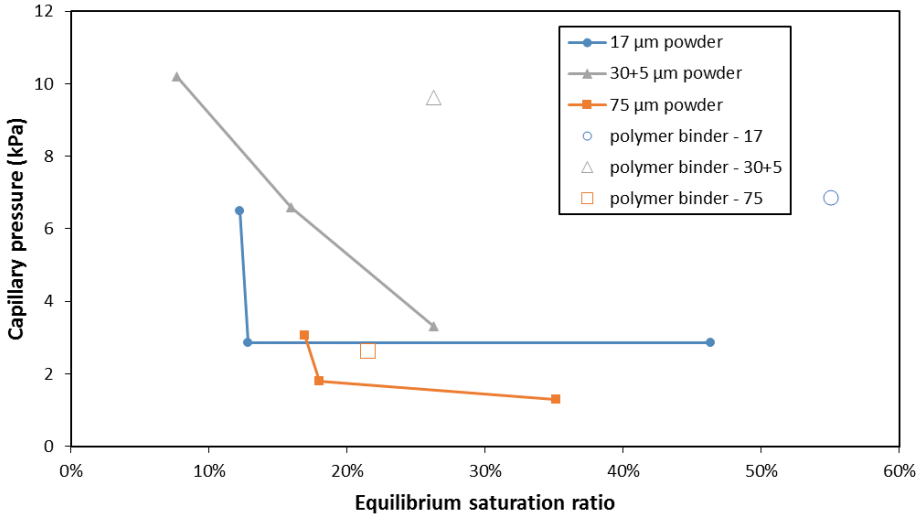

Figure 5.19 The relationship between the capillary pressure and equilibrium binder saturation ratio

5.4.4. Application

Binder-powder compatibility is the pre-requisite of successful printing in binder jetting and it can be used to screen materials. In this work, the compatibility between binder and powder can be described by the dynamic wetting in capillaries. In general, the characteristics of good binder-powder compatibility are reflected in shorter penetration time, smaller capillary dynamic contact angle, and higher capillary pressure.

Binder-powder wettability and associated capillary pressure also has an impact on the selection of printing parameters. Despite the sessile drop used in this study being much larger than ink jetted drops, the powder nucleation mechanisms are the same because both drops are larger than the powder particle size [36]. As a result, it is assumed the primitive size is proportional to the diameter of the binder drop (treating binder drop as spherical-shaped). The primitive dimensions (D_P or H_P) can therefore be estimated by the sessile drop granule dimensions (D_S or H_S) and drop volume of inkjet (V_{inkjet}) and sessile drop (V_S) in Equation 5.19. Table 5.3 uses polymer binder and 15 wt% nanoparticle binder as an example to show how the printing parameter selection is guided using the results in Section 5.4.2.

$$D_P = D_S \times (V_{inkjet}/V_S)^{1/3} \qquad (5.19)$$

Table 5.3 Printing parameter selection for 17 µm powder

	Polymer binder	*15 wt% nanoparticle binder*
Inkjet drop volume, V_{inkjet}	132.8 pL	119.3 pL
Primitive diameter (maximum allowed drop spacing), D_P	167.7 µm	166.1 µm
Primitive height (maximum allowed layer thickness), H_P	43.0 µm	113.0 µm
Binder saturation ratio (*S*) with no primitive stitching	23.3%	8.1%
Binder saturation ratio (*S*) with 1/3 primitive overlaps ($dX=2/3D_P$)	78.8%	27.5%

The inkjet drop volume (V_{inkjet}) is determined by firing a known number of droplets to a substrate on an ExOne 3D printer and measuring the gained weight of the substrate. The binder saturation ratio (*S*) in Table 5.3 (calculated according to Figure 5.20 and Equation 5.20) is related to printing parameters and needs to be distinguished from equilibrium binder saturation ratio (S_e) discussed in Section 5.4.2.3. It can be concluded from the calculation of required binder saturation ratio (*S*) that, *S* needs to be larger than equilibrium binder saturation ratio (S_e) to achieve primitive overlaps that is mandatory for binder jetting.

$$S = \frac{V_{inkjet}}{dXdYdZ(1-\varphi)} \qquad (5.20)$$

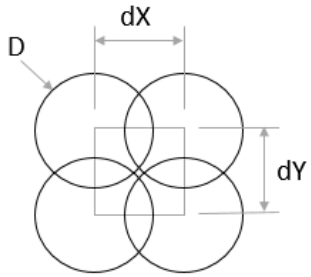

Figure 5.20 Overlapping of printed primitives with a drop spacing of *dX* and *dY*

The larger capillary pressure in 15 wt% nanoparticle binder enables deeper penetration depth, which increases the maximum layer thickness that is allowed to stitch printed layers of primitives and reduces the required binder saturation ratio (*S*) to successfully printed parts. This impact of nanoparticle binder on printing parameters can potentially reduce binder consumption and increase print speed, but the resolution will be lower due to enlarged primitives. While the comparison between two binders is valid, the authors believe the primitive height (*H*) in Table 5.3 is underestimated as this method does not consider the binder drop velocity effect that provides inertia energy for deeper binder penetration.

5.5. Conclusions

This work established an experimental approach based on powder bed sessile drop goniometry and coupled with capillary models for characterizing the binder-powder interaction in binder jetting (Section 5.2). As the sessile drop spreads and penetrates into a powder bed, the interfacial apparent contact angle at powder surface decreases and is plotted against time. The penetration time retrieved from this plot is then used to calculate the dynamic contact angle of binder inside the powder capillary pores, which describes the powder wettability and permeability. The powder bed sessile drop goniometry also produces binder-powder granules that can be directly measured for dimensions once retrieved from the powder. The powder granules created by binder sessile drops mimic the shape of primitives created by inkjet drops in

binder jetting, and therefore can be used to predict primitive dimensions and guide printing parameter selections.

The impact of nanoparticle suspension binder on powder permeability, primitive formation, and printing parameter selections were then investigated using this created tool. The increased viscosity (Figure 5.9) and reduced surface tension (Table 5.2) in the nanoparticle suspensions with higher solid loading prolonged the binder penetration time, especially in less porous powders (Figure 5.13). The relationship between nanoparticle solid loading and powder permeability (dynamic contact angle) manifested a two-section trend. As solid loading increased in the nanoparticle suspensions (7.5-22.5 wt%), the powder permeability was reduced, which was reflected in a larger dynamic contact angle (Figure 5.14), reduced penetration depth (Figure 5.17), larger equilibrium saturation ratio (Figure 5.18), and reduced capillary pressure (Figure 5.19). When the solid loading was increased from 0 wt% (as in pure polymer binder) to 7.5 wt%, an improved powder permeability driven by higher capillary pressure was observed. This is believed to be caused by the enhanced local capillary flow caused by the surface tension gradient around nanoparticles [37], and the reduced local capillary radius around nanoparticles.

This gained understanding can be used to guide printing parameter selection in binder jetting. For example, the primitive size increased when a nanoparticle binder (15 wt%) was used to replace polymer binder (Table 5.3), which lowered the required binder drop spacing and binder saturation ratio for stitching primitives, but reduced the feature resolution in printed parts.

5.6. References

[1] Vaezi, M., and Chua, C. K., 2011, "Effects of layer thickness and binder saturation level parameters on 3D printing process," Int. J. Adv. Manuf. Technol., 53(1–4), pp. 275–284.

[2] Castilho, M., Gouveia, B., Pires, I., Rodrigues, J., and Pereira, M., 2015, "The role of shell/core saturation level on the accuracy and mechanical characteristics of porous calcium phosphate models produced by 3D printing," Rapid Prototyp. J., 21(1), pp. 43–55.

[3] Washburn, E. W., 1921, "The dynamics of capillary flow," Phys. Rev., 17(3), pp. 273–283.

[4] Denesuk, M., Smith, G. L., Zelinski, B. J. J., Kreidl, N. J., and Uhlmann, D. R., 1993, "Capillary penetration of liquid droplets into porous materials," J. Colloid Interface Sci., 158(1), pp. 114–120.

[5] Hapgood, K. P., Litster, J. D., Biggs, S. R., and Howes, T., 2002, "Drop Penetration into Porous Powder Beds," J. Colloid Interface Sci., 253(2), pp. 353–366.

[6] Holman, R. K., Cima, M. J., Uhland, S. A., and Sachs, E., 2002, "Spreading and infiltration of inkjet-printed polymer solution droplets on a porous substrate," J. Colloid Interface Sci., 249(2), pp. 432–440.

[7] Miyanaji, H., Zhang, S., and Yang, L., 2018, "A new physics-based model for equilibrium saturation determination in binder jetting additive manufacturing process," Int. J. Mach. Tools Manuf., 124(September 2017), pp. 1–11.

[8] Cima, M. J., Lauder, A., Khanuja, S., and Sachs, E., 1992, "Microstructural Elements of Components Derived From 3D Printing," International Solid Freeform Fabrication Symposium, pp. 220–227.

[9] Utela, B. R., Storti, D., Anderson, R. L., and Ganter, M., 2010, "Development Process for Custom Three-Dimensional Printing (3DP) Material Systems," J. Manuf. Sci. Eng., 132(1), p. 11008.

[10] Bai, J. G., Creehan, K. D., and Kuhn, H. A., 2007, “Inkjet printable nanosilver suspensions for enhanced sintering quality in rapid manufacturing,” Nanotechnology, 18(18).

[11] Bailey, A., Merriman, A., Elliott, A., and Basti, M., 2016, “Preliminary Testing of Nanoparticle Effectiveness in Binder Jetting Applications,” Int. Solid Free. Fabr. Symp., pp. 1069–1077.

[12] Godlinski, D., and Morvan, S., 2005, “Steel Parts with Tailored Material Gradients by 3D-Printing Using Nano-Particulate Ink,” Mater. Sci. Forum, 492–493, pp. 679–684.

[13] Mueller, S., Llewellin, E. W., and Mader, H. M., 2010, “The rheology of suspensions of solid particles,” Proc. R. Soc. A Math. Phys. Eng. Sci., 466(2116), pp. 1201–1228.

[14] Stickel, J. J., and Powell, R. L., 2005, “Fluid Mechanics and Rheology of Dense Suspensions,” Annu. Rev. Fluid Mech., 37(1), pp. 129–149.

[15] Coussot, P., and Ancey, C., 1999, “Rheophysical classification of concentrated suspensions and granular pastes,” Phys. Rev. E - Stat. Physics, Plasmas, Fluids, Relat. Interdiscip. Top., 59(4), pp. 4445–4457.

[16] Krieger, I. M., and Dougherty, T. J., 1959, "A Mechanism for Non-Newtonian Flow in Suspensions of Rigid Spheres," Trans. Soc. Rheol., 3(1), pp. 137–152.

[17] Schramm, L. L., and Hepler, L. G., 1994, “Surface and interfacial tensions of aqueous dispersions of charged colloidal (clay) particles,” Can. J. Chem., 72, pp. 1915–1920.

[18] Tanvir, S., and Qiao, L., 2012, “Surface tension of nanofluid-type fuels containing suspended nanomaterials,” Nanoscale Res. Lett., 7(1), p. 1.

[19] Murshed, S. M. S., Tan, S. H., and Nguyen, N. T., 2008, “Temperature dependence of interfacial properties and viscosity of nanofluids for droplet-based microfluidics,” J. Phys. D. Appl. Phys., 41(8).

[20] Chen, R. H., Phuoc, T. X., and Martello, D., 2011, “Surface tension of evaporating nanofluid droplets,” Int. J. Heat Mass Transf., 54(11–12), pp. 2459–2466.

[21] Vafaei, S., Purkayastha, A., Jain, A., Ramanath, G., and Borca-Tasciuc, T., 2009, “The effect of nanoparticles on the liquid-gas surface tension of Bi2Te3 nanofluids,” Nanotechnology, 20(18), p. 185702.

[22] Dong, L., and Johnson, D., 2003, “Surface Tension of Charge-Stabilized Colloidal Suspensions at the Water-Air Interface,” Langmuir, 19(24), pp. 10205–10209.

[23] Bredt, J. F., 1995, “Binder stability and powder-binder interaction in three dimensional printing,” Doctoral dissertation, Massachusetts Institute of Technology.

[24] Wolansky, G., and Marmur, A., 1998, “The Actual Contact Angle on a Heterogeneous Rough Surface in Three Dimensions,” Langmuir, 14(18), pp. 5292–5297.

[25] Alghunaim, A., Kirdponpattara, S., and Newby, B. M. Z., 2016, “Techniques for determining contact angle and wettability of powders,” Powder Technol., 287, pp. 201–215.

[26] Middleman, S., 1995, Modeling axisymmetric flows: dynamics of films, jets, and drops, Academic Press.

[27] Rillaerts, E., and Joos, P., “The Dynamic Contact Angle,” Chem. Eng. Sci., 35, pp. 883–887.

[28] Bredt, J. F., Anderson, T., Russell, D. B., Clark, S. L., and DiCologero, M. J., 2006, “Material systems and methods of three-dimensional printing”, United States Patent US 7,795,349 B2

[29] Moseley, W. A., and Dhir, V. K., 1996, “Capillary pressure-saturation relations in porous media including the effect of wettability,” J. Hydrol., 178(1–4), pp. 33–53.

[30] Miyanaji, H., and Yang, L., 2016, “Equilibrium Saturation in Binder Jetting Additive Manufacturing Processes: Theoretical Model Vs. Experimental Observations,” International Solid Freeform Fabrication Symposium, pp. 1945–1959.

[31] Bai, Y., and Williams, C. B., 2017, “Binderless Jetting: Additive Manufacturing of Metal Parts via Jetting Nanoparticles,” Int. Solid Free. Fabr. Symp., pp. 249–260.

[32] Bai, Y., and Williams, C. B., 2015, “An exploration of binder jetting of copper,” Rapid Prototyp. J., 21(2), pp. 177–185.

[33] Derby, B., and Reis, N., 2003, “Inkjet Printing of Highly Loaded Particulate Suspensions,” MRS Bull., 28(11), pp. 815–818.

[34] Bai, Y., Wagner, G., and Williams, C. B., 2017, “Effect of Particle Size Distribution on Powder Packing and Sintering in Binder Jetting Additive Manufacturing of Metals,” J. Manuf. Sci. Eng., 139.

[35] Link, K. C., and Schlünder, E.-U., 1996, “A new method for the characterisation of the wettability of powders,” Chem. Eng. Technol., 19, pp. 432–437.

[36] Hapgood, K. P., Farber, L., and Michaels, J. N., 2009, “Agglomeration of hydrophobic powders via solid spreading nucleation,” Powder Technol., 188(3), pp. 248–254.

[37] Casson, K., and Johnson, D., 2001, “Surface-tension-driven flow due to the adsorption and desorption of colloidal particles,” J. Colloid Interface Sci., 242(2), pp. 279–283.

6. Additive Manufacturing of Metal Parts from Jetting a Particle-free Metal Ink as Binder Precursor for Binder Jetting

6.1. Introduction

6.1.1. Polymer binder vs. metal binder

The selection of binder material for binder jetting is critical as it determines the success of creating green parts with satisfactory green strength and affects the final properties of the sintered parts (e.g., sintered density and sintering shrinkage). Different types of binders have been used in binder jetting, including various solvents, colloids, and organic based inks [1].

In modern commercial metal binder jetting systems, solvent-based organic binders that contain thermosetting polymers are commonly used to print green parts [2]. As shown in Figure 6.1, after jetting binder at each layer, an overhead heater removes the solvent (drying). Once the part is printed, the entire powder bed can be placed in a curing oven to fully set and crosslinks the jetted polymer (curing). While the curing of binder could be integrated into a drying process with longer heating time and higher temperature, it is typically chosen to cure the part separately after printing for economic reasons. The cured polymer binder is then burned at an elevated temperature through polymer pyrolysis when the printed part is sintered.

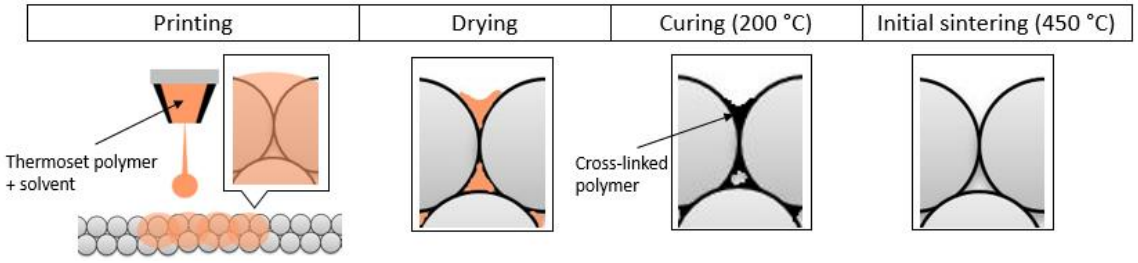

Figure 6.1 Jetting an organic adhesive as the binder

While polymer binders have demonstrated a wide success and compatibility with many metal systems, their use in binder jetting can add complexity to the sintering process and adversely affect the final product performance metrics:

(i) the need to debind polymer binders typically require refined sintering profile and slow heating ramp to facilitate polymer pyrolysis and degassing, and could lead to debinding-related defects;
(ii) the green part can lose structural integrity (i.e., warping, creep) during sintering if the onset sintering temperature of powders is higher than the binder burn-out temperature;
(iii) the pyrolysis of polymer binder can leave residual ash, which affects the purity (and thus mechanical, optical, electrical/thermal properties) of the final part.

To circumvent these limitations, the authors propose using metal nanoparticles ink as a binder to replace organic adhesives. Many metal nanoparticles manifest size-dependent melting behaviors and lower melting/sintering temperatures compared with the bulk materials [3]. For example, copper nanoparticles can sinter and neck within temperature ranges (150-300 °C) that are significantly reduced from sintering temperature for micron-sized powders (around 1000 °C) [4]. When nanoparticles are jetted as a binder in binder jetting, this unique sintering temperature reduction feature of nanoparticles can enable the selective cohesion of the powder bed when heat is supplied at each layer to sinter jetted nanoparticles while not affecting the powder in unprinted regions.

6.1.2. Review of metal inks used in binder jetting

Metal inks have been explored in prior research for fabricating metal artifacts to enhance material properties. Metal-based binders have existed in the forms of either metal particle suspensions or metal salt solutions, and used as a standalone ingredient or mixed with other adhesives.

6.1.2.1. Particle suspension metal inks

Particles suspensions can be used together with polymer binders to enhance material properties [5–7]. For example, silver nanoparticles were dispersed into suspensions and used together with a water-based organic binder to print micron-sized silver powders, which achieved higher sintered density (88.9%), reduced shrinkage and warpage compared to just using the polymer binder.

Jetted particulate suspensions can be also used without the presence of other adhesives. Yoo *et al.* jetted carbonyl iron (1.7 μm) suspended into water to stainless steel powders (60 μm) followed by firing the entire powder bed in forming gas at 600-700 °C, under which temperature the interstitial carbonyl iron particles sintered without sintering the base powder, generating weak but retrievable printed parts [8]. Similarly, Hadjiloucas *et al.* used silver suspensions as the binder for printing molybdenum powders [9]. The printed interstitial silver particles melted and bonded the base powder particles after heating at 1000 °C; at this temperature, the base powder remained loose and ensured part retrieval from the powder bed.

In prior work, the authors have successfully used nanoparticles as a binder to print micron-sized powders in a single material system (e.g. copper) [10]. A copper nanoparticle suspension was jetted into copper powder as a binder without polymer binders. Green parts with satisfactory integrity (flexural strength of 1.1 MPa) were produced by sintering the jetted nanoparticles after subjecting the printed powder bed to heating (200-250 °C). The printing process schematic for nanoparticle binders is depicted in Figure 6.2. Compared to the sacrificial polymer binder in Figure 6.1, the nanoparticle binder is permanent as it remains after sintering and becomes part of the final product.

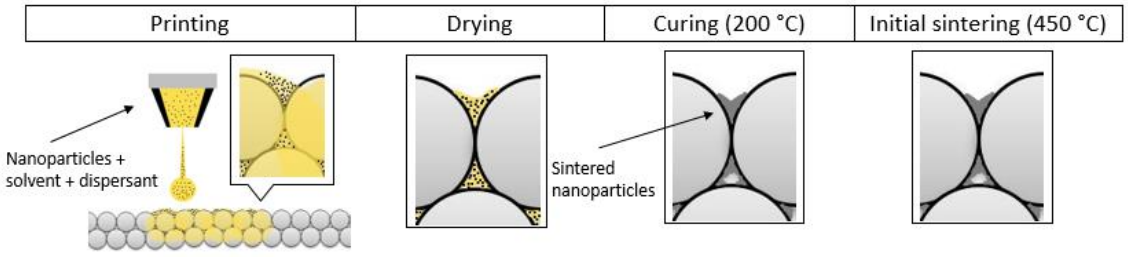

Figure 6.2 Jetting a nanoparticle suspension as the binder

Despite the vast success of using particle suspensions demonstrated in the literature, the overall effectiveness of using particle suspension as a metal binder is limited by (i) the difficulty to disperse particles and requirement of capping materials in the suspension, and (ii) possible ink sedimentation and printhead nozzle clogging during inkjet printing.

6.1.2.2. Metal salt inks

Due to the challenges in inkjet printing particle suspensions, researchers have looked to use metal salt as an alternative metal ink. Metal salts dissolved in solvents can be jetted, and then precipitate metal solids through decomposition or reduction upon heating. Various inorganic metal salt solutions have existed for the use as a precursor ink in conductive pattern printing (e.g., copper nitrate hydroxide [11] and copper sulfate [12]). Compared to particle suspension binders, metal salt ink is particle-free and therefore is more suitable for inkjet printing applications, such as (i) reducing the risk of clogging inkjet

printhead, (ii) preventing ink sedimentation and increasing ink shelf life, and (iii) alleviating surface oxidation in metal nanoparticles during storage.

Metal salt has been used with or without polymer binder for printing metals in binder jetting. Liu *et al.* used metals salts as precursor inks to strengthen printed metal parts [13]. Copper or nickel acetate saturated solutions were deposited into stainless steel powders, after firing at a temperature below the powder sintering temperature (450 °C), metals formed and sintered to the metal powder particles and to one another in the powder interstices. Yoo *et al.* used silver nitrate as a binder for steel powders [8]. Silver nitrate reduced to an adherent silver film in the powder neck region and produced pellets with satisfactory strength after firing in forming gas at 400 °C, at which temperature the steel powder did not sinter. Hadjiloucas *et al.* used copper and silver salt solutions as binders for molybdenum powders [9]. The molybdenum powder allows an ultra-high temperature (>1000 °C) to cure the metal salt binder without sintering the powder bed. The printed parts were heated above the melting temperature of the elemental metals, where the metal salts decomposed, melted and formed a necking between powder particles.

While metal salt inks circumvent the dispersion and jettability issues in jetting particle suspensions, its use as a binding agent in binder jetting is limited in that (i) the metal content is limited by the metal salt solubility in saturated solutions, and (ii) the metal salt decomposition or reduction typically requires ultra-high temperature and reducing atmosphere. For example, copper acetate water solution is difficult to be used as a binder for printing copper, as the metal content cannot exceed 2.3 wt% due to solubility limits, and the required ink metallization temperature (300 °C in air [14]) exceeds the initial sintering temperature of micron-sized copper powders.

6.1.2.3. Metal-Organic-Decomposition (MOD) inks

Metal-Organic-Decomposition (MOD) ink is a metal ink that has been widely used for printed electronics [15,16]. MOD ink contains an organometallic compound formed by introducing ligands (complexing agents) to metal salts. Compared to metal salt inks, the introduction of complexing agents (e.g., amines) can (i) lower the required metallization temperature, (ii) control the precipitated particle size, or (iii) improve solubility of the metal-organic compounds in solvents. This makes MOD ink more suitable for printing metal patterns as a precursor ink on flexible polymer substrates that cannot withstand high curing temperature [17–19].

This unique feature of MOD ink also creates an opportunity for its use as a precursor to the nanoparticle binder for binder jetting of metals. After applying a moderate heat to the jetted ink without fusing the surrounding powder, the MOD ink is capable of depositing nanoparticles with controlled growth, which can be sintered to form a bond for the powder. MOD ink is similar to nanosuspension in a way that nanoparticles are deposited to the powder necking and interstices after drying (Figure 6.3). However, unlike nanoparticle suspension, MOD ink is particle-free during printing, and therefore has a potential to alleviate the challenges encountered in particle inks (e.g. nozzle clog, sedimentation, etc.)

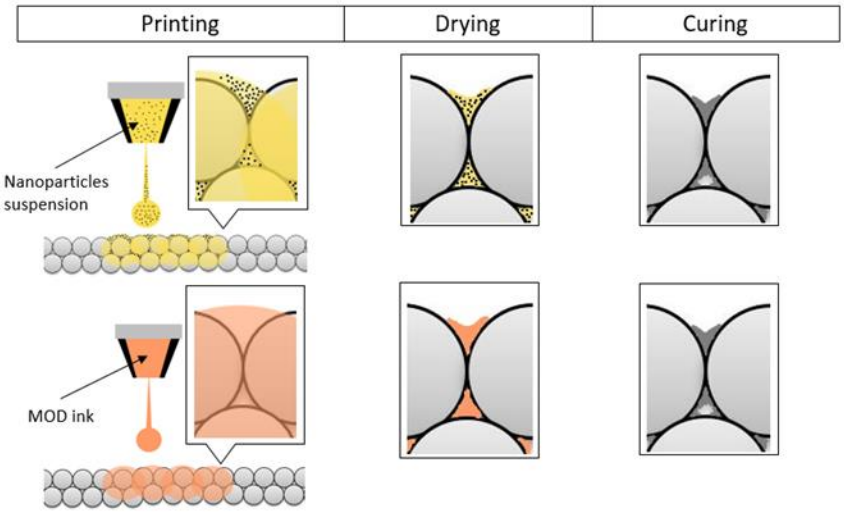

Figure 6.3 Comparison between jetting a nanoparticle suspension (with particles) and MOD ink (particle-free) as the binder

6.1.3. Roadmap

The goals of this article is to (i) demonstrate the concept of using Metal-Organic-Decomposition (MOD) ink as a particle-free metal binder in binder jetting, and (ii) experimentally explore of its effects on the printed part properties. The use of MOD ink is validated in the context of binder jetting of copper, based on an established manufacturing process for copper from prior work [20,21].

Section 6.2 provides the details on the material system, printing process, and experimental procedures; Section 6.3 discusses the experimental outcomes from using copper MOD inks in binder jetting of copper.

6.2. Experimental methods

To experimentally validate the use of MOD ink as a nanoparticle binder, green parts were printed on a binder jetting platform using copper powder and synthesized copper MOD inks and then sintered. To study the MOD binder's impact on green and sintered part properties, binder saturation ratio and green part curing temperatures were varied to study their effects on the green part structural integrity and sintered part density. Parts were also printed with similar conditions using conventional polymer binders to establish a datum for comparison.

6.2.1. Ink formulation and synthesis

The formulation and synthesis of copper MOD inks is well established in the electronic printing industry. Among copper carboxylates (e.g., copper glycolate [19], oxalate [22], lactate and oleate [23]) that can decompose to form copper when annealed at elevated temperatures, short carbon chain copper carboxylates (e.g., copper formate and acetate) are typically used in order to increase the metal content of the inks. Amines are the commonly used complexing agents for copper MOD inks (e.g. isopropanolamine [24], cyclohexylamine [25], and aminediols [26], etc.). In order to generate copper nanoparticles, octylamine can be used to control particle growth, and 2-amino- 2-methyl-1-propanol (AMP) can be used to improve solubility in organic solvents and lower decomposition temperature [18]. In a similar study, copper formate and AMP combination was deemed as most ideal to print conductive patterns compared with other studied ligands [17].

Based on the reviewed literature, in this study the authors choose copper(II) formate as the precursor and 2-amino- 2-methyl-1-propanol (AMP) and octalamin as the ligand, in order to make the ink

dissolvable in organic solvents and achieve (i) high copper loading, (ii) low decomposition temperature, and (iii) minimal organic residual. Copper nanoparticles are generated through the decomposition of copper formate which follows [18]:

$$Cu(HCOO)_2 \rightarrow Cu + 2CO_2 + H_2$$

To synthesize the copper organometallic compound, 42 g of AMP and 64 g of octalamin as complexing agents was added to 90 g of methyl alcohol and magnetically stirred for 30 min. Then, 112 g of copper(II) formate tetrahydrate powder was added to the mixture so that the molar ratio of copper(II) formate to the complexing agents was 1:2. This solution was stirred for 60 minutes to ensure complete formation of the copper organometallic complex, and dried in a vacuum oven for 8 hours to remove the solvent.

6.2.2. Ink rheology and metallization

The final MOD ink was prepared by diluting the organometallic compound with 2-methoxyethanol. An ink rheology that is suitable for inkjet printing was obtained by varying the concentrations of the organometallic compound. 2-methoxyethanol is the main solvent for ExOne's solvent-based polymer binder, and it is used in the MOD inks for a more predictable printing process. The viscosity and surface tension of copper MOD ink was measured by a TA Instrument hybrid rheometer and sessile drop tensiometer.

In order to verify the metallization of synthesized MOD ink and observe the precipitated nanoparticles, silicon wafer substrates were coated with MOD ink films and heated with various temperatures that are typically used for curing printed green parts, and characterized by SEM. The metal content of copper MOD inks was measured by Thermogravimetric Analysis (TGA) to quantify the nanoparticle weight percentage in the MOD binder that is used towards constructing the final sintered parts.

6.2.3. Printing process and green part properties

The green parts were printed on an ExOne R2 3D printer. A high purity (>99%) gas atomized copper powder with 17 μm median particle size was used for printing. A standard, ExOne solvent-based polymeric binder was used to print parts as a control group in this study. The printing parameters used to print the green parts were: 10 mm/s powder spreading speed, 1.3 feed-to-build powder recoating ratio, and 80 μm layer thickness.

Interlayer drying during printing and post-print curing is typically required for polymeric binder to dry the solvent crosslink polymers. When printing polymer binder, the powder bed temperature controller was maintained at 80 °C and the overhead heater was set at 200 °C with a scanning speed of 1 mm/s for each printed layer. When printing MOD inks, the suitable drying and curing temperature was determined by studying the particle formation in the ink metallization process. An infrared thermometer was used to monitor the actual powder bed temperature during printing. After printing, the green parts printed by both binders were cured in a controlled atmosphere oven. Curing temperature was varied to study its effect on the green part strength.

The binder saturation ratio for each binder (copper MOD ink and polymeric binder) was determined by the measured powder bed density and recorded binder drop volume. The measured drop volume for copper MOD ink and polymeric binder was 50 pL and 96 pL, respectively.

Several 18×6×3 mm test coupons were printed to evaluate print quality, strength and density of the printed green parts. In the binder jetting metal printing process, sufficient green strength of the printed

parts is required for part removal and depowdering via compressed air. Therefore, several parts were printed for each binder saturation ratio, and the green strength was evaluated by assessing part damage after depowdering using compressed air.

6.2.4. Sintering and sintered part properties

The printed, cured, and depowdered green parts were then sintered in a pure hydrogen atmosphere for copper oxide reduction, with an isotherm at 450 °C for 30 min to facilitate debinding of polymeric binders [20]. While no polymer pyrolysis is needed for MOD ink printed parts, the debinding isotherm was still incorporated into the heating schedule to ensure parts printed with different binders receive same heat treatment for comparing sintered properties. With a heating ramp of 5 °C/min, printed samples were heated to different peak temperatures (1025-1075 °C) and maintained for 2 hours.

Three parts were printed for each binder and binder saturation ratio to evaluate sintered part properties at each sintering condition. Sintered density and porosity was measured by Archimedes immersion method [27] and metallographic methods. The sintered part surface morphology and composition was characterized by a LEO (Zeiss) 1550 field-emission SEM.

6.3. Results and discussion

6.3.1. Ink rheology

Figure 6.4 shows the measured viscosity of MOD inks with different concentrations of organometallic compound in solvent (50 wt% and 75 wt%). While being near Newtonian fluid, the MOD ink's viscosity clearly depends on the weight percent of organometallics in the solvent.

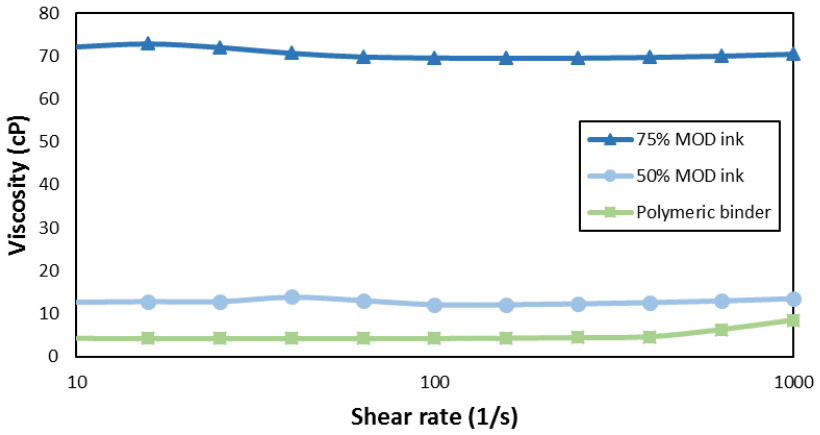

Figure 6.4 Viscosity of the copper MOD ink in the solvent with different concentrations, compared to the polymeric binder

In inkjet printing, jettability is dictated by the Ohnesorge number (*Oh*), a function of an ink's viscosity (μ), density (ρ), surface tension (γ), and nozzle diameter (Equation 6.1). Specifically, if the inverse of the *Oh* of an ink has a value between 1 and 10, then the ink is likely to be successfully jetted on most commercial Drop-on-Demand (DOD) platforms [28].

$$Oh = \frac{\sqrt{We}}{Re} = \frac{\mu}{\sqrt{\rho\gamma D}} \qquad \text{(Equation 6.1)}$$

Table 6.1 summarizes the rheology information and calculated Ohnesorge number for the MOD ink and polymer binder, showing only 50% MOD ink is predicted to be able to inkjet thorough a 55 µm printhead nozzle. The surface tension of 50 wt% MOD compound dispersed in the solvent was measured by the pendent drop in Figure 6.5.

Table 6.1 Summary of binder rheology and jettability

Binder type	*Viscosity (cps)*	*Surface tension (mN/m)*	*Density (g/ml)*	*Nozzle diameter (µm)*	*1/Oh*
50 wt% MOD ink	12	29.4	0.90	55	3.2
Polymer binder	4.5	31.2	0.99	55	9.2

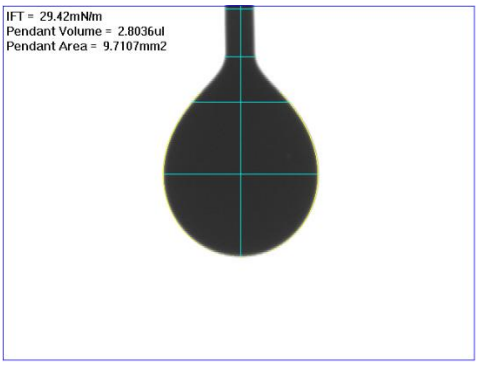

Figure 6.5 Pendent drop of 50% MOD ink, with a calculated surface tension of 29.42 mN/m

6.3.2. Ink metallization

Metallization of MOD ink was confirmed with electronic microscopy, where copper particles have formed upon heating the copper MOD ink at 250 °C (Figure 6.6). In both reducing and inert atmosphere, the precipitated particles from ink metallization is a mixture of larger particles (over 100 nm) and nanoparticles (less than 100 nm). When heated in air atmosphere, large micron-sized particles formed instead, with more oxidation on particle surface.

The successful use of MOD ink as a nanoparticle binder relies on the controlled particle growth and development of oxidation when the ink is metallized. As a result, the heating of jetted MOD inks in air with elevated temperature and prolonged time should be avoided.

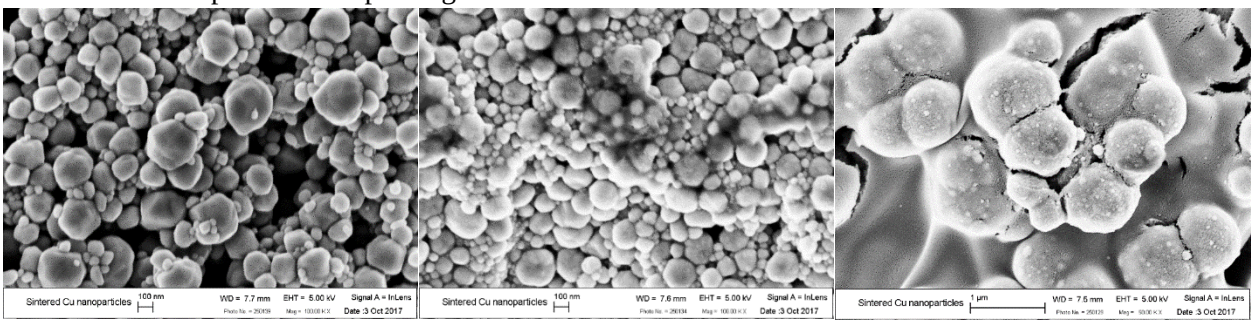

Figure 6.6 SEM images of copper MOD ink, heated at 250 °C for 3 hours in hydrogen (left, 100kx), nitrogen (middle, 100kx), and air (right, 50kx), with copper weight percent measured by EDS of 98.2%, 93.9% and 77.4%

TGA was used to study the ink metallization kinetics and the metal loading of the synthesized MOD ink. As revealed in Figure 6.7, the copper MOD ink was heated at 5 °C/min in nitrogen, and finished decomposition by reaching to the final composition at 150 °C, in a time span of approximately 25 minutes. In this MOD ink, 7.4% of the total binder content turned to copper particles that can be utilized towards building the final sintered parts; verses in polymer binder, approximately 9% percent polymer was left after solvent removal but later pyrolyzed, leaving 0.7% carbon residual that was considered as an impurity.

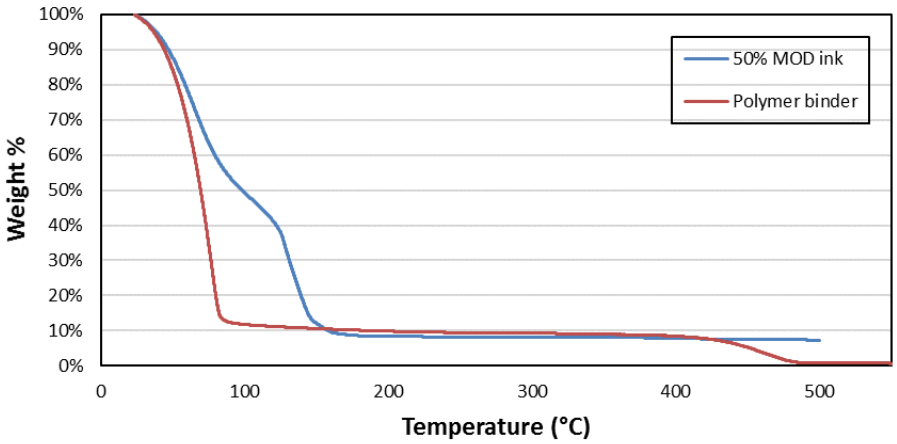

Figure 6.7 Thermographic analysis of copper MOD in (50 wt% compound in solvent) and polymer binder

6.3.3. Green part properties

The ink metallization process studied in Section 6.3.2 provided a guidance for the development of appropriate drying and curing conditions for printing MOD inks. To ensure the successful printing MOD ink as a nanoparticle binder, the jetted ink needs to metallize and precipitate particles in an inert or reducing atmosphere. As a result, the heating conditions for drying and curing MOD were set in a way that (i) solvent can be dried with limited ink metallization when heating printed layers in the air, and (ii) nanoparticles can completely precipitate from the ink and then sintered when curing the printed parts in a controlled atmosphere.

An overhead heater (set at 200 °C) with scanning speed of 5 mm/s was used to dry the jetted MOD inks. When the heater scanned over the copper powder bed, the powder directly under the heater reached to a temperature of 160 °C for a few seconds, and then rapidly drops down to a temperature below 100 °C after the heater moves away. While the peak powder temperature has reached the ink decomposition temperature (Figure 6.7), the fast scanning speed did not allow sufficient time for ink metallization, thus preventing the unwanted particle growth and oxidation when heating MOD ink in the air (Figure 6.6).

Figure 6.8 shows the interparticular bonding within the green parts from drying jetted MOD inks (without any post-print curing). The drying condition did not allow a completed ink metallization; as a result, the jetted ink mainly remained as not decomposed organometallics. Despite no nanoparticle sintering is evident as this stage (after drying without post-print curing), the dried MOD ink was able to provide enough bonding strength to ensure printed part removal from the powder bed (Figure 6.9).

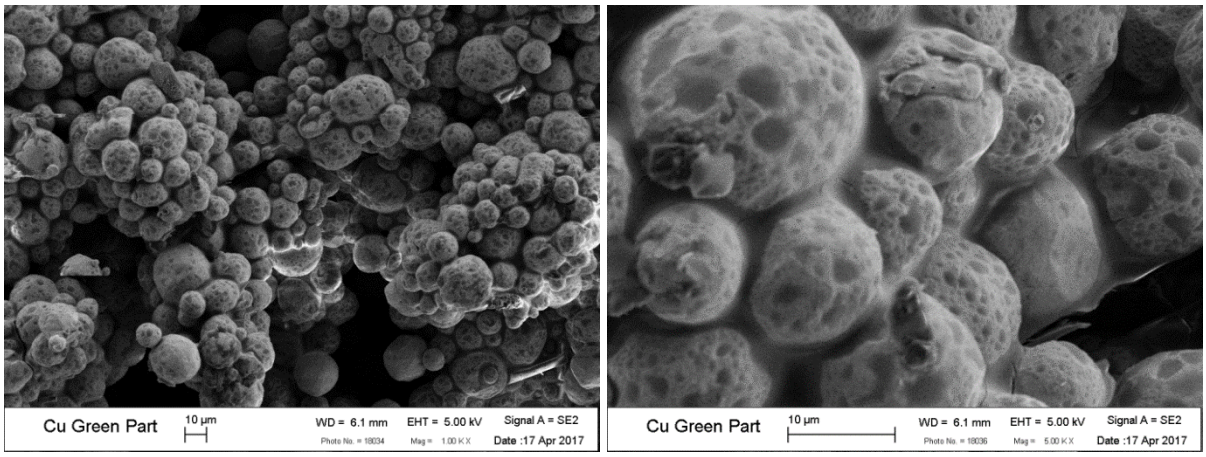

Figure 6.8 SEM images of the green parts printed with MOD ink (150% binder saturation, without post-print curing): 1kx (left) and 5kx (right) magnification rate

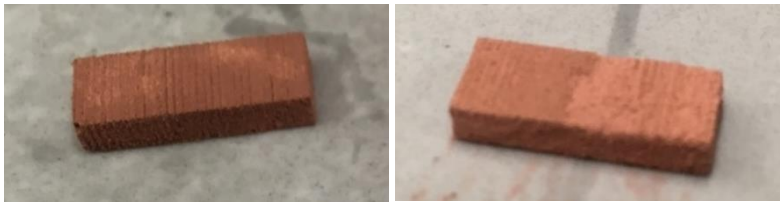

(a) (b)

Figure 6.9 MOD printed part (18×6×3 mm) with (a) 150% saturation ratio and (b) 75% saturation ratio, after retrieving from the powder bed without post-print curing

After retrieval from the powder bed, the MOD ink printed parts were cured in a controlled-atmosphere oven to complete the decomposition of MOD ink and formation of nanoparticles. The curing temperature was varied from 200 to 250 °C, in order to (i) ensure the sintering of precipitated nanoparticles, and (ii) study the effects of curing temperature on green part integrity. A reducing atmosphere was used facilitate nanoparticle sintering by reducing surface oxidation. After curing, sintered nanoparticles can be found at the necking of powder particles (Figure 6.10).

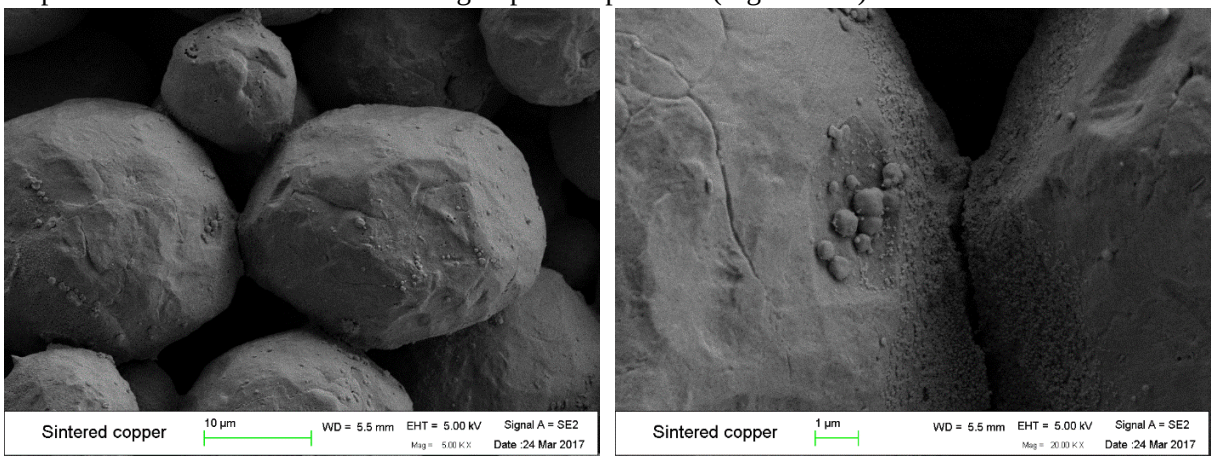

Figure 6.10 SEM images of the powder particle bonding formed by sintered copper nanoparticles (150% saturation): 5kx (left) and 20kx (right) magnification rate

To evaluate the integrity of printed green part after depowdereing, the cured green parts were subjected to a compressed air stream at the surface (Table 6.2). Compared to curing at 200 °C, curing

with 250 °C produced better green strength, especially in 150% saturation ratio printed parts. While satisfactory printed part strength can be achieved with sufficient binder saturation and curing condition, it is noted that, overall, the MOD binder printed green part is less strong than the polymer binder counterparts.

Table 6.2 Before and after depowdering comparison of the green parts cured at different temperatures for 1 hour in hydrogen

	Cured parts before depowdering	*200 °C cured parts after depowder with 20 psi compressed air*	*250 °C cured parts after depowder with 40 psi compressed air*
MOD ink (75% saturation)			
MOD ink (150% saturation)			
Polymeric binder (150% saturation)			

The green density of MOD ink and polymer binder printed parts was measured prior to post-print curing (Figure 6.11). When printed with same saturation ratio (150%), MOD ink printed parts have a similar green density with polymeric binder printed parts, corresponding to the binder residual percentage measured by TGA in Figure 6.7 (approximately 7% and 9% for MOD ink and polymer binder).

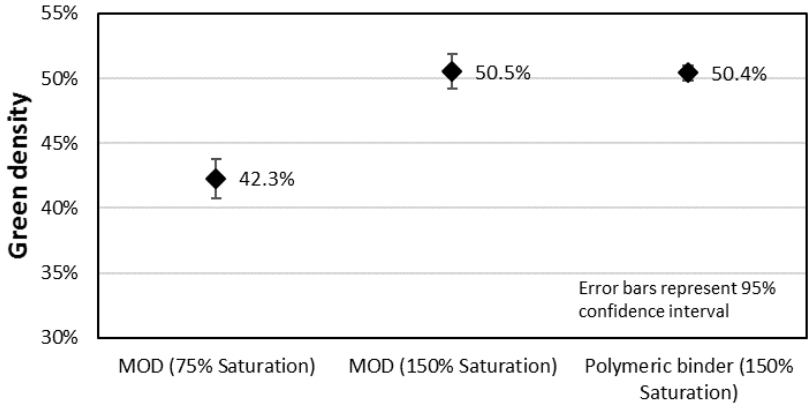

Figure 6.11 Green density of MOD ink printed and polymeric binder printed parts

6.3.4. Sintered part properties

6.3.4.1. Sintered density and shrinkage

The polished cross-sections of sintered MOD ink printed parts have shown a unique pore distribution, where large pores are concentrated near surface and the core section is relatively pore-free (Figure 6.12). For further porosity distribution analysis, Figure 6.12 was converted to black and white images as a binary representation of the microscopic images, where dark regions represent occurrence of the porosity. In Figure 6.13, the distribution of large and small pore is studied separately for MOD ink and polymer binder printed parts. A pixel number of 10 is used to differentiate small and large pores. A map of pore occurrence intensity is created for large and small pores.

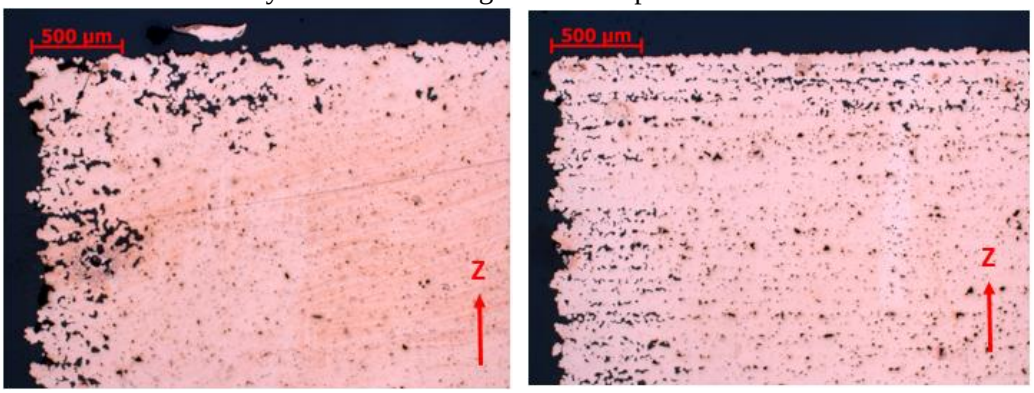

(a) (b)

Figure 6.12 Optical microscopic images of the sectioned and polished sintered parts, printed by (a) MOD ink and (b) polymeric binder, using 150% binder saturation ratio

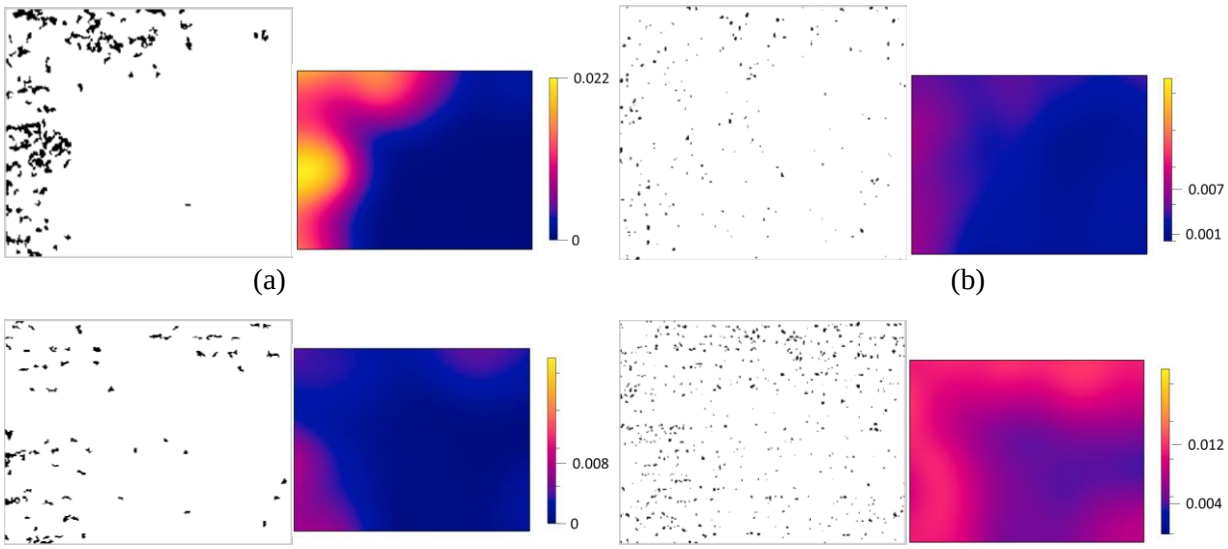

(a) (b)

(c) (d)

Figure 6.13 Porosity distribution analysis by separating large and small pores from Figure 6.12: (a) large pores in MOD ink parts, (b) small pores in MOD ink parts, (c) large pores in polymer binder parts, and (d) small pores in polymer binder parts

In binder jetting printed parts, small pores typically represent the inherent inter-particle spacing, while large pores are more likely caused by factors including powder packing irregularities and powder loss due to missed binder jets. As seen in Figure 6.13, both MOD ink and polymer binder printed parts

have a porous shell composed of large pores and inner section with small pores. However, the porosity in MOD ink printed parts is mainly contributed by the large pores, while small pores are more dominant in polymer binder printed parts (Figure 6.14 and 6.15). When only the core section is compared, the MOD ink printed parts have significantly less porosity, as a result of the densifying effects from depositing extra metal contents to the powder bed. However, the overall porosity in MOD ink printed parts is raised by the porous shell, which is attributed to the loss of powder during depowdering due to insufficient green part strength.

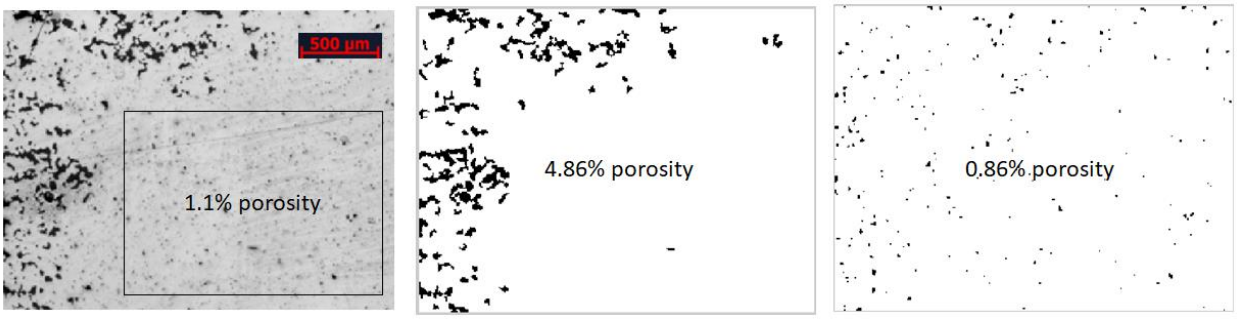

Figure 6.14 Porosity measurement (by optical pixel counting) for MOD ink printed part (Figure 6.12): core section only (1.1%), large pores (4.86%), and small pores (0.86%)

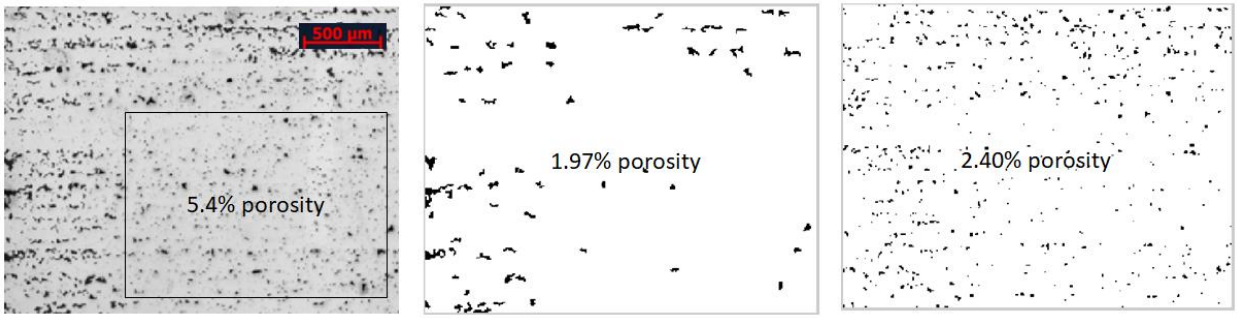

Figure 6.15 Porosity measurement (by optical pixel counting) for polymer binder printed part (Figure 6.12): core section only (5.4%), large pores (1.97%), and small pores (2.40%)

This unique pore distribution of MOD ink printed parts is also reflected in the measured sintered density by Archimedes' method with oil impregnation (Figure 6.16). When a porous sintered part is oil impregnated which seals surface pores, the envelope density of sintered part is measured which reflects the actual part density of both core and shell section. While the overall sintered density of MOD ink printed parts is lower than that of polymer binder printed parts (Figure 6.16), the core section in MOD ink printed parts is denser (Figure 6.14 and 6.15).

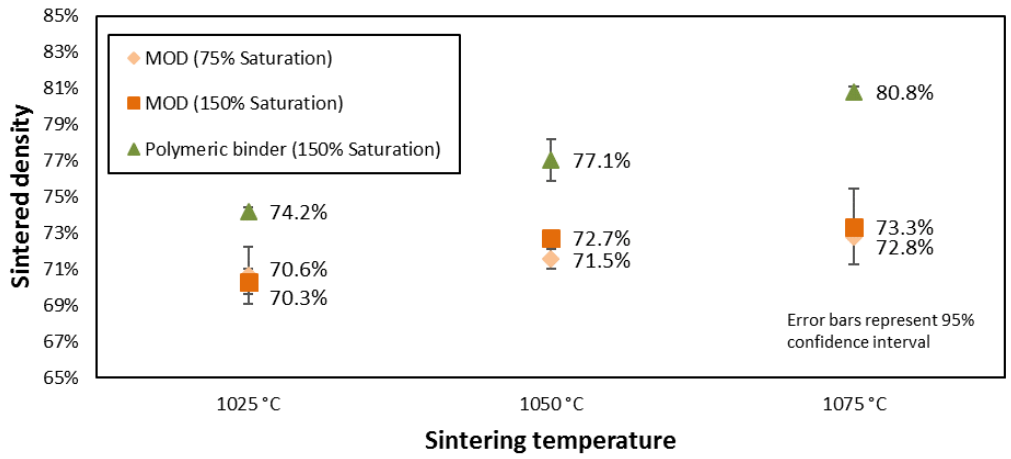

Figure 6.16 Sintered density measured with oil impregnation

Figure 6.17 compares part shrinkage at three different sintering temperatures for MOD ink and polymer binder printed parts. In MOD ink printed parts, the result reveals that higher amount of nanoparticles in 150% binder saturated parts reduced the overall shrinkage compared to the lower saturation parts. This can be attributed to the improved green density in 150% saturated MOD ink parts (Figure 6.11).

It is also noticed that the shrinkage and densification in sintered MOD ink printed parts is less dependent on the peak sintering temperature, compared to the polymer printed parts (Figure 6.16 and 6.17).

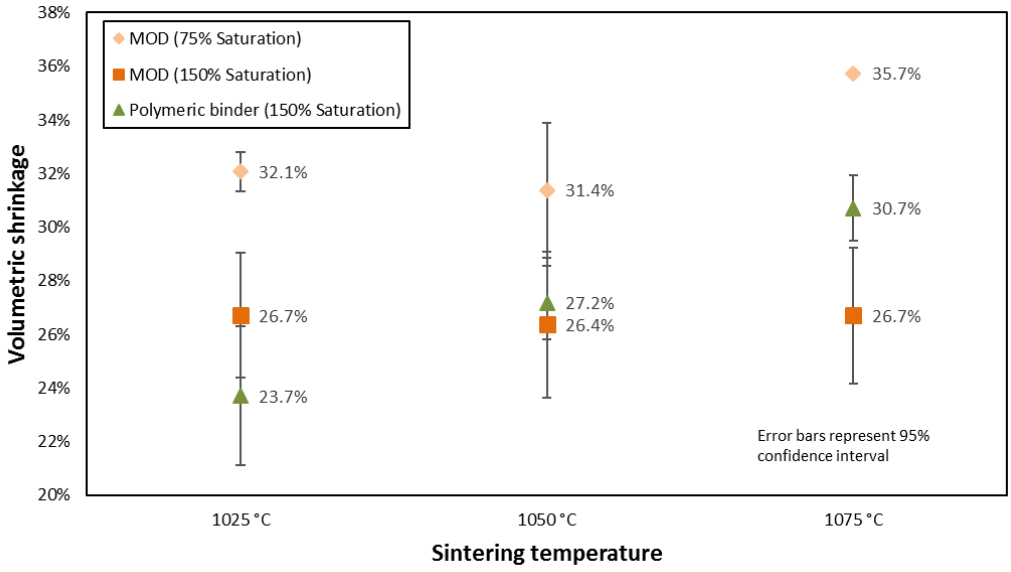

Figure 6.17 Volumetric shrinkage of the sintered part

Density (or porosity) in sintered artifacts made in binder jetting is influenced by many factors. Previous study in binder jetting of copper has shown that sintered density can be affected by printing and sintering conditions [20], powder particle size [29], and post-processing [30]. The results discussed in this work also show that sintered density and pore distribution can be affected by the binder compositions and green part structural integrity and strength.

6.3.4.2. Surface morphology

The use of copper MOD ink also produces a different part surface morphology than traditional polymeric binders. In polymer binder printed parts, a trench-like surface composed of a network of closely packed powder granules is formed as a result of polymeric binder penetrating and rearranging powder particles (Figure 6.18a). In comparison, the printing of MOD inks produces a relatively more uniform surface (Figure 6.18b). This is because of the smaller *Oh* number of MOD ink (Table 6.1) represents less kinetic energy and surface tension in the binder to overcome its viscosity when penetrating powder and rearranging particles. The insufficiently saturated MOD ink part (Figure 6.18c) suffered from low green part strength and powder loss, thus shows more occurrence of surface damage.

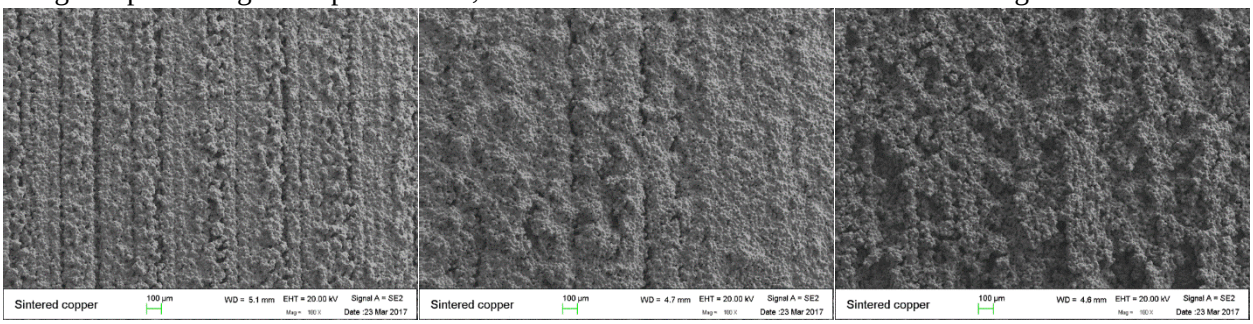

(a) (b) (c)

Figure 6.18 SEM images (100x magnification) of sintered part surface (sintered at 1075 °C), for surface morphology comparison between parts printed by (a) polymeric binder, (b) 150% saturation MOD ink, and (c) 75% saturation MOD ink

6.4. Conclusions

This work demonstrates that Metal-Organic-Decomposition (MOD) ink can be used as a precursor to the nanoparticle binder for binder jetting of metals, by initiating binding between metal powders through sintering the precipitated nanoparticles from jetted ink. As a particle free ink, MOD ink is more cost-effective, and more suitable for inkjet printing as it can potentially alleviate the sedimentation, particle oxidation, and nozzle clog issues found in particle suspensions.

This concept is validated through experimentation in the context of binder jetting of copper. Copper organometallic complex was synthesized with a shown capability of producing copper nanoparticles upon heating (Figure 6.6). A metal content of 7.4 wt% of was achieved (Figure 6.7) as a result of mixing the synthesized organometallic complex with a solvent to maintain ink jettability (Figure 6.4).

Using a similar print setting in printing polymeric binders, the inkjet printed MOD ink was dried between layers by an overhead heater to remove the solvent; the printed parts went through post-printing curing in a reducing atmosphere to fully precipitate and sinter nanoparticles from the jetted and dried organometallic complex, providing a bonding strength to the powder. While the green part produced from MOD ink is less strong compared to the conventionally printed polymeric binder counterparts (Table 6.2), it can maintain a structural integrity after depowdering with compressed air (using 150% binder saturation ratio).

The sintered copper parts printed by copper MOD ink have generated a dense core section that has less porosity than polymer binder parts (Figure 6.12). However, a porous outer shell composed of large pores is formed around the dense core in MOD ink printed parts, which has led to lower sintered density compared to the polymer binder counterparts (Figure 6.16). The porous shell is mainly caused by the powder loss due to weak powder bonding at surface in MOD ink printed parts.

In conclusion, copper MOD ink has been successfully used as a binding agent to print copper parts. Future work may focus on improving material properties thorough developing a higher metal loading ink, as well as expanding the presented concept into more materials.

6.5. References

[1] Utela, B. R., Storti, D., Anderson, R. L., and Ganter, M., 2010, "Development Process for Custom Three-Dimensional Printing (3DP) Material Systems," J. Manuf. Sci. Eng., 132(1), p. 11008.

[2] Jianxin, L., and Kuhn, H. A., 2006, "Materials Development for ProMetal," Mater. Sci. Technol., 66(3), pp. 911–917.

[3] Asoro, M., Damiano, J., and Ferreira, P., 2009, "Size Effects on the Melting Temperature of Silver Nanoparticles: In-Situ TEM Observations," Microsc. Microanal., 15(S2), p. 706.

[4] Yu, E.-K., Piao, L., and Kim, S.-H., 2011, "Sintering Behavior of Copper Nanoparticles," Bull. Korean Chem. Soc., 32(11), pp. 4099–4102.

[5] Bai, J. G., Creehan, K. D., and Kuhn, H. A., 2007, "Inkjet printable nanosilver suspensions for enhanced sintering quality in rapid manufacturing," Nanotechnology, 18(18).

[6] Godlinski, D., Petzoldt, F., and Morvan, S., 2004, "Tailored Functional Gradients by 3D-Printing using Metal Powder and Nano-particulate Inks," Euro PM2004.

[7] Bailey, A., Merriman, A., Elliott, A., and Basti, M., 2016, "Preliminary Testing of Nanoparticle Effectiveness in Binder Jetting Applications," 27th Annu. Int. Solid Free. Fabr. Symp., pp. 1069–1077.

[8] Yoo, H. J., 1995, "Reactive binders for metal parts produced by Three Dimensional Printing", Doctoral dissertation, Massachusetts Institute of Technology.

[9] Hadjiloucas, C., 1997, "Low Shrinkage Metal Skeletons by Three Dimensional Printing," Doctoral dissertation, Massachusetts Institute of Technology.

[10] Bai, Y., and Williams, C. B., 2017, "Binderless Jetting: Additive Manufacturing of Metal Parts via Jetting Nanoparticles," Solid Freeform Fabrication Proceedings.

[11] Draper, G. L., Dharmadasa, R., Staats, M. E., Lavery, B. W., and Druffel, T., 2015, "Fabrication of Elemental Copper by Intense Pulsed Light Processing of a Copper Nitrate Hydroxide Ink.," ACS Appl. Mater. Interfaces, 7(30), pp. 16478–85.

[12] Petukhov, D. I., Kirikova, M. N., Bessonov, A. a., and Bailey, M. J. a., 2014, "Nickel and copper conductive patterns fabricated by reactive inkjet printing combined with electroless plating," Mater. Lett., 132, pp. 302–306.

[13] Liu, J., 2009, "In Situ Created Metal Nanoparticle Strengthening of Metal Powder Articles", United States patent US 2009/0007724 A1

[14] Lin, Z., Han, D., and Li, S., 2012, "Study on thermal decomposition of copper(II) acetate monohydrate in air," J. Therm. Anal. Calorim., 107(2), pp. 471–475.

[15] Perelaer, J., Smith, P. J., Mager, D., Soltman, D., Volkman, S. K., Subramanian, V., Korvink, J. G., and Schubert, U. S., 2010, "Printed electronics: the challenges involved in printing devices, interconnects, and contacts based on inorganic materials," J. Mater. Chem., 20(39), p. 8446.

[16] Kamyshny, A., 2011, “Metal-based Inkjet Inks for Printed Electronics,” Open Appl. Phys. J., 4(1), pp. 19–36.

[17] Farraj, Y., Grouchko, M., and Magdassi, S., 2015, “Self-reduction of a copper complex MOD ink for inkjet printing conductive patterns on plastics,” Chem. Commun., 51(9), pp. 1587–1590.

[18] Shin, D. H., Woo, S., Yem, H., Cha, M., Cho, S., Kang, M., Jeong, S., Kim, Y., Kang, K., and Piao, Y., 2014, “A self-reducible and alcohol-soluble copper-based metal-organic decomposition ink for printed electronics,” ACS Appl. Mater. Interfaces, 6(5), pp. 3312–3319.

[19] Yang, W., Liu, C., Zhang, Z., Liu, Y., and Nie, S., 2014, “Copper inks formed using short carbon chain organic Cu-precursors,” RSC Adv., 4(104), pp. 60144–60147.

[20] Bai, Y., and Williams, C. B., 2015, “An exploration of binder jetting of copper,” Rapid Prototyp. J., 21(2), pp. 177–185.

[21] Bai, Y., Wagner, G., and Williams, C. B., 2017, “Effect of Particle Size Distribution on Powder Packing and Sintering in Binder Jetting Additive Manufacturing of Metals,” J. Manuf. Sci. Eng., 139.

[22] Salavati-Niasari, M., Davar, F., and Mir, N., 2008, “Synthesis and characterization of metallic copper nanoparticles via thermal decomposition,” Polyhedron, 27(17), pp. 3514–3518.

[23] Deng, D., Qi, T., Cheng, Y., Jin, Y., and Xiao, F., 2014, “Copper carboxylate with different carbon chain lengths as metal-organic decomposition ink,” J. Mater. Sci. Mater. Electron., 25(1), pp. 390–397.

[24] Li, Y., Qi, T., Cheng, Y., and Xiao, F., 2015, “A new copper ink with low sintering temperature for flexible substrates,” 2015 16th International Conference on Electronic Packaging Technology.

[25] Yang, W. dong, Wang, C. hai, Arrighi, V., Liu, C. yan, and Watson, D., 2015, “Microstructure and electrical property of copper films on a flexible substrate formed by an organic ink with 9.6% of Cu content,” J. Mater. Sci. Mater. Electron., 26(11), pp. 8973–8982.

[26] Yabuki, A., Tachibana, Y., and Fathona, I. W., 2014, “Synthesis of copper conductive film by low-temperature thermal decomposition of copper-aminediol complexes under an air atmosphere,” Mater. Chem. Phys., 148(1–2), pp. 299–304.

[27] ASTM Standard B962-08, Standard Test Methods for Density of Compacted or Sintered Powder Metallurgy (PM) Products Using Archimedes’ Principle.

[28] Derby, B., 2010, “Inkjet Printing of Functional and Structural Materials: Fluid Property Requirements, Feature Stability, and Resolution,” Annu. Rev. Mater. Res., 40(1), pp. 395–414.

[29] Bai, Y., Wagner, G., and Williams, C. B., 2017, “Effect of particle size distribution on powder packing and sintering in binder jetting additive manufacturing of metals,” J. Manuf. Sci. Eng. Trans. ASME, 139(8).

[30] Kumar, A., Bai, Y., Eklund, A., and Williams, C. B., 2017, “Effects of Hot Isostatic Pressing on Copper Parts Fabricated via Binder Jetting,” Procedia Manuf., 10, pp. 935–944

7. Conclusions and broader impacts

7.1. Summary of research

In this work, binder jetting was identified as a suitable AM platform to process thermally conductive and optically reflective materials. Specifically, a manufacturing process chain was created to fabricate complex structures made of high purity copper. Through the establishment of the manufacturing process and the exploration of the printed copper properties (Chapter 2), challenges have been identified that provided the motivation for the rest of the work.

Overall Motivation
Establish a manufacturing process and material system for fabricating high purity copper parts with reduced porosity, less shrinkage, and improved structural integrity.

Driven by this overall motivation, a multimodal particle size system was investigated in an effort to address the process limitations in binder jetting through filling powder bed voids with smaller particulate materials, embodied in the forms of (i) a powder bed of bimodal powder mixture, and (ii) a nanoparticle binder that can deposit metal contents to the powder bed. While the new material systems aimed to improve the printed copper material properties, the focus of this work and the primary research goal was to develop a fundamental understanding on how the bimodal particle size systems affect the printed material properties and binder-powder interactions for binder jetting of metals or ceramics.

Primary Research Goal
To gain an understanding of how the fine particulates added to powder bed affect printed part properties and binder-powder interactions in binder jetting of metal.

Driven by this primary research goal, the printed part properties were investigated in the use of a powder bed of bimodal particle mixtures (Chapter 3) and three different types of nanoparticle binder (Chapter 4 and 6). Recognizing the influence a particle suspension can have on the binder jet printing process, a tool for characterizing the binder-powder interactions was developed in Chapter 5 and used for understanding the effects of nanoparticle suspensions on the binder permeation and powder granulation process.

A summary of the key results formed from answering each research question is provided in the following sub-sections.

7.1.1. Research Question 1

The effect of a bimodal powder mixture powder bed on the printed part properties was studied by answering Research Question 1. Powder bed particle size distribution was varied through the mixing of differently sized powders, which was hypothesized to be capable of increasing powder bed packing efficiency and improving sintered density.

Research Question 1:
How does the powder bed of bimodal powder mixture affect the green/sintered part density and sintering shrinkage of binder jetting printed parts?
Hypothesis 1:
Unlike traditional powder metallurgy processes where high sintered density is typically achieved through sintering monosized fine powders, the use of bimodal powder mixture over ultra-fine powder constituent in binder jetting can increase sintered density with reduced shrinkage.

The use of bimodal powder mixtures has shown several benefits in the experiments with binder jetting of copper. The tested powder mixtures have successfully improved powder packing density and powder flowability compared to the monosized ultra-fine powder (5 μm). As a result, the printed green part density was able to increase by up to 9.4% as compared to the monosized powder counterparts (Figure 3.1).

The use of bimodal powder mixtures has also improved the sintered density. For example, through a wider particle size distribution created by replacing 15 μm powder with the 30+5 μm powder mixture, the sintered density improved by 12.3% (Figure 3.3). However, when ultra-large particles (e.g., 75 μm) were mixed into 15 μm powder, the sintered density was not improved due to the rigid skeleton formed by the large particles where the sintering contribution of the fine powder was constrained (Figure 3.3).

The feasibility of improving sintered density by bimodal mixtures compared to the constituent powders has also been demonstrated (Figure 3.2). The obtained result was different than the understanding in traditional powder metallurgy processes where high sintered density is typically achieved through sintering the monosized fine powder constituent. The unique result in binder jetting was mostly attributed to the significantly inhibited sintering shrinkage of the ultra-fine constituent powder (5 μm), as it was revealed in an existing sintered density prediction model (Section 3.3.5).

In addition to the increased sintered density, the use of bimodal powder mixtures has shown additional benefits: (i) the sintering shrinkage was reduced due to an increased green density (Figure 3.2 & 3.3); (ii) the bimodal powder mixture was less sensitive to sintering conditions, and potentially can be sintered with less energy input compared to monosized powders (Figure 3.4).

7.1.2. Research Question 2

The effect of nanoparticle binder on printed part properties was studied by answering Research Question 2. Because of the reduced sintering temperature of nanoparticles, it was hypothesized that the nanoparticles jetted into the powder bed interstices can sinter and fuse powder particles together after heating the powder bed, which enabled the creation of green parts and its separation from the unsintered powder particles (Hypothesis 2.2). It was also hypothesized that the use of nanoparticle binders can improve green and sintered part properties (Hypothesis 2.1).

Research Question 2:
How does the jetted nanoparticles affect the printed green and sintered part properties?
Hypothesis 2.1:
Jetted nanoparticles can densify the printed green part and reduce sintering shrinkage. Improved sintered density with less sintering shrinkage can be produced by increasing the binder saturation ratio of printing the nanoparticle binder.
Hypothesis 2.2:
Nanoparticles can be used in the binder with or without polymer adhesives. Metal powders can be printed by jetting nanoparticles as a binder to replace the role of organic binders. A metallic binding mechanism is enabled through sintering the jetted nanoparticles at a temperature lower than the micron-size powder particles to selectively provide bonding strength to the powder bed, which enables satisfactory green part strength and printed part retrieval from the unsintered powder particles.

Three different types of nanoparticle binders have been created for answering Research Question 2: colloidal organic binder (copper nanoparticles suspended in organic binder), copper nanosuspension (copper nanoparticles suspended in adhesive-free dispersing medium), and copper MOD ink (a particle-free organometallic precursor to nanoparticles) (Table 7.1). The three nanoparticle binders are different in their binding mechanisms: the binding function of the colloidal organic binder still relies on the

polymerization of organic adhesives, and the latter two are considered as inorganic metal binders as they eliminate the need for polymer adhesives.

Table 7.1 Summary of the nanoparticle binders used in this work

	Metal content (wt%)	*Fluid type*	*Presence of organic adhesives*
Colloidal organic binder	17.4%	Particle suspension	Yes
Nanosuspension	23.3%	Particle suspension	No
MOD ink	7.4%	Organometallic dispersion	No

Hypothesis 2.1 was tested using the colloidal organic binder and nanosuspension. Compared to the use of the ExOne's organic binder, the green density in both binders was improved (Figure 4.3 and Figure 4.12), which led to a reduced sintering shrinkage (Figure 4.4, 4.5, 4.14 and 4.15). While the colloidal organic binder was capable of producing denser green parts, the sintered density was not significantly improved over the regular polymer binder printed parts, as the sintering densification was reduced by the extra amount of the jetted nanoparticles and organic adhesives (Figure 4.4 and Figure 4.5). However, the inkjetted nanoparticles improved the tensile strength of the sintered parts (Figure 4.8) through a reduced grain size (Figure 4.6). The sintered density was able to be further improved when the nanosuspension was used as the binder with ultra-high binder saturation ratios; however, a powder recoating defect was caused by the nanoparticle accumulation on top of printed layers (Figure 4.13). Unlike the use of organic binders, the sintered density was increased when a higher binder saturation ratio was used, as the jetted metal contents constitute towards the final sintered parts.

When the MOD ink was used, the sintered density was lower than the organic binder printed parts (Figure 6.16) due to a lower solid loading of nanoparticles and the insufficient green strength (Table 6.2). However, the sintered parts have generated a dense core section with less porosity than the organic binder printed parts (Figure 6.12). A porous outer shell composed of large pores was formed around the dense core in the MOD ink printed parts, mainly caused by the powder loss in depowdering the green parts due to the insufficient powder bonding strength.

Hypothesis 2.2 was tested using the copper nanosuspension. Enabled through the sintering temperature reduction of nanoparticles, the jetted nanosuspension was sintered to provide bonding strength to the printed green parts when a heat was supplied to the powder bed during printing (Figure 4.10 and Figure 4.11). This work has shown that a metal nanosuspension in a non-adhesive dispersing medium can replace organic binders for printing metal parts, and was capable of producing satisfactory green part strength (Figure 4.11), with an improved structural integrity (Figure 4.18) and metal purity (Table 4.3) in the sintered parts.

Copper MOD ink was also tested as a binder for printing copper. The MOD ink was used as a precursor to the nanoparticle binder, by initiating binding between metal powders through sintering the precipitated nanoparticles from the jetted organometallic ink in a reducing atmosphere (Figure 6.10). The inkjetted MOD ink was dried between printed layers by an overhead heater to remove the solvent; the printed powder bed then went through a post-printing curing step in a reducing atmosphere to precipitate and sinter nanoparticles from the organometallic complex without particle growth and oxidation.

7.1.3. Research Question 3

The nanoparticle binder's impact on the binder jet printing process was studied by answering Research Question 3. It was hypothesized that the suspended particles in a binder changes the binder rheology, which ultimately affects the binder-powder interaction behaviors and the resultant printed primitive morphology. Before Research Question 3 can be answered, a tool to characterize the binder-powder interaction has to be first created.

Research Question 3:
How does the solid loading of nanoparticles in a binder and the powder bed pore size affect the binder-powder interaction and resultant printed primitive size?
Hypothesis 3:
As the nanoparticle content increases, the binder surface tension decreases and viscosity increases, thus reduces the powder permeability through inhibited binder penetration. Smaller printed primitives are created as a result of the reduced powder permeability. The powder permeability is further reduced in smaller pore size powder beds as the binder penetration time decreases.

Several colloidal organic binders were created by suspending copper nanoparticles into an organic binder at different solid loadings (7.5-22.5 wt%), and used to study the impact of nanoparticle suspension binder on the binder-powder interactions and printed primitive formation in binder jetting. A characterization methodology, powder bed sessile drop goniometry, was first developed by leveraging the gained understanding of the physics in liquid-powder interactions.

The binder wetting and penetrating powder bed behavior was described by the dynamic contact angle of a binder inside the powder capillary pores, which was derived from the measured penetration time in the contact angle goniometry experiment. The powder bed sessile drop goniometry also produced binder-powder granules that can be directly measured for dimensions, and used to estimate the dimensions of the primitives generated by inkjet and to guide printing parameter selections. The dynamic contact angle was more useful for binder jetting than other metrics (e.g., apparent contact angle) as it (i) provides information on a combined wetting and penetrating dynamic process, and (ii) is correlated with the binder penetration depth and primitive size.

The effect of solid loading of a nanoparticle suspension binder was studied with the powder bed sessile drop goniometry. The increased viscosity (Figure 5.9) and reduced surface tension (Table 5.2) in the nanoparticle suspensions with a higher solid loading prolonged the binder penetration time, especially in the less porous powders (Figure 5.13). As the solid loading in the nanoparticle suspensions increased (7.5-22.5 wt%), the powder permeability was reduced, which was reflected in the larger dynamic contact angle (Figure 5.14), reduced penetration depth (Figure 5.17), larger equilibrium saturation ratio (Figure 5.18), and reduced capillary pressure (Figure 5.19). When the nanoparticle suspension (7.5 wt%) was compared to the pure organic binder, the powder permeability was improved driven by a higher capillary pressure, as a result of a hypothesized enhanced local capillary flow caused by the surface tension gradient around the nanoparticles. This enhanced capillary action resulted in an increased primitive size, which lowered the required amount of binder for stitching primitives but reduced feature resolution in printed parts (Table 5.3).

7.2. Limitations and future work

Several limitations have been encountered throughout the execution of this research study. These limitations are discussed in the following subsections, along with the directions proposed for the future work.

7.2.1. Generalization of the results

All experimental work was conducted in the context of copper, as fabricating copper with improved material properties was the motivation and focus of this research. It is hypothesized that the understanding gained in the investigation of the multiscale particle systems in binder jetting of copper can be applied to a broader range of materials. As a part of the future work, experiments should be conducted in different materials to provide additional evidence to support the generalization of the conclusions made in this work.

7.2.2. Material systems used for experimentation

While the bimodal powder mixture created in Chapter 3 has successfully answered Research Question 1, it is worth noting that only two mixing ratios were used for mixing small and large particles due to the limited resources. There is an opportunity to modify the existing sintered density predicting model to be more accurate in predicting the binder jetting printed part densities using an empirical approach. However, the development and validation of the modified model will require more powder mixing ratios created for the experimentation.

The nanoparticle binder systems created in Chapter 4 and 6 are limited in the highest achievable particle solid loading while maintaining the ink jettability and stability. For example, the effectiveness of using the MOD ink to improve sintered density was strongly limited by the relatively low metal content (7.4 wt%). Similarly, the colloidal organic binder was limited in the solid loading in order to maintain the jettability, and was found to be difficult to maintain good stability at higher solid loadings (e.g., 22.5 wt%) even with the use of different dispersants. As a result, there exists an opportunity to optimize the synthesis routes and dispersing strategies to produce higher solid loading and metal content nanoparticle binders, which are hypothesized to be more effective in improving the sintered part density.

7.2.3. Characterizing the binder-powder interaction in binder jetting

The powder bed sessile drop goniometry developed in this work has provided a viable platform to characterize the binder-powder interaction process and printed primitive formation. However, it is worth noting that the sessile drop method does not exactly reflect the binder jetting process. For example, the powder bed sessile drop experiment is limited in that no drop velocity is considered, which is believed to be a significant factor in influencing the binder penetration process. Future work can focus on (i) modifying the existing binder-powder interaction models to include drop velocity and volume factors, and/or (ii) developing a new experimental platform integrating inkjet printing with powder bed contact angle goniometry, with the help of high-speed image capturing and printed primitives microscopic observation capabilities.

Finally, there also exists an opportunity to develop the next generation tools and methodologies for the metrology in Additive Manufacturing. In the conducting of this work, several challenges have been encountered in the measurements of green part density, powder bed packing density, and porosity distribution in the printed parts, which have limited the overall effectiveness in producing statistically significant results. Future work may focus on characterizing the powder bed and printed parts using non-destructive methods (e.g., micro-CT) and in-situ monitoring techniques (e.g., thermal cameras, hot stage microscopes).

7.3. Publications

Five core publications are generated in accomplishing this work. A list of journal publications conference proceedings, and patent disclosures related to this dissertation is also provided.

Related research question	*Journal*	*Title*
N/A	Rapid Prototyping Journal (Volume 21, Issue 2)	An Exploration of Binder Jetting of Copper
RQ1	Journal of Manufacturing Science and Engineering (Volume 139)	Effect of Particle Size Distribution on Powder Packing and Sintering in Binder Jetting Additive Manufacturing of metals
RQ2	Materials and Design (Volume 147)	Additive Manufacturing of Metal Parts from Jetting a Particle-free Metal Ink as Binder Precursor for Binder Jetting
RQ2	Nanotechnology (submitted)	Effect of Inkjetted Nanoparticles on Metal Part Properties in Binder Jetting Additive Manufacturing
RQ3	Journal of Manufacturing Science and Engineering (submitted)	Characterizing the Interaction between Nanoparticle Suspension Binder and Metal Powder in Binder Jetting Additive Manufacturing

Other publications related to this work are:

- Bai, Y. and Williams, C.B. (2017), "Binderless Jetting: Additive Manufacturing of Metal Parts via Jetting Nanoparticles", *International Solid Freeform Fabrication Symposium*, Austin TX
- Bai, Y. and Williams, C. B., "Additive Manufacturing of Metal Parts from Jetting a Particle-free Metal Ink as Binder", U.S. Provisional Patent, Application No: 62/596,555 Assignee: Virginia Tech, 2017
- Liu, J. (Peter), Liu, C., Bai, Y., Kong, Z. (James), Rao, P. and Williams, C.B. (2017), "Spatiotemporal Modeling and Layer-wise Prediction of Porosity in Additive Manufacturing", *IISE Transactions*
- Kumar, A., Bai, Y., Eklund, A. and Williams, C.B. (2017), "Effects of Hot Isostatic Pressing on Copper Parts Fabricated via Binder Jetting", *Procedia Manufacturing*, Elsevier B.V., Vol. 10, pp. 935–944.
- Wagner, G., Bass, L., Rau, D., Scott, Z., Wolf, M., Wolf D., Meenakshisundaram, V., Bai, Y., et al. (2017), "Design and Development of a Multi-Tool Additive Manufacturing System", *International Solid Freeform Fabrication Symposium*, Austin TX
- Bai, Y. and Williams, C. B., "Binderless Jetting - Using Nanoparticles to Replace Polymer Binders in Binder Jetting of Metal," U.S. Provisional Patent, Application No: 62/402,000, Assignee: Virginia Tech, 2016
- Bai, Y., Wagner, G. and Williams, C.B. (2015), "Effect of Bimodal Powder Mixture on Powder Packing Density and Sintered Density in Binder Jetting of Metals", *International Solid Freeform Fabrication Symposium*, Austin TX, pp. 758–771.
- Bai, Y. and Williams, C.B. (2014), "An exploration of binder jetting of copper", *International Solid Freeform Fabrication Symposium*, Austin TX, pp. 793–814.

7.4. Research contributions

In accomplishing this work, a manufacturing process for fabricating high purity copper by binder jetting AM was established. New material systems created for filling the powder bed voids were investigated for their relationships with the printed part properties. A fundamental understanding of the binder jetting process was developed through the study of the binder-powder interactions and printed primitive formation.

This work has brought major contributions to binder jetting by (i) filling the gaps in understanding the relationship between the powder bed particle size distribution to the printed part properties, and (ii) providing a fundamental understanding on the mechanisms of binder-powder interaction and printed primitive formation, and their correlations with the binder rheology and powder sizes.

In addition to creating a process chain for printing high purity copper via binder jetting, the following contributions have been made, which can be generalized to the binder jetting process as a whole:

- A validation of the use of bimodal particle size systems in binder jetting to improve sintered density and reduce sintering shrinkage
- A demonstration of the nanoparticle sintering as a new binding mechanism for binder jetting of metals that can improve the printed part purity and structural integrity
- An understanding of how the bimodal particle size distributions in a powder bed affect printed green and sintered part properties in binder jetting
- An understanding of the fundamental mechanisms of the binder-powder interactions and printed primitive formation in binder jetting, with an established correlation with the binder rheology and powder pore size
- An established methodology and experimental approach on characterizing the binder-powder interactions, which provides a fundamental approach to determine the material compatibility and predict printing parameters in binder jetting

7.5. Broader impacts

- This work has created a manufacturing process for highly conductive materials in the embodiment of high purity copper. A near full sintered density has been achieved through Hot-Isostatic-Pressing, which is made possible through the advancements made in this work. This demonstrated manufacturing capability can enable the advanced design and manufacturing of highly efficient thermal management systems.
- The nanoparticle binder systems created in this work can enable the printing of refractory materials in binder jetting. Refectory materials are considered as challenging to process in binder jetting, as the structural integrity of the printed geometry can be compromised by the debinding of organic binders at temperatures lower than the initial sintering point of the powder. The nanoparticle binder system can provide a permanent bonding to the printed powder skeleton through the sintering cycle, which may eliminate the requirements of support structures.
- The nanoparticle binder systems investigated in this work has created an understanding of the process-structure-property relationships for the use of a functional metal ink in binder jetting. This gained knowledge can be leveraged to expand the current manufacturing capability to the realization of multi-functional, multi-material and voxel-printing on inkjet-based AM systems. In an inkjet-based AM system, the multi-material printing capability is made possible through the inkjet deposition of different materials to a powder bed or solid substrate. Furthermore, the deposition of materials is defined voxel-by-voxel with a spatial control of composition, property, and functionality to enable functional gradient materials. Embodiments of this manufacturing capability include (i) printing metal alloys with compositional gradients by depositing inks that contain alloying elements (e.g., carbon) at different concentrations to a base metal powder, (ii) printing Ceramic-Matrix-Composite (CMC) or Metal-Matrix-Composite (MMC) through depositing inks that are loaded with particles to a powder bed of metals or ceramics, and (iii) printing pharmaceuticals with drug release control and dosage design by jetting multiple inks loaded with different Active Pharmaceutical Ingredient (API) to excipient powders.